UNIVERSITY OF LEEDS

Lithium Niobate Waveguides for Continuous Wave Terahertz Generation

John Alexander Campling Richards, MEng

Submitted in accordance with the requirements for the degree of Doctor of Philosophy

University of Leeds

School of Electronic and Electrical Engineering
Pollard Institute

March 2024

The candidate confirms that the work submitted is his own, except where work which has formed part of jointly-authored publications has been included. The contribution of the candidate and the other authors to this work has been explicitly indicated below. The candidate confirms that appropriate credit has been given within the thesis where reference has been made to the work of others.

J. A. C. Richards, M. C. Rosamond, A. G. Davies, E. H. Linfield, and J. R. Freeman, "LiNbO3 Waveguide for Efficient CW THz Generation," International Conference on Infrared, Millimeter, and Terahertz Waves, IRMMW-THz, vol. 2022-August, 2022

Test ribs in chapter 4 fabricated with assistance from Dr. Mark Rosamond.

Scanning electron microscope images (excluding focused ion beam images) in chapter 4 taken with assistance from Dr. Mark Rosamond.

Focused ion beam work in chapter 4 performed by John Harrington.

BCB spin curve data when mixed with mesitylene in chapter 4 provided by Connor Kidd.

Code for time domain spectroscopy analysis for refractive index evaluation in chapter 4 provided by Dr. Joshua Freeman.

Rib break photos in chapter 6 taken by Yifan Weng.

The thesis was proof-read before submission by a third-party proof-reader. The PGR confirms that the third-party proof-reading undertaken was in accordance with the Postgraduate Researcher Proof-reading Policy.

Dedicated to my parents, who bought me my Game Boy. I used to stare at the electronics through the transparent Pokémon cartridge, and the way the story appears on a screen is still like magic.

Acknowledgements

First and foremost I would like to thank my supervisors Dr. Joshua Freeman and Prof. Edmund Linfield, who were always patient and understanding with me and provided excellent advice when I needed it. Thank you for giving me with the opportunity to do this PhD, and to develop and grow from it. Furthermore, I would like to thank Prof. Giles Davies, Prof. John Cunningham, and Dr. Paul Dean for their contributions at project meetings, as well as Dr. Alexander Valavanis for keeping me organised with the lab meetings, and for the advice provided after my presentations and progress reviews. Give me that mug back! I would also like to express gratitude to those named above who taught me at undergraduate level, for lecturing the most interesting topics, so I could reach this point.

A very special thanks must be given to Dr. Mark Rosamond, who dedicated far more time than he would have liked to instructing me inside the cleanroom, and helping to make quick progress on device fabrication, despite the large time constraints from the covid-19 pandemic and the cleanroom moving buildings.

Special thanks to Dr. Reshma Mohandas, for showing me some of the ropes (or rather fibres) when I started the PhD. And to Yifan Weng, whose questions about the project kept me on my toes. I hope you manage to make advances on the project and don't have as many delays as I did!

Thank you to Dr. Thomas Gill, Connor Kidd, and Eleanor Nuttall. Both in and out of the university, the 'Turnover' group was always great company. Especially thanks to Connor, who I started both my masters project and PhD with, and who kindly shared his home as a bubble with me during the pandemic. I would also like to thank my other coworkers and lab-mates, Dr. Aniela Dunn, Dr. James Keeley, Dr. Craig Knox, Nicolas North, Nathan Fox, and Dr. Emily Darwin, among others, for creating a fun and social atmosphere to work in and providing advice from their own experiences.

Thanks to other group members; Dr. Christopher Wood, for his advice regarding aspects of the cleanroom fabrication and comments from the transfer viva. Dr. Li Chen, Dr. Rob Farr, and Chris Day for the cleanroom help. Also Dr. Andrew Burnett, always ready with a helpful comment or suggestion. Thanks to everyone else in the Pollard institute, your contributions, no matter how small, are appreciated.

I would like to thank my family; my father, mother, sister, and grandmothers. Dad, your DPhil has always been a lofty inspiration to reach for. Mum, you have always given me the push I need to get something done. Kate, you provide a dose of reality when they have their heads in the clouds. Granny and Grandma, thank you for the belief and the financial support throughout university. All the encouragement from you means everything.

I would also like to thank anyone else who directly or indirectly helped or inspired me to reach this point, whether an old school teacher or friend, or someone I've never met who influenced me through some form of media. A

special mention to Mr. Wooldridge in particular, who curated my electronics learning at GCSE level.

Abstract

In this work, a device is proposed which is capable of operating as an Electromagnetic (EM) wave emitter between 2 and 5 Terahertz (THz) in Continuous Wave (CW) operation. Very few widely tunable EM sources currently exist in this frequency range. The proposed THz source would be tunable and able to produce monochromatic emission over a broad spectral range at room temperature.

The proposed device employs a rib waveguide, fabricated from a thin film Lithium Niobate (LN) substrate. By phase matching the Near Infra-Red (NIR) and THz waves using cladding materials, Difference Frequency Generation (DFG) of two NIR pump beams is attempted in order to generate THz radiation.

Modelling of the device is presented, detailing the influence of geometry on phase matching and mode confinement. Calculations are then presented to estimate the expected power. The upper bound on emission power is given by the quality of the phase matching, which determines the length of the waveguide in which frequency conversion occurs. The results suggest that a realistic device operating at 2 THz could generate 2 µW of THz power.

Techniques to fabricate the proposed device are investigated and fabrication of LN rib waveguides is described. These test ribs are then characterised in an experimental setup.

An alternative approach to phase matching, using a Cherenkov angle, is presented near the end of the thesis as a route towards efficient THz generation with less stringent phase matching and simplified fabrication. The fabrication and experimental testing of this emitter is discussed.

List of Publications

The following journal and conference papers were published by the author during the course of the presented work.

Conference Publications

- **J. A. C. Richards**, M. C. Rosamond, A. G. Davies, E. H. Linfield and J. R. Freeman.
  "$LiNbO_3$ Waveguide for Efficient CW THz Generation".
  47th International Conference on Infrared, Millimeter, and Terahertz Waves (IRMMW-THz) 2022.

Contents

List of Abbreviations

AFM Atomic Force Microscopy

ALD Atomic Layer Deposition

Ar^+ Argon Ion

$BaTiO_3$ Barium Titanate

BCB Benzocyclobutene

CAD Computer Assisted Design

CW Continuous Wave

DFG Difference Frequency Generation

E-Beam Electron Beam

EDFA Erbium Doped Fibre Amplifier

EM Electromagnetic

EO Electro-Optical

ESD Electrostatic Damage

FEG Field Emission Gun

FEI Field Electron and Ion Company

FFT Fast Fourier Transform

FIB Focused Ion Beam

FOM Figure of Merit

FOx Flowable Oxide

FSR Free Spectral Range

FWHM Full Width at Half Maximum

GaAs Gallium Arsenide

GaP Gallium Phosphide

GE General Electric

HF Hydrofluoric acid

HNO_3 Nitric acid

ICP-RIE Inductively Coupled Plasma Reactive Ion Etching

InP Indium Phosphide

IR Infra-Red

LEMAS Leeds Electron Microscopy and Spectroscopy

$LiTaO_3$ Lithium Tantalate

LN Lithium Niobate

LNOI Lithium Niobate On Insulator

MBE Molecular Beam Epitaxy

MgO Magnesium Oxide

NIR Near Infra-Red

OPA Optical Parametric Amplification

OPO Optical Parametric Oscillation

OR Optical Rectification

PC Photoconductive

PD Photodiode

PE Proton Exchange

PECVD Plasma Enhanced Chemical Vapour Deposition

PM Polarisation Maintaining

PPLN Periodically Poled Lithium Niobate

QCL Quantum Cascade Laser

QPM Quasi Phase Matching

QW Quantum Well

RIE Reactive Ion Etch

SEM Scanning Electron Microscope

SH Second Harmonic

SHG Second Harmonic Generation

Si Silicon

SiO_2 Silicon Dioxide

SNR Signal to Noise Ratio

SPP Surface Plasmon Polariton

TDS Time Domain Spectroscopy

TE Transverse Electric

THz Terahertz

TM Transverse Magnetic

TO Transverse Optical

UoL University of Leeds

UTC-PD Uni-Travelling Carrier Photodiode

UV Ultra Violet

ZnTe Zinc Telluride

List of Figures

List of Tables

Chapter 1

Introduction

This thesis covers the research into a Lithium Niobate (LN) waveguide to generate Terahertz (THz) radiation. In this introduction, a broad overview of THz radiation and its applications is provided, before concluding with an outlook for the subsequent chapters.

1.1 Terahertz Radiation

THz radiation is part of the Electromagnetic (EM) spectrum, lying between the Infra-Red (IR) and microwave frequencies. Consequently, it is sometimes referred to as far IR radiation. The frequency range is without a standard definition, and has been quoted as anywhere within the range of 0.1 to 30 THz. This is, however, a broad region which overlaps with many existing spectral bands such as the sub-millimeter wave and mid-IR radiation bands [1, 2]. A perhaps more appropriate frequency range, which encompasses the area of interest to this project, is from 0.3 to 10 THz (0.03 - 1 mm).

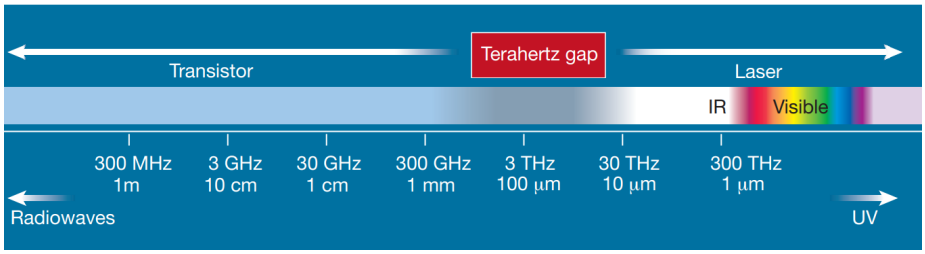

Figure 1.1: The THz gap, which is roughly between 0.3 and 10 THz. Figure taken from [2].

THz is an unexploited area of the EM spectrum, due to the challenge of generating a high power in this frequency range [3]. This has created what is commonly referred to as the 'THz gap'. On the lower frequency side of

the gap, transistor technologies reach the limits of their switching speeds when approaching the THz range. On the higher frequency side, methods of photon generation rely on transitional states. However, the bandgap size that relates to THz wavelengths is so small that ambient room temperature can provide enough energy to electrons to disrupt the system. A diagram of the EM spectrum, with the THz region highlighted, is displayed in Figure 1.1 [2].

1.1.1 Terahertz Applications

The potential applications of THz are wide ranging owing to their useful properties. These properties include being non-ionising, meaning they are safe for humans, and are described as non-destructive and non-invasive. They are strongly absorbed by water, and have unique absorption peaks for many materials, while non-polar materials such as plastics and clothing are transparent to the radiation. This consequently opens up opportunities in many fields, such as security with drugs and explosives screenings [4], healthcare with certain high contrast medical scans [5], and meteorology with observations about the atmosphere and weather [6]. THz spectroscopic analysis of ultra cold molecules could even help with molecular understanding [7]. On the other hand, due to having such a short wavelength, some of the frequencies in this band are strongly attenuated by the atmosphere. This means they can suffer from wave path changes through the atmosphere's variable refractive index, and have a short penetration depth [8]. Due to an abundance of natural THz radiation along with the lack of atmosphere in space, THz technologies are sought after for many astronomical applications; heterodyne detection of THz from far away objects being one example.

However, to reach prominent commercial interest, THz technologies need to improve. Solid state and compact devices must be engineered [9]. These technologies must start to achieve reasonable efficiencies without drawbacks such as needing cryogenic cooling [10] or having a poor linewidth [7].

1.1.2 High Resolution Terahertz Spectroscopy

A key application of THz wavelengths is in the use of spectroscopy. THz spectroscopy is "a powerful analytical tool" [11], and is performed best when using Continuous Wave (CW) systems, which "define the state-of-the-art in terms of spectral resolution", which lies in the megahertz range [12]. Several absorption and vibration lines appear in this region [13], whilst heat, pressure, dynamics, and molecular concentration can all also be detected [6]. There are currently several effective methods for creating high resolution THz spectroscopy. One method is to use a Quantum Cascade Laser (QCL), a device discussed further in Section 2.1.2.1, as they are ideal for use as either an absorption or heterodyne spectrometer. Another is a femtosecond laser based frequency comb [14]. Remote sensing, and investigation of atom structures and states, are open for investigation with such techniques [11]. Other areas explored with THz spectroscopy include the Earth's atmosphere, molecules in space [1], and biological

molecules, which have been investigated using waveguided Time Domain Spectroscopy (TDS) [15].

1.1.3 Issues with Current Terahertz Generation

Technologies exist trying to bridge the THz gap. However, these devices have not reached commercial success due to a range of issues. Therefore, a device is proposed, described at the start of Chapter 3, to tackle some of the common problems.

The device aims to:

- Be tunable within a range of 1 to 5 THz
- Provide powers of at least a few microwatts within this frequency range
- Provide a low linewidth
- Operate at room temperature
- Provide a CW emission

These properties do not exist together within a single device at present. The most comparable device is perhaps a photomixer, discussed in Section 2.1.3.3. However, this suffers a steep power drop off at frequencies above approximately 1 THz [7]. Most devices able to generate powers in the specified frequency range rely on transitional energy states, such as QCLs (Section 2.1.2.1), are unable to run at room temperature due to the size of the bandgaps. Pulsed generation techniques typically generate higher powers than CW, yet this comes with larger linewidths. Pulsed and CW efforts are established in Section 2.1.

1.2 Thesis Structure

A background of the relevant theory to the project is presented in Chapter 2. Starting from some common THz generation sources, it builds into non-linear generation techniques, then waveguide theory, and culminates in an analysis of how LN has previously been used for generating THz. At the end of this review, the motivation for the project is addressed.

The background information leads into Chapter 3, which is where the proposed device is introduced. Here, diagrams are provided to display the waveguide structure, with an explanation on how it works, followed by simulations about optimal waveguide design and predicted performance.

In Chapter 4, the fabrication of the waveguide is described. It starts with an investigation into different fabrication techniques for creating a LN rib and deposition of the cladding layers, followed by the construction method for a batch of test ribs. A discussion on how to produce high quality optical ridge facets is included.

The results section starts in Chapter 5, where Near Infra-Red (NIR) testing on the batch of test ribs discussed in chapter four is reported on. This experimentation provides an insight into the ridge loss, coupling loss, and polarisation properties of the rib.

In Chapter 6, an alternative LN waveguide design is discussed, as a step along the way to the full phase matching of the initial proposal. The design of this waveguide is introduced, along with its fabrication, before THz generation tests are detailed.

An evaluation of this research is given in Chapter 7, before exploring the prospective future work which could be undertaken.

Chapter 2

Prevailing Terahertz Generation Techniques

Various methods for generating THz presently exist, the problem is how to make a significant quantity coherently, in order to be applied commercially. Different techniques of generating THz are detailed in this chapter, leading up to the research proposal in the ensuing chapter, and in which ways the proposed device will fill a gap in modern THz generation technologies.

The chapter sections are outlined below:

- Terahertz Generation Sources
- Second Order Non-linear Terahertz Generation
- Waveguiding
- Previous Terahertz Generation via Lithium Niobate Crystals
- Project Motivation

2.1 Terahertz Generation Sources

2.1.1 Pulsed and Continuous Wave Generation

There are two broad categories for producing THz radiation; pulsed, which typically produces a broadband spectrum, and CW, associated with a narrow spectrum.

CW THz emitters can have a very low linewidth, in the region of a few megahertz, if produced by a system involving CW pump beams, such as photomixing or Optical Rectification (OR). This is due to the emission linewidth being determined by the pump linewidths, which can be sourced from highly established devices from the telecommunications region of the EM spectrum.

For a comparable pulsed system, the THz bandwidth is dependant upon the incident pulse duration [16].

Pulsed emission is often used for THz time domain systems, such as spectroscopy, due to a high Signal to Noise Ratio (SNR). However, pulsed systems often have high costs and sizes. CW systems typically have lower SNRs in the time domain due to requiring lower pump powers in order to avoid component damage. For example, THz frequency QCLs have reached a peak emission power of around 2.4 W [17] for pulsed operation, but significantly less than that power in CW [18]. Pulsed systems are often used for non-linear techniques due to their high peak powers [19]. However, imaging using CW is faster [16].

Various methods exist for generating either pulsed or CW THz, and some generation methods can be run in either orientation, such as a QCL. Pulsed methods operate at different pulsing rates, for example, Photoconductive (PC) switches generate THz pulses of picosecond lengths [16], while non-linear crystals are in the nanosecond range [1], and time domain systems are in the femtosecond range [16]. This impacts the frequency resolution of pulsed methods, which is determined by the pulse width.

2.1.1.1 Pulsed Generation

Femtosecond lasers can produce high power and ultra short pulses, and consequently are used as the input for many generation techniques, including OR in crystals such as LN [20], PC emission, and air plasma based generation [21]. A laser oscillator is typically used for most THz systems, but amplified laser systems employ a chirping process to the femtosecond oscillator output in order to reach a high pulse power while remaining below the point of causing component damage. This is done by heightening the pulse energy while simultaneously reducing repetition rate.

A femtosecond laser can produce pulses with a bandwidth of around 100 THz in a lossless non-linear crystal via OR. However, no non-linear medium can provide a uniform emission over such a bandwidth, due to phonon resonances in this frequency region. In contrast, a PC emitter can have comparatively small bandwidths of around 15 THz. A PC emitter is a switch, where the turn on time is affected by the pulse duration.

Femtosecond pulses allow THz frequency TDS to be performed. This is where an input pulsed beam is split in two, to form a pump and a probe beam. The pump activates a THz emitter (either PC emission or OR), which then shines upon a detector after passing through a sample space, while the probe beam also reaches the detector, but via a delay stage. The probe beam can then measure the THz reading at the detector, and can evaluate both amplitude and phase [1].

2.1.1.2 Continuous Generation

Generation in CW tends to have less peak power than a pulsed signal, which allows a cooling period between the high power pulses to avoid component dam-

age. However, the trade off is that a CW signal is an uninterrupted source, resulting in a more comparable average power. Methods of CW generation vary. THz can be created CW by either a transition of electron states or a periodic acceleration of electrons. A QCL is an example of a transitional state approach, while free electron lasers, photomixers, and backwards wave oscillators all periodically accelerate electrons, although on greatly different scales. Several CW schemes utilise optical frequency mechanisms, examples being microwave frequency multiplication and Optical Parametric Amplification (OPA). The heavy use of optical technology is because it can be ultrafast. For instance, when photomixing, ultrafast lasers may be chosen in order to facilitate the fast transitional time of a PC switch. For CW characterisation, thermal detectors such as bolometers are normally used [1], although other detector types such as heterodyne detectors also exist [22].

In conclusion, both pulsed and CW operation have their merits. For example, when considering THz generation via non-linear crystals, pulsed operation leads to high peak pump powers, providing a higher conversion efficiency due to increased intensity. However, CW operation provides a better spectral resolution, which can be used for stabilisation of other systems which suffer from frequency jitter.

2.1.2 Electrically Driven Sources

Generating THz can be done either via providing an electrical input or an optical input. Some electrically driven THz generation schemes are described here, before moving on to laser driven sources in Section 2.1.3.

Electrically driven sources rely upon electron movement. By supplying an input bias, electrons can be pumped to higher energy states. The relaxation of the electrons to the lower energy states is what releases the THz frequency emissions. Other electrically driven methods rely on electron oscillation via alternating current.

2.1.2.1 Quantum Cascade Lasers

Lasers are photon generation devices which work by amplifying the number of photons via multiple electron transitions to create coherent radiation. The first laser was a ruby laser in 1960, by T. H. Maiman. It operated at a wavelength of 6943 Å [23]. Advances in laser technology and the development of Molecular Beam Epitaxy (MBE), a method of growing semiconductors at a level of atomic precision, have led to the QCL, first fabricated in 1994 by Faist et al. and operated at 4.2 µm [24].

A QCL is an intersubband semiconductor laser; a monochromatic radiation source which is defined by amplitude, frequency and phase. Since the first QCLs, refinements have been made which mean THz frequency QCLs now exist. The first THz QCL operated at 4.4 THz and at 2 mW at 50 K, created by Kohler et al. in 2002 [9]. Since then, THz QCLs have been demonstrated operating in a range of 1.9 - 5 THz [18], with output powers of 2.4 W [17].

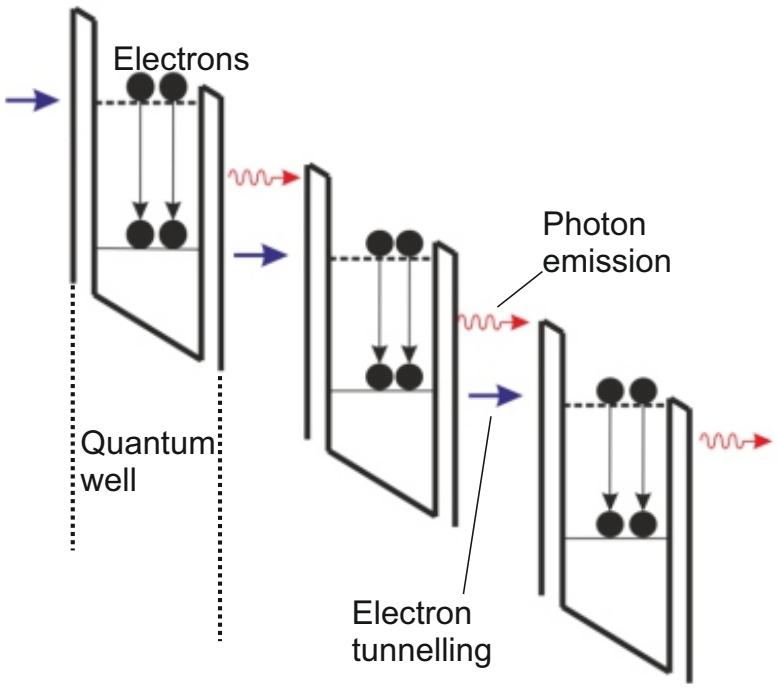

Figure 2.1: QCL periods showing Quantum Well (QW)s. Under an induced bias, the wells align and the electrons can tunnel from the lower state of one well into the higher energy state of the adjacent well. An electron can 'cascade' through many wells in this manner, meaning a single electron can create multiple photons. Figure taken and edited from [16].

Generating THz radiation via electronic transitions in a semiconductor requires bandgap engineering, as there is no naturally occurring material with a bandgap which corresponds to THz wavelengths. Bandgap engineering is performed by growing different crystal structures on top of each other. Using advanced material growth methods such as MBE or chemical vapour deposition, superlattice structures with multiple junctions and engineered material widths can be fabricated. This facilitates the creation of QWs, seen in Figure 2.1. The width of a QW determines the spacing between the energy states within it, and hence the characteristics of a photon released from it. By defining these QW widths it is possible to generate THz radiation.

When the electrons are pumped to a higher energy state using a bias, population inversion is reached. When one electron naturally decays into a lower energy state, emitting a photon, this causes the other electrons to decay also via stimulated emission. The electric field caused by the applied bias can also be used to align the QWs, by having the lower energy state of one well line up with the higher energy state of the next, allowing the electrons that have emitted to

tunnel through to the next QW, where they can emit by dropping an energy state again. Hence, a single electron can emit multiple photons, by cascading through the QWs [3].

A QCL typically consists of an active region within a ridge, top and bottom contacts for electrical connections, and a waveguide for mode confinement. The QCL cavity has a fully reflecting facet at one end and a partially reflecting facet at the other. This allows light to build up inside the cavity, which is then emitted when the mirror losses are larger than other device losses. Two different types of QCL waveguide have been created; single metal and double metal. Developments have also resulted in differing designs of QCL structure, which have different operating characteristics. These structures include chirped superlattice, bound to continuum, and resonant phonon. It is also possible to get a hybrid design; a bound to continuum device with aspects of the resonant phonon design [16, 25]. Another QCL design performs intra-cavity non-linear THz generation [10], described later in this chapter, in Section 2.2.4.

At THz frequencies QCLs suffer from the fact that to create this radiation the energy levels must have such small spacing that any thermal fluctuation may affect the energy level an electron is occupying, ruining the population inversion and consequently the stimulated emission of the device. An electron moving to a higher state due to excess heat energy is known as thermal backfilling. As a result, the QCL must be cryogenically cooled to prevent such disturbances. It is well documented that the higher the temperature a QCL is operated at, the larger the threshold current and worse the output power [26]. Raising the operating temperature of QCLs is a key research area. A recent record for the maximum operating temperature of a THz QCL is 260 K [27].

QCLs also suffer from frequency jitter and drift. The frequency of a laser can fluctuate by up to a few megahertz, creating a larger linewidth [28]. This jitter is caused by thermal, mechanical, and electric instabilities within the laser [16]. Injection locking is a method of countering this. Allowing QCLs to be used for high power THz spectroscopy. By injecting an EM wave into the QCL cavity, similar enough in frequency to the operating frequency of the QCL, the QCL 'locks' to the injected frequency and stabilises [7]. Several ways to lock a QCL have been demonstrated, included via an erbium doped fibre laser, photomixer, super-lattice mixers, schottky mixers, and a telecommunications frequency comb [29].

2.1.2.2 Other Electrically Operated Sources

Further electrically driven sources exist, such as backward wave oscillators, microwave frequency multiplication, and P-type germanium lasers. While these generation methods have their own advantages, such as all being tunable, they also have their drawbacks. P-type lasers suffer in much the same way as QCLs do in needing cryogenic cooling and a low duty cycle in order to counteract the electrical heating which disrupts the desired electron levels. Meanwhile, microwave frequency multiplication and backward wave oscillators both hit an upper frequency limit of around one THz, and their power drops off rapidly after

this. Another scheme is the free electron laser, which when pulsed can produce up to megawatts in the lower THz range. However, this is not a compact THz source, as it requires a vast amount of space with large arrays of magnets and an electron accelerator, taking up several cubic metres of room each [1].

2.1.3 Laser Driven Sources

Diode lasers are very useful for certain THz generation methods, photomixing and Difference Frequency Generation (DFG) for example, by providing coherent NIR waves. This is because optics in the telecommunications area are quite advanced, with minimal attenuation and dispersion generally seen, along with performance proven equipment such as the Erbium Doped Fibre Amplifier (EDFA). Two common types of diode laser are distributed Bragg reflector lasers and distributed feedback lasers [30].

THz sources driven by these lasers rely on photons rather than electrons. This means that when attempting to generate THz this way, navigating the difficulties of transitional states over a small bandgap can be avoided. Some laser driven THz sources are described in this section.

2.1.3.1 Photoconductive Emission

PC emission, first achieved in 1984 [31], has a high optical to electrical efficiency and the ability to function without any cryogenic cooling [16]. PC emission can be operated in either pulsed or CW, depending upon the method. A comparison of pulsed PC switching against CW photomixing is shown in Figure 2.2. An advantage of PC based generation methods is not requiring the long interaction lengths that non-linear techniques do.

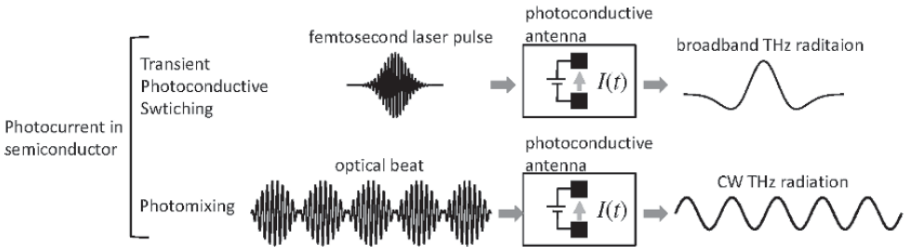

Figure 2.2: A comparison between pulsed and CW emission from photoconductives. Figure taken from [1].

PC emission is performed using a PC switch on a semiconductor surface. The PC switch can function as an electrical switch because of the increase in conductivity in the semiconductor due to an abundance of light, and the converse lack of conduction in an absence of light. Higher levels of light increase conduction due to creating more electron-hole pairs. The light must have a photon energy greater than that of the bandgap for the electron to reach the

conduction band. Electron-hole pairs created in this way are referred to as photocarriers [1].

A high carrier mobility and breakdown voltage are parameters of an ideal PC switch, as well as a short carrier lifetime. Low temperature grown Gallium Arsenide (GaAs) is a commonly used semiconductor for PC switches due to providing favourable properties [1].

The switches are incorporated into antenna structures [16]. These antennas have oppositely charged electrodes. When photocarriers are created and the antenna is biased, the holes are accelerated towards the negative electrode and the electrons towards the positive one. Different designs of PC antenna exist, including bow-tie, dipole and spirals. Methods of increasing the power of the antennas are to create resonant antennas for certain frequencies, or improve either the substrate or active region [1]. Research has also recently taken place investigating antennas with nanostructure aspects [32].

2.1.3.2 Pulsed Photoconductive Emission

In pulsed PC generation of THz, a single pulsed laser excites a PC switch leading to a generated photocurrent. The acceleration and recombination of these photocarriers can lead to THz transient pulses. Acceleration can be caused by applying a bias to a pair of electrodes on the semiconductor, which create an antenna structure. The bandwidth of the emission is determined by the switching time, controlled by the pump pulse and the switch material. The pulse width of the pump alters the switch rise time, and the carrier lifetime is dependant upon the semiconductor used. Subpicosecond switching is needed for THz, so pump pulse duration and photocurrent carrier lifetimes must reflect this. This means short pump pulses and fast recombination periods. Furthermore, the induced THz electric field is decided by the transient current density. Factors influencing the current density include carrier mobility, carrier concentration, and the amount of bias applied [1, 16].

2.1.3.3 Continuous Wave Photoconductive Emission

PC CW generation of THz is called photomixing. It is also known as optical heterodyne mixing, and has been defined as "the modulation in the conductance of a semiconductor due to the beating of two laser beams" [16]. Two CW lasers of similar frequencies create a beat frequency incident to the PC antenna which consequently creates a continuous THz wave. The THz wave has a frequency of the difference between the two incident lasers. Photomixing is an established PC method to create THz at room temperature. The response time of photomixing is very fast [33], and has a much higher efficiency than the non-linear technique OR (discussed in Section 2.2.2), although also has a more complicated setup and a smaller potential bandwidth [34]. A typical setup is displayed in Figure 2.3.

Photomixing can be used as a coherent detection method of THz radiation, as the induced photocurrent is dependant upon the phase difference between the THz wave and a beating optical probe signal [1].

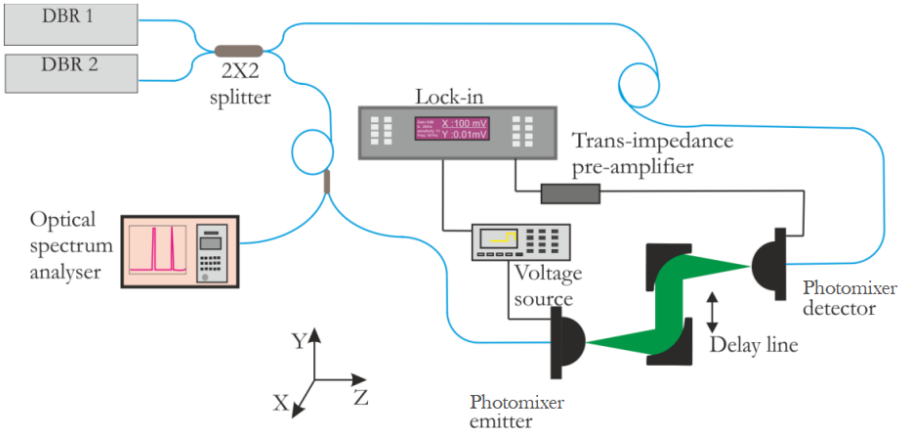

Figure 2.3: A system diagram of an example photomixing setup. *DBR* - Distributed Bragg Reflector diode laser. Figure edited from [16].

A photomixer is a compact and solid state device, capable of generating CW THz using a PC switch, and can have a very wide tuning range. They typically employ an antenna structure such as a logarithmic spiral design with interdigitated electrodes. Emission is suitable for use in applications such as injection locking QCLs [35]. However, the generated power is in the range of microwatts or less for THz frequencies, with a rather poor optical to THz conversion efficiency, along with a dependence upon the thermal conduction of the semiconductor material used. Low power issues are particularly true above 2 THz [32].

As photomixing has low SNR in comparison to pulsed PC switches due to lower peak powers, this can be considered as a lower dynamic range for TDS and therefore provide a lower quality scan. However, photomixing provides faster imaging [16].

A different CW approach is to replace the semiconductor layer with a photodiode, creating a Uni-Travelling Carrier Photodiode (UTC-PD). A conventional Photodiode (PD) operating at telecommunications frequencies allows low cost optical components to be utilised in generating THz. A UTC-PD is an improvement over a standard PD, with a reported three times as much bandwidth and 100 times as much power [33]. A UTC-PD is a solid state THz generator [36]. It contains an active layer and a carrier collection material, making use of a quick response time of holes and the high velocity of electrons. One study integrated tiny antennas into the UTC-PD design to minimise electrical loss. The advantages consist of having a minimal carrier transit time, low bias required, and a large saturation current. 10.9 µW of output power has been achieved at 1.04 THz [33]. Higher THz frequencies experience steady a drop in power levels however, due to the limitations of the carrier response times [1, 37].

2.1.3.4 Other Laser Driven Sources

Optical pumping using source lasers can be used in ways other than PC emission to generate THz. One example is the THz gas laser, which uses optical excitation in order to induce rotational transitions leading to THz radiation. Non-linear THz generation techniques are also dependant upon source beams, some of which are detailed in Section 2.2. One non-linear method of generating THz is through air plasma [1]. Air plasma generation of THz has been demonstrated using laser pulses by creating a density imbalance between electrons and ions using a high bias electric field [38]. The amount of THz generated is close to how much can be made by a semiconductor method, such as PC emission [1].

2.2 Second Order Non-linear Terahertz Generation

A laser driven form of THz generation; non-linear techniques rely on interactions within a non-linear crystal. The oscillating electric field from a source EM wave leads to a non-linear dipole movement within the crystal, which can be used to cause THz generation.

2.2.1 Non-Linear Crystals

Non-linear optics occurs in a non-linear medium, such as a periodic crystal lattice. Such crystals include LN, GaAs, and Indium Phosphide (InP). These crystal lattices have no inversion centre, and so are called non-centrosymmetric. Due to the crystal shape, the induced dipole from an EM wave is non-linear rather than linear, which is what allows the use of these crystals for non-linear techniques. Perhaps the most widely used Electro-Optical (EO) crystal for non-linear applications is Zinc Telluride (ZnTe), due to having a low refractive index mismatch at optical and THz frequencies. This means that little phase matching needs to occur to equate the velocities of concurrent different frequency waves through this crystal to minimise destructive interference. Other crystals may be desired due to having different crystal structures, or having different Transverse Optical (TO) phonon absorptions; non-radiative lattice vibrations which disrupt the THz generated at that frequency. Indeed, while Lithium Tantalate ($LiTaO_3$) has a minimum TO phonon frequency of 4.2 THz [39], Gallium Phosphide (GaP) has a much higher minimum TO phonon frequency of 11 THz [40]. TO phonons typically affect the region of five to ten THz [1].

These EO crystals can be used to generate THz using techniques such as DFG, exemplified by the device discussed in this thesis, described in Chapter 3. DFG is introduced in Section 2.2.4. Another use of EO crystals is to detect THz radiation via the application of an electric field [22, 41].

In linear optics, the polarisation can be defined by

$$P = \epsilon_0 \chi E \tag{2.1}$$

where P is polarisation, ε_0 is the permittivity of free space, χ is susceptibility, and E is electric field. However, polarisation becomes a series of increasing order terms when applied to a non-linear medium, due to being periodic non-uniform structures. This creates an equation with as many terms as there are non-linear elements.

$$P = \epsilon_0(\chi^{(1)}E + \chi^{(2)}E^2 + \chi^{(3)}E^3 + ...) \tag{2.2}$$

When looking at second order effects induced by OR, polarisation can be expressed by the following equation.

$$P_{\mathrm{i}}^{(2)}(0) = \sum_{j,k} \epsilon_0 \chi_{\mathrm{x,j,k}}^{(2)}(0, \omega, -\omega) E_{\mathrm{j}}(\omega) E_{\mathrm{k}}^{*}(\omega) \tag{2.3}$$

where i, j, and k are Cartesian coordinates. It can be seen that the non-linear polarisation is proportional to the strength of the incident light. The non-linear susceptibility of an EO crystal can be presented in a matrix equation, in order to determine the polarisation of the non-linear medium when performing OR;

$$\begin{pmatrix} P_{\mathrm{x}} \\ P_{\mathrm{y}} \\ P_{\mathrm{z}} \end{pmatrix} = 2\epsilon_0 \begin{pmatrix} d_{11} & d_{12} & d_{13} & d_{14} & d_{15} & d_{16} \\ d_{21} & d_{22} & d_{23} & d_{24} & d_{25} & d_{26} \\ d_{31} & d_{32} & d_{33} & d_{34} & d_{35} & d_{36} \end{pmatrix} \begin{pmatrix} E_{\mathrm{x}}^2 \\ E_{\mathrm{y}}^2 \\ E_{\mathrm{z}}^2 \\ 2E_{\mathrm{y}}E_{\mathrm{z}} \\ 2E_{\mathrm{z}}E_{\mathrm{x}} \\ 2E_{\mathrm{x}}E_{\mathrm{y}} \end{pmatrix} \tag{2.4}$$

This can be simplified due to many of the values in the d-matrix becoming zero value terms because of the crystal symmetry. Furthermore, several remaining terms may be equivalent. Which terms these are depend upon the crystal class. An example of this is given for LN in Equation (2.5). The intensity of generated THz is dependant upon the angle of incident field direction within the EO lattice structure. Maximum power can be generated when the field is aligned to the crystal lattice bonds [1, 42].

2.2.1.1 Lithium Niobate

LN is an EO crystal, seen in Figure 2.4a and b, in crystal class 3m (ditrigonal-pyramidal). This means it has three unique mirror planes, seen in Figure 2.4c. None of these mirror planes pass through the centre of the crystal unit cell, making it a non-centrosymmetric crystal. It was first discovered to be ferroelectric in 1949, and is also piezoelectric [43]. It is commonly used for EO applications due to its high transparency over a broad frequency range, and large susceptibility coefficient of 27 $\mathrm{pmV_{-1}}$ [22]. A drawback to its use is a large index mismatch - for extraordinary rays at ~2 THz the index is ~5, whereas at ~200 THz its index is ~2.1 [44]. This makes OR difficult. However, the large susceptibility coefficient helps it overcome the issues created by the large index mismatch by allowing methods such as wavefront tilting to be employed [1]. The dominant form of THz absorption in an EO crystal are transverse optical phonon processes, and

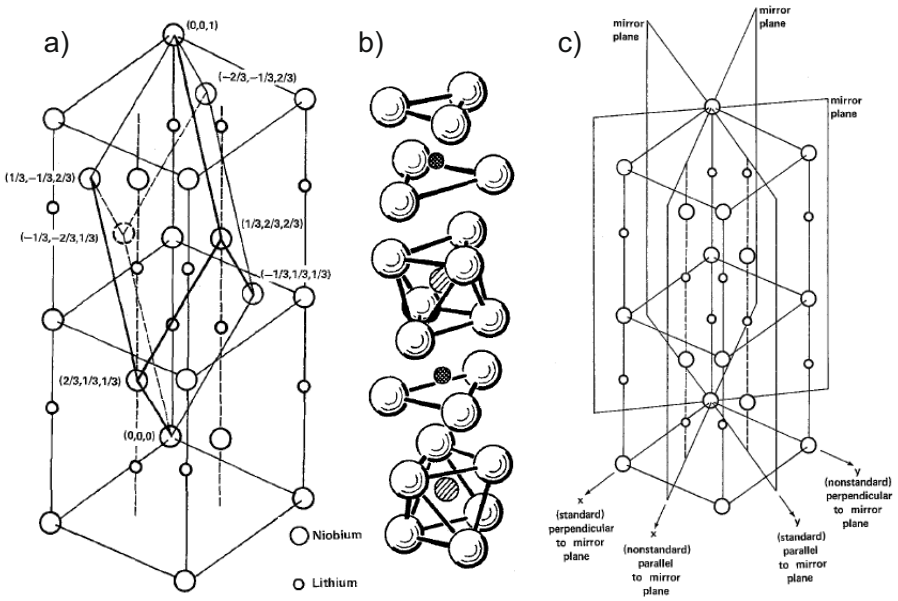

Figure 2.4: Diagrams showing the LN crystal structure. a) shows the rhombohedral unit cell, in relation to the hexagonal unit cell, b) details how the oxygen atoms relate to the lithium and niobium atoms, and c) shows the three mirror planes the crystal has, and relates four planes used to describe tensor properties to them. Figures taken from [43].

the lowest frequency this occurs at in LN is 7.7 THz, above the range for many THz based applications [45]. Due to these properties, LN is commonly used for operations such as OPA. Often, LN is doped with Magnesium Oxide (MgO), which achieves less loss and less fluctuation in the refractive index across the crystal while increasing the damage threshold [46, 47].

Many applications employ Lithium Niobate On Insulator (LNOI) for high density photonic circuits, such as EO modulators and wavelength conversion devices. Waveguides are often key components of such circuits. The high disparity between LN and Silicon Dioxide (SiO_2) indices leads to confined and well guided light [48].

To look at the non-linear polarisation of LN, the d-matrix of Equation (2.4) must be analysed. Due to the symmetry planes of the LN crystal lattice, some of the matrix components become zero terms, while other non-zero terms become matching values, resulting in Equation (2.5).

$$\begin{pmatrix} P_{\mathrm{x}} \\ P_{\mathrm{y}} \\ P_{\mathrm{z}} \end{pmatrix} = 2\epsilon_0 \begin{pmatrix} 0 & 0 & 0 & 0 & d_{15} & -d_{22} \\ -d_{22} & d_{22} & 0 & d_{15} & 0 & 0 \\ d_{15} & d_{15} & d_{33} & 0 & 0 & 0 \end{pmatrix} \begin{pmatrix} E_{\mathrm{x}}^2 \\ E_{\mathrm{y}}^2 \\ E_{\mathrm{z}}^2 \\ 2E_{\mathrm{y}}E_{\mathrm{z}} \\ 2E_{\mathrm{z}}E_{\mathrm{x}} \\ 2E_{\mathrm{x}}E_{\mathrm{y}} \end{pmatrix} \tag{2.5}$$

The final form is then;

$$P_{\mathrm{x}} = 4\epsilon_0(d_{15}E_{\mathrm{z}}E_{\mathrm{x}} - d_{22}E_{\mathrm{x}}E_{\mathrm{y}}) \tag{2.6}$$

$$P_{\mathrm{y}} = 2\epsilon_0(-d_{22}E_{\mathrm{x}}^2 + d_{22}E_{\mathrm{y}}^2 + 2d_{15}E_{\mathrm{y}}E_{\mathrm{z}}) \tag{2.7}$$

$$P_{\mathrm{z}} = 2\epsilon_0(d_{15}E_{\mathrm{x}}^2 + d_{15}E_{\mathrm{y}}^2 + d_{33}E_{\mathrm{z}}^2) \tag{2.8}$$

It can be seen that the largest second order term, d_{33}, lies in the z plane. If the crystal is used in such a way that $E_{\mathrm{x}} = E_{\mathrm{y}} = 0$, then the input is pure E_{z} and the output is pure P_{z}. This allows OR to lie along the same polarisation direction as the input beam [1].

2.2.2 Optical Rectification

OR is a second order non-linear method of generating THz. An incident field from EM waves on a material will cause electron movement, resulting in radiation emission. If a field is incident upon a noncentrosymmetric crystal, such as LN, and strong enough to create a large dipole displacement, non-linear electron motion occurs, giving rise to both OR and Second Harmonic Generation (SHG).

In OR, the varying polarisation causes the radiation emission, where the Gaussian non-linear polarisation is proportional to the intensity of the incident EM wave. If the incident wave is a short pulse, the pulse shape is duplicated by the rectified wave, with bandwidth inverse to the pulse duration. When performing ultrashort pulses for ultrabroadband, which is where the pulse bandwidth extends beyond 10 THz, the emission bandwidth will include TO phonon resonances. The output is dependant upon polarisation position; if the refractive indices of the medium at both source and emission frequencies are matched, then the emission will amplify until the pump is depleted. Otherwise the emission is subject to walk-off length; the distance until destructive interference occurs. OR works better at lower temperatures as less THz radiation is absorbed by the EO crystal [1].

2.2.3 Second Harmonic Generation

SHG is a second order non-linear process, in which the fundamental wave creates an additional wave at its own second harmonic frequency via interaction with the susceptibility of an EO crystal [49]. The SHG intensity is proportional to the second order polarisation [50]. It is a widely adopted method of creating coherent and tunable EM radiation, although requires a long interaction length

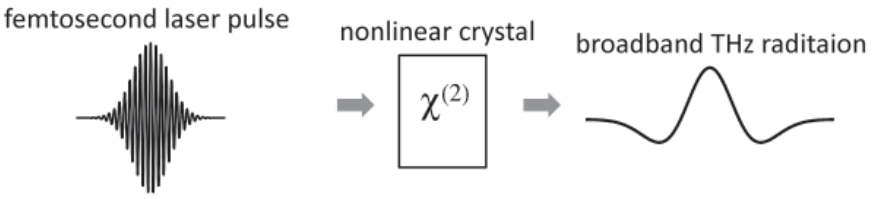

Figure 2.5: The OR process. Figure taken from [1].

and high pump power to be efficient. A balance between efficiency and tunability must be accommodated in a conventional non-linear arrangement [51].

The power of the fundamental is transferred to the Second Harmonic (SH) wave, proportional to both second order non-linearity and the intensity. This has has been demonstrated using a LN. One method is by mixing counter propagating waves, resulting in the generated SH emitting vertically [52]. Another uses Quasi Phase Matching (QPM), which involves using an alternating orientation of crystal structure at regular intervals to reverse the impact of phase mismatch, and has been exemplified by use of Periodically Poled Lithium Niobate (PPLN) as a successful SHG approach. By regularly changing the sign of the non-linear coefficient, PPLN effectively inverts the phase, causing the SHG signal to grow in power by allowing co-propagation between it and the fundamental [49]. More recently, waveguided LN has allowed the SHG method of generating light to flourish, due to utilising features such as high mode confinement and thermo-optic birefringence [51, 53].

2.2.4 Difference Frequency Generation

DFG is a method of CW THz generation. When two copropagating EM waves reach a noncentrosymmetric crystal, these waves are interact in a second order non-linear process, resulting in a single output wave which has a frequency of the difference in frequency between the two input waves. In fact, OR can be considered as DFG of all the frequency components of a pulse [1].

If, for example, input waves of 199 and 201 THz were used, then an output wave with a frequency of 2 THz would be obtained.

$$\omega_{\mathrm{THz}} = \omega_1 - \omega_2,\ \omega_1 > \omega_2 \tag{2.9}$$

The separate electric fields from each incident wave cause the crystal to polarise at both the sum and difference frequencies, however, it is the difference which creates the THz radiation, so the sum frequency is often ignored. The input waves must be linearly polarised in the same direction, so when travelling together the interference pattern then results in a 'beating' frequency equivalent to the output wave [1, 10].

Resonant cavity DFG has been demonstrated inside a QCL using pulsed pump beams. For intra-cavity DFG ordinarily, the high absorption and limited

intensity of pump beams hampers such attempts. However, by designing the active non-linear semiconductor with quantum wells, lasing gain is attained along with a large second order susceptibility, offsetting the original problems and obtaining a massive confinement [10].

2.2.4.1 Phase Matching

In general, a material will have a different refractive index at different frequencies. The result of this is that waves at different frequencies propagate through the crystal at different velocities, ultimately leading to destructive interference. Phase matching involves equating the velocities of the waves travelling through the waveguide in order to delay the waves from ending up out of phase for as long as possible.

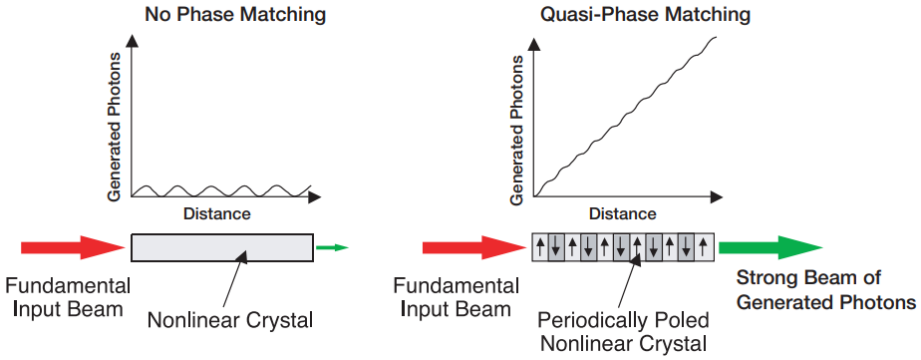

Figure 2.6: A diagram comparing QPM of a periodically poled EO crystal to a single pass crystal. Figure taken from [54].

Phase matching has been shown to be an issue with LN and its vastly different refractive index at NIR and THz frequencies. This causes the NIR wave to arrive at the crystal edge before the THz wave [1]. A common method of working around this involves using PPLN, where the changing polarisation generates a THz field over half of the number of domains along the PPLN crystal. This is employed via QPM, seen in Figure 2.6, where the alternating crystal structure reverses the phase mismatch at regularly spaced intervals. The frequency can be varied by adjusting the domain length [55]. A tilted wavefront approach has also successfully produced phase matching results for THz generation in LN [56]. PPLN and wavefront tilting are explained further in Section 2.4.

The maximum distance two waves of differing frequencies can co-propagate through a device until destructive interference occurs is called walk off length. To maximise the walk off length, the waves must be phase matched. Ideally, the phase matching condition would be satisfied completely, occurring when the optical and THz refractive indices are exactly equal. In reality however, a perfectly matched system is not realistic, due to the limitations of micro

and nano fabrication, and the best that can be done is to minimise the phase discrepancy as much as possible.

A way of extending the walk-off length is by mode matching. Mode matching involves comparing the electric fields of a device at the different frequencies it is being operated at and ensuring that the wavefronts of the different traversing waves are aligned with each other.

Walk off length is different from spatial walk off. Spatial walk off is where the wave intensity starts distributing away the beam axis, caused by travel through an anisotropic medium by the differing indices. Angles are typically in the range of milliradians. This can also be corrected by phase matching. By correcting the spatial walk off, a better walk off length can be achieved [1, 57].

2.3 Waveguiding

A waveguide is a physical construct which contains a wave as it travels towards its destination, rather than letting it expand into open space and lose intensity. There are waveguides for both acoustic and EM waves. For EM waveguides at radio frequencies, hollow metal pipes are used which reflect the waves within the empty space. Dielectric waveguides, used at higher frequencies, are similar in principle but are the shape of a slab or channel of dielectric material rather than a hollow metal pipe. A dielectric material channels electric field without being conductive, in other words without electron flow [58]. An optical fibre is an example of a dielectric waveguide. This type of waveguide works by taking advantage of a high index material, called the core. By coating it with a low index material, referred to as cladding, the waves are contained in the high index material by total internal reflection. The most significant loss mechanisms for optical waveguides are scattering and absorption losses [59].

2.3.1 Complex Refractive Indices

The refractive index of a material governs the factors of the velocity of a wave through the medium and the attenuation the wave experiences. It changes depending upon the wavelength incident upon a given material. This can be critical when dealing with an effect such as walk-off length. The complex form is given as:

$$N = n + ik \tag{2.10}$$

where n is the real part affecting velocity and ik is the imaginary part known as the extinction coefficient, affecting attenuation.

The real part n, which is related to the velocity of a wave through a material and causes refraction, is derived from a propagating electric field:

$$\frac{d^2E}{dx^2} = \frac{1}{v^2}\frac{d^2E}{dt^2} \tag{2.11}$$

where E is electric field and v is velocity. $1/v^2$ can be replaced by $\varepsilon\mu$, where ε is the medium permittivity and μ is the medium permeability. This means that;

$$n^2 = \varepsilon_\mathrm{r}\mu_\mathrm{r} = \frac{\varepsilon\mu}{\varepsilon_0\mu_0} \tag{2.12}$$

where ε_r and μ_r are relative permittivity and permeability, and ε_0 and μ_0 are free space permittivity and permeability. This shows that refractive index is temperature dependant, as permittivity influenced by temperature. When assuming $\mu = \mu_0$,

$$n = \sqrt{\varepsilon_\mathrm{r}} = \sqrt{\frac{\varepsilon}{\varepsilon_0}} \tag{2.13}$$

[60, 61].

A wave travelling through a medium also experiences absorption. This can be derived by examining the electric field as it passes through a medium.

$$E = E_0 cos(\omega t - KL) \tag{2.14}$$

E_0 is the initial electric field intensity, ω is defined as $2\pi f$ where f is frequency, t is the period of the wave ($\frac{1}{f}$), K is defined as $\frac{2\pi}{\lambda}$ where λ is wavelength, and L is the distance from the starting position. Equation (2.14) can be rewritten to use N.

$$E = E_0 cos(\omega(t - \frac{NL}{c})) \tag{2.15}$$

Speed of light is defined here as c. When taking the refractive index N as complex, and rewriting Equation (2.15) in exponential form, Equation (2.16) is reached.

$$E = E_0 e^{-\frac{\omega k L}{c}} e^{\omega i(t - \frac{nL}{c})} \tag{2.16}$$

Here, it is shown that the amplitude of the electric field, given by $E_0 e^{-\frac{\omega k L}{c}}$ is attenuated exponentially [60].

The absorption a wave experiences can also be provided by looking at the Beer-Lambert law:

$$I = I_0 e^{-\alpha L} \tag{2.17}$$

where I is intensity, I_0 is the intensity at the material boundary the ray enters at, and α is the absorption coefficient. Absorption coefficient and extinction coefficient are related by the following equation:

$$k = \frac{\alpha c}{4\pi f} = \frac{\alpha c}{2\omega} \tag{2.18}$$

This shows that the frequency of the wave passing though a material affects the amount of attenuation experienced [61, 62].

2.3.2 Styles of Dielectric Waveguide

2.3.2.1 Slab Waveguide

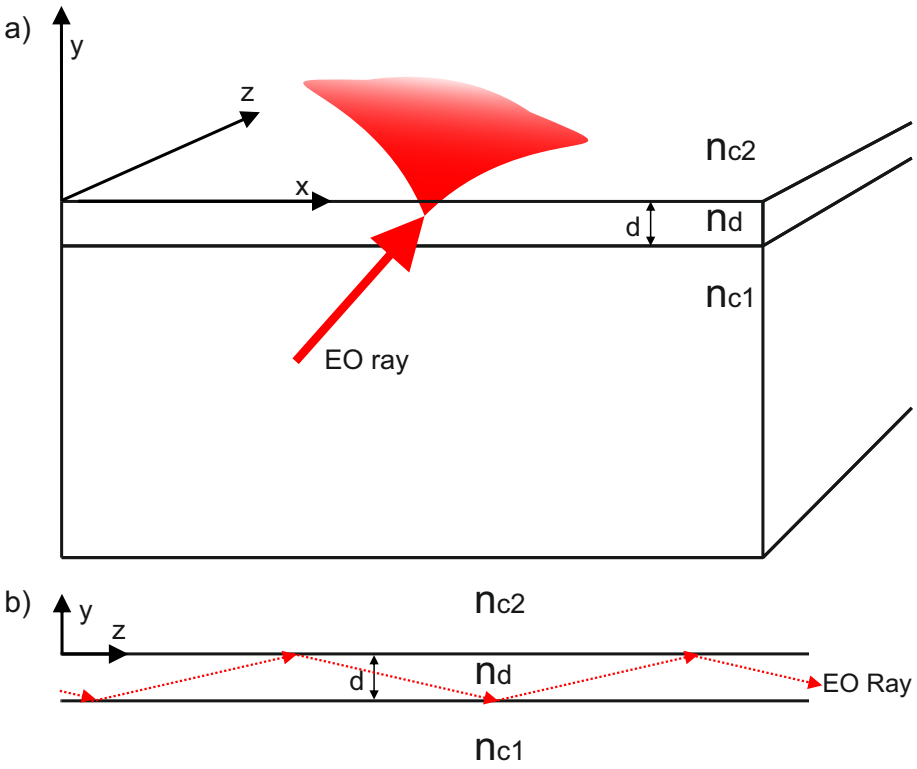

Figure 2.7: Diagrams of a slab waveguide geometry, where $n_d > n_{c1}$ and n_{c2}. a) shows how an EO wave enters the slab and disperses in the x direction while propagating through z. b) displays how light travels through a slab waveguide via total internal reflection [63].

A slab waveguide, also known as a planar waveguide, is a high index dielectric material confined at the top and bottom by cladding of lower index materials [64], shown in Figure 2.7a. Below the waveguide the material is referred to as the substrate, while above is the cover. If the refractive index of the substrate and cover are the same, the waveguide is referred to as symmetrical. Otherwise it is asymmetrical [63]. Due to the planar geometry of this waveguide, light is only guided in one direction, which in Figure 2.7a is the y plane. A two dimensional image of light propagation is shown in Figure 2.7b.

When light is travelling through a waveguide, electric and magnetic fields are created through the structure. The areas where the field distribution is unchanging in the direction of light propagation are called modes. Only the phase and power of the signal can change in a mode [65]. Depending upon the

waveguide, many modes can exist, or the waveguide can be designed specifically to support a single mode, called the fundamental mode. How many modes exist depends upon multiple factors. These include the thickness of the core layer, the refractive indices of the core and cladding layers, and the wavelength of light traversing through the waveguide [66]. Cladding modes may also exist, in the event of light escaping the waveguide or not coupling into the core upon insertion. This light is unguided and can be detrimental to performance, either by coupling with the core modes or by providing an undesired additional signal to a detector at the end of the waveguide [67, 68].

2.3.2.2 Channel Waveguides

A channel waveguide is like a planar waveguide but also confined at the sides [48]. This results in the EM wave being guided in two dimensions, while propagation is restricted to one - the direction of the channel. This type of waveguide is often designed to be single mode [69] [48]. Fabrication techniques can restrict this style of waveguide due to the small sizes required [70].

The simplest channel waveguide is simply a dielectric ridge, or strip, atop the lower index insulator material, shown Figure 2.8a. In this scenario, the wave is confined both above and at the sides by an interface with a cladding material which has a much lower refractive index than the dielectric [48]. Air is sometimes used as the cladding. When completely clad by a single insulator material, a channel waveguide may be referred to as a buried waveguide.

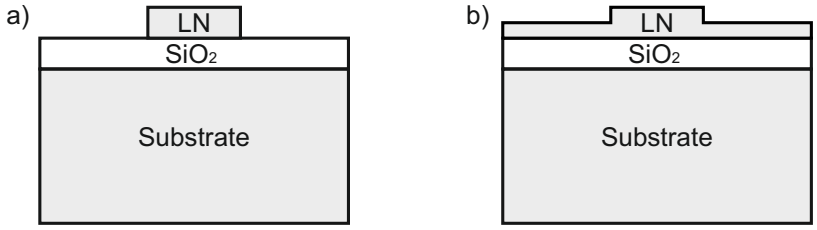

Figure 2.8: A diagram using LNOI to illustrate cross-sections of a) a ridge waveguide, and b) a rib waveguide.

The dimensions of a waveguide are important - the size and shape of the waveguide affects the beam profile needed to provide efficient light injection into the waveguide, in addition to altering the mode area, which is related to non-linear interaction strength [71]. High losses can be caused by surface roughness, leading to scattering and waveguide mode asymmetry [72]. While channel waveguides can support a curved shape, the induced bend loss must be taken into account. A smaller bend radius will induce a higher loss [48].

LNOI has been found to make an effective channel waveguide. Consisting of a single crystal thin film layer atop a low index layer, often SiO_2, it provides

strong single mode EM wave guidance with high confinement due to the large disparity in refractive indices. Consequently, it is often used for integrated photonic circuits, offering a low consumption of power at a high integration density [48].

Channel waveguides are also commonly used in lasers such as QCLs. Using a channel waveguide with reflective end surfaces, the Fresnel reflections cause a build up of light inside the waveguide cavity until powerful enough to overcome the losses and emit through the end surface [73].

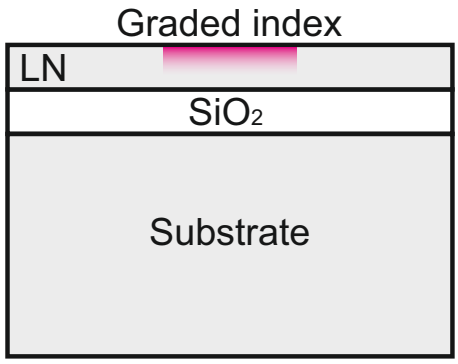

Figure 2.9: A diagram using LNOI to illustrate the cross-section of a graded index waveguide, fabricated via Proton Exchange (PE) or metal ion diffusion. The more intensely coloured area has a more significant index change from the surrounding LN.

Various fabrication techniques for the creation of channel waveguides have resulted in variations of the base concept. The standard ridge is simple to etch [74], while other techniques such as PE create a ridge with a graded index rather than a hard step, and the channel embedded into the substrate [75], as seen in Figure 2.9. PE waveguides involve replacing crystal ions with protons. This is often demonstrated using LN, where the lithium ions are replaced with protons. This is done by immersing the crystal in molten benzoic acid, being careful to avoid crystal cracking [76]. The replacement of the lithium ions with protons causes the refractive index to rise. A post-exchange anneal has been shown to provide more favourable qualities by providing a greater index gradient. The gradient follows the number and depth of exchanged protons, displaying a Gaussian curvature [77]. An index gradient influences mode shape, and wave group velocity and dispersion [78]. Metal ion diffusion into an EO crystal is similar in result to PE waveguides, and has long been used in an effort to create low loss waveguides. LN is, again, often used as the crystal of choice, while the ion diffusion is usually performed with titanium, but sometimes done with with other metals such as nickel or vanadium. The metal is evaporated onto the EO crystal surface and then heated in an inert atmosphere. The metal width and thickness, heating temperature and heating time are factors used to influence the size of change in refractive index, in addition to the size

of the guiding area and the number of modes guided. A higher temperature equates to a higher diffusion rate. Like PE waveguides, the index follows a Gaussian curvature. Surface roughness from leftover oxide may lead to scattering losses [75, 79]. Ti-diffusion and proton exchanged LN waveguides are the most established technologies for LN waveguides [80]. The confinement is not high however, so for devices where high confinement is a priority, the waveguide must be etched.

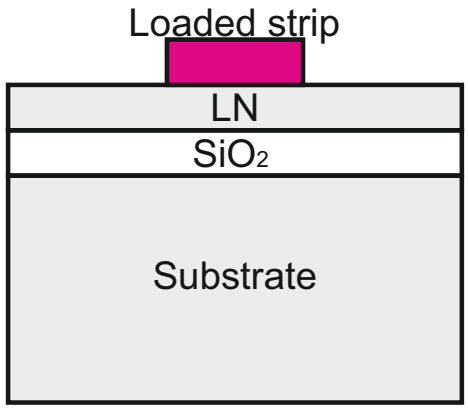

Figure 2.10: A diagram using LNOI to illustrate the cross-section of a strip loaded waveguide.

A strip loaded waveguide is another take on the standard channel waveguide, shown in Figure 2.10. A strip loaded waveguide is a high index planar waveguide, with a slightly lower index ridge atop it [64]. This strip provides lateral confinement [81]. The sidewall roughness is not as critical as most of the energy is in the slab rather than the strip, providing easier fabrication [64], and enabling complex structures to be designed using this type of waveguide, such as ring resonators and Bragg gratings [81]. An early example used a photoresist strip above glass [64]. More recent efforts have utilised LN for the slab, and materials such as silicon and titanium dioxide for the strip [48, 81].

2.3.2.3 Rib Waveguide

A variation on a channel waveguide is a rib waveguide. A rib waveguide is equivalent to a ridge waveguide atop a slab waveguide, shown in Figure 2.8a. This allows more space vertically for a mode while still providing confinement horizontally. It is similar to a strip loaded waveguide, except that the rib is made of the same material as the slab. The propagation losses of a rib waveguide are lower [82] and they are less sensitive to sidewall roughness [83]. The width of the rib has been shown to influence how much of the mode is guided between the rib and the planar section of the waveguide [84]. Rib waveguides have been demonstrated using PPLN [72] and LNOI [85].

2.3.2.4 Surface Plasmon Waveguides

An Surface Plasmon Polariton (SPP) waveguide uses metal for the cladding material. Surface plasmons are collective charge oscillations at the interface between a metal and a dielectric [86], caused because metals have plasma like properties at optical frequencies [87]. When a plasmon resonates with an EM wave, it causes an excitation called a polariton [88]. This SPP is an oscillation of surface charge density coupled to the EM fields. When the dielectric and metal have opposite permeabilities to each other, the SPP exists as a Transverse Electric (TE) wave, which travels along the material interface. Metal dielectric interfaces are commonly used for sensors due to the detectable excitations created at the interface [89].

SPP waveguides suffer from ohmic losses, leading to high attenuation and low mode conversion efficiency. This is counterbalanced by the tight confinement provided [19]. SPPs have been demostrated in THz frequency QCLs, reducing the wavefront size so the emission becomes narrowbeam [90]. Using a waveguide in a semi-insulating surface plasmon style in a high THz gain QCL to reduce the mode overlap with doped semiconductor cladding was first demonstrated in 2001 [9], while a double metal waveguide appeared shortly after [91] [92]. Dielectric waveguides like those used in solid state lasers cannot be used in QCLs due to the high wave penetration depth in comparison to the size of the active region [1].

2.3.3 Mode Shape

The mode shape between a symmetric slab dielectric waveguide and an SPP waveguide of similar dimensions differ. It can be seen from Figure 2.11a that the slab mode profile is most intense in the centre of the dielectric material, providing a Gaussian-like electric field across the vertical cross-section. In contrast, Figure 2.11b shows the surface plasmons formed at the insulator-metal boundaries act to pin the high electric-field at the boundary, resulting in a near-constant electric field through a vertical cross-section within the waveguide.

Using the slab waveguide diagram in Figure 2.11a and taking the propagation direction as through the z plane, there are electric field components in the x and y planes, as electric field direction is perpendicular to the propagation direction. In the y direction, there is confinement of the EO wave. Consequently, there are three regions to consider through y; the slab waveguide, and the cladding areas both above and below.

Within the dielectric slab, the fundamental mode is most intense in the centre of the waveguide. The intensity decreases in any direction away from this central point. Therefore, taking the centre of the dielectric slab as the origin in the plane perpendicular to the two cladding interfaces, the field strength resembles a cosine function:

$$E_{\mathrm{d}} = C_{\mathrm{d}} \cos\left(k_{\mathrm{y}} S_{\mathrm{y}}\right) \tag{2.19}$$

where E_{d} is the electric field strength in the dielectric slab, C_{d} is a constant,

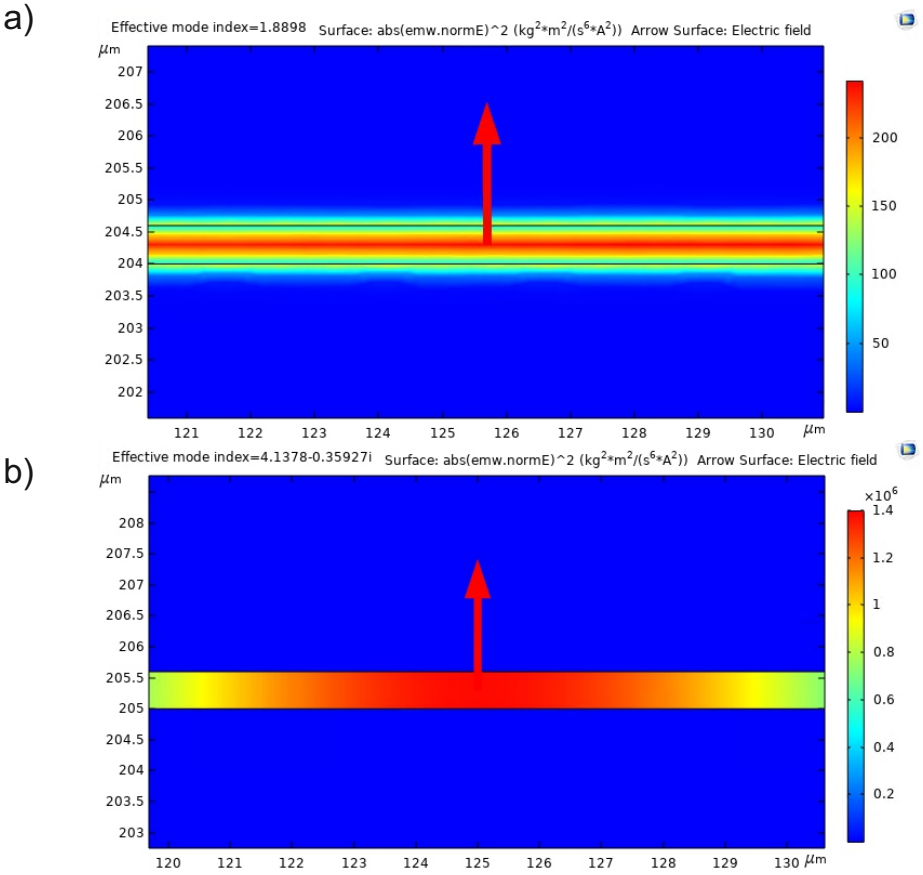

Figure 2.11: A model, simulated in COMSOL, of a) a dielectric planar waveguide, with the TE mode intensity displayed. The model is a thin film of LN with SiO_2 cladding underneath and above. In b) the model shows an SPP waveguide, with the TE mode intensity displayed. The model is a thin film of LN with gold cladding above and below. For both sub-figures, the EO wave propagation direction is into the page, and are simulated at 193 THz with vertical polarisation. The brighter colours represent higher TE mode intensity. The red arrows display the direction of the electric field. Simulated using device widths (along the x axis) of 50 µm, providing nominal horizontal confinement. Small sections of the widths are shown to highlight the areas of interest.

k_{y} is the propagation constant of the slab in the y plane, and S_{y} is the distance in the y plane from the mode centre.

When considering the field strength in the cladding, an exponential decay provides a better representation:

$$E_{\mathrm{c}} = C_{\mathrm{c}} e^{\pm\alpha(S_{\mathrm{y}} \pm \frac{d}{2})} \tag{2.20}$$

where E_c is the electric field strength in the cladding, C_c is a constant, α is a decay constant for the cladding, and d is the thickness of the slab waveguide, as the condition for this equation occurs when the cladding starts.

While these equations explain the shape of the mode, they do not provide the condition for a mode forming. When considering the total electric field of the wave, which is dependant upon its frequency and the permeability and permittivity of the material it is passing through, the following equations can be formed:

$$k_x^2 + k_y^2 = \omega^2 \mu_d \epsilon_d \tag{2.21}$$

$$-\alpha^2 + k_z^2 = \omega^2 \mu_c \epsilon_c \tag{2.22}$$

where k_x and k_z are the propagation constants in the x and z planes respectively, ω is angular frequency, μ_d and ϵ_d are the permeability and permittivity of the dielectric slab respectively, and μ_c and ϵ_c are the permeability and permittivity of the cladding respectively. By considering the electric and magnetic fields continuous at the cladding interfaces:

$$C_c = C_d \cos\left(k_y \frac{d}{2}\right) \tag{2.23}$$

$$\frac{\alpha}{\mu_c} C_c = C_d \frac{k_y}{\mu_d} \sin\left(k_y \frac{d}{2}\right) \tag{2.24}$$

Using Equation (2.23) and Equation (2.24), the guidance equation is found:

$$\alpha = \frac{\mu_c}{\mu_d} k_y \tan\left(k_y \frac{d}{2}\right) \tag{2.25}$$

The electric field strength for a symmetrical slab waveguide guiding a fundamental mode is displayed in Figure 2.12.

The above equations also hold true for an even number of modes in the waveguide more than the fundamental. For an odd number, the cosine function of Equation (2.19) must be changed to a sine function, due to the modes not being centred between the cladding, before following the equations through. This in turn adjusts the equations for matched field strengths at the interfaces [65].

In an SPP waveguide, the propagation of any modes into the metal layers depends upon the frequency of the wave through the metal in comparison to the frequency through the dielectric. When the frequencies are equal, as they are in the waveguide proposed in Chapter 3, then the propagation constant of the metal layer disappears, and its induced polarisation density becomes opposite to the electric field;

$$P_{\text{metal}} = -\epsilon_0 E \tag{2.26}$$

Hence, no mode propagates through the metal. [87]

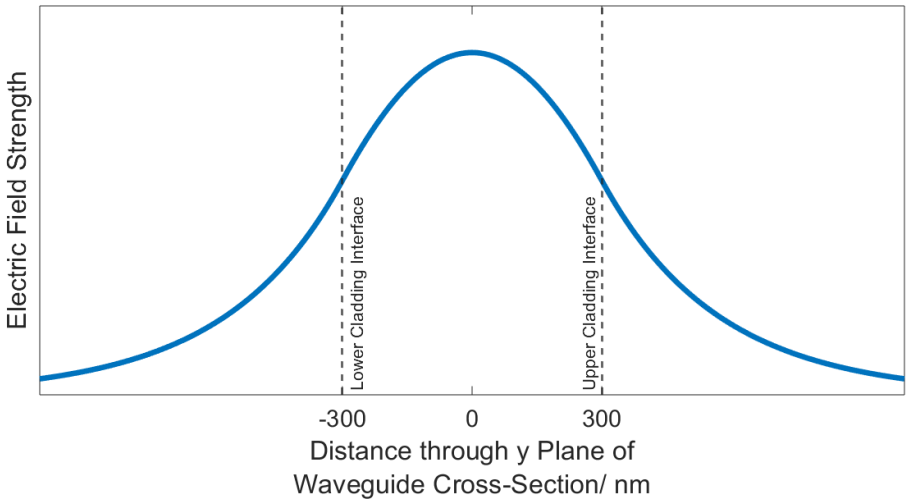

Figure 2.12: A plot showing the field strength through a slab waveguide in the y direction when matched to a fundamental mode. The cladding interfaces are set at the distances used in the device introduced in Chapter 3.

2.3.4 Coupling from Optical Fibre to Waveguide

For a waveguide, size mismatch between itself and an optical fibre is often a large source of coupling loss. There are two main methods of coupling to waveguides. The first is edge coupling, where the wave is pointed directly at the side of the waveguide. This is the simplest form of coupling. It requires high quality facets, and has the advantage of a low polarisation dependence. The second method is vertical coupling. This is where the beam is pointed at the top or bottom of the waveguide, and a coupling structure adjusts the beam direction into the waveguide. Various adaptations of these two methods have been experimented with, including tapered or trident structures of waveguide, and different styles of diffraction gratings [93]. Gratings have the advantage of a high alignment tolerance [94].

For a simple tapered edge coupler, a large collecting facet appears on the end of the waveguide to collect the wave, shrinking down to the waveguide size over a short distance. However, while this assists in collecting the light, the shape of the wave changes along the diminishing width of the coupler, resulting in mode conversion loss in addition to any facet reflection loss [93].

Another way to reduce coupling losses is the use of anti-reflection coating [94].

2.3.4.1 Spot Size Converter

A standard optical fibre (SMF-28) has a single mode transmission with an attenuation potentially lower than 0.18 dB/km at a wavelength of 1.55 µm [93].

The end of the fibre can be modified to alter the spot size of the emergent EM beam from it, portrayed in Figure 2.13.

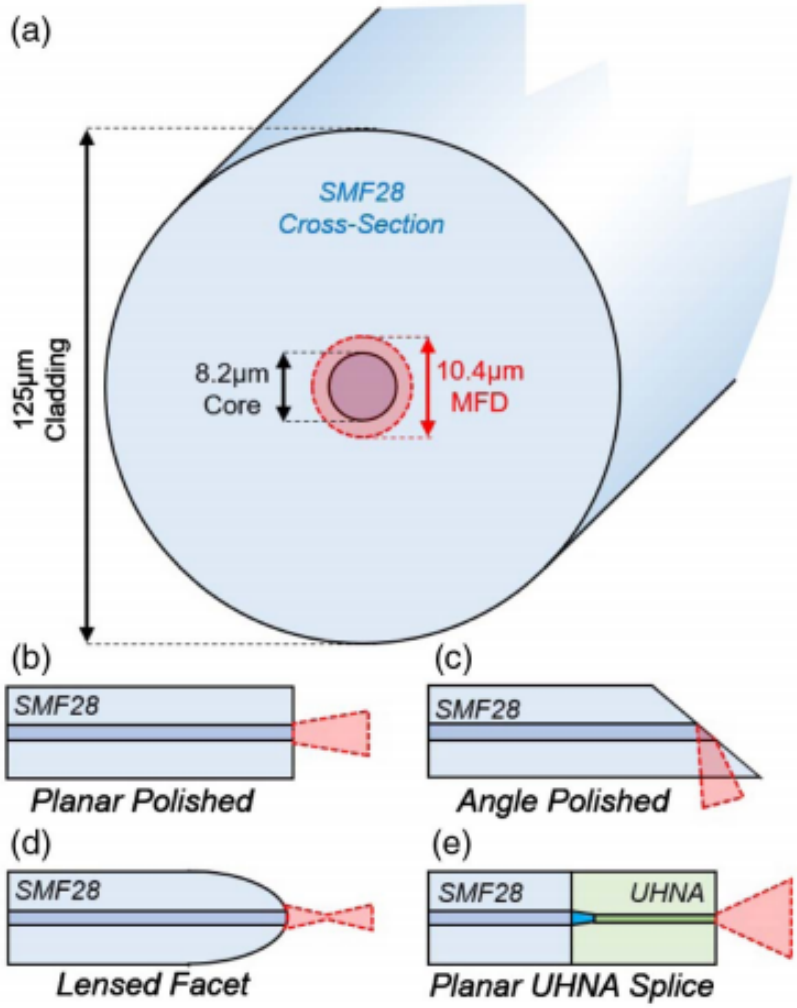

Figure 2.13: (a) shows a cross-section of a standard telecommunications optical fibre, while (b) to (e) depict various alterations to the fibre end in order to modify the emitted beam. *SMF* - Single Mode Fibre, *MFD* - Mode Field Diameter, *UHNA* - Ultra-High Numerical Aperture. Figure taken from [93].

Of particular interest to the work in this thesis is the lensed facet method depicted in Figure 2.13d. The convex facet, achievable via polishing or laser ablating, focuses the transmitted beam from the 10 µm aperture to a spot size of only 2 µm at around 30 µm from the fibre; ideal for a high modal overlap beam into a small waveguide. While this method has high efficiency, it is hard

to successfully align.

Other methods of coupling from a single mode fibre include a planar polish (Figure 2.13b) of the fibre to give a symmetric beam profile. While simple, the emission profile of this fibre end does not lead to a small spot size. Making the facet angled (Figure 2.13c) by up to 40° instead facilitates total internal reflection, causing the beam to come out in a direction approaching orthogonal to the fibre, useful for coupling into gratings from above, which could be experimented with to improve coupling from the device introduced in Chapter 3. An ultra high numerical aperture (Figure 2.13e), which involves a high index between the core and cladding, is not so relevant due to its use for frequencies of only a few gigahertz [93].

2.3.5 Lithium Niobate Waveguides in the Optical and Near Infra-Red Regimes

LN waveguides have long been demonstrated operating outside the THz range. Using the tight confinement of modes available, LN waveguides have displayed large non-linear interaction in the optical and NIR regimes.

Since as early as 1976, LN has been considered for thin film guided optics for telecommunications integrated systems. Optical fibres were set to replace coaxial lines, and integrated optics were being investigated as a way of incorporating active functions such as high speed switching and data modulation. Thin films were already commonplace due to their use for filters and anti-reflection in classical optics. By depositing a film on top of a lower index substrate, an optical mode could be guided. This mode was then confined laterally by reducing the thickness of the film on both sides of the guiding area, resulting in a ridge waveguide. The lower refractive index of the substrate causes total internal reflection of light in the layer of film, while the low height of the film results in constructive interference of successive reflections, causing propagation. Loss from absorption and scattering were considered issues to be addressed in any such waveguide. While many materials were considered, LN, particularly when doped with titanium, showcased itself for its high EO properties and low optical loss. However, the high insertion loss between the high index LN and low index optical fibre, or air, caused issues [95].

Over the course of the advance into integrated systems, LN waveguides have become a more explored area. For example, a recent simulated experiment compared different types of thin film LN waveguides at 1.55 µm wavelength, discussing the performances of ridge, PE and strip loaded waveguides at different thicknesses [48]. There is also a keen interest into LNOI usage, which is considered “a rapidly developing platform”. LNOI offers the useful material properties of LN while also providing high optical confinement and integration density. Key technological advancements have been made towards using LNOI waveguides for integrated circuits, and it has been considered for applications in telecommunications and quantum photonics. However, a high cost per wafer is a limiting factor to its continued success [96].

Alternative approaches showcase an effort involving waveguided PPLN for SHG of 1.5 µm radiation by QPM, which is used to get around the need for long lengths and high pump powers for effective conversion. The efficiency, which increases with input power up to a maximum, peaks at 53% with an input greater than 200 mW, with losses as low as 0.03 dB/cm. The highest second order non-linear tensor component is used - d_{33}, and strong optical confinement is exploited. These effects are used in order to obtain a lower group velocity mismatch [53].

Options such as utilising temperature tuning have also been explored. While performing SHG, one example demonstrates conversion efficiencies comparable to using PPLN with an 8 mm long waveguide by using Z-cut LN for a high polarisation purity and creating a large spatial mode overlap by experimenting with the effective mode area to create a tight mode confinement [51].

In summary, LN waveguides at communication frequencies are an established field. To generate THz however, sophisticated phase matching needs to be exploited, several methods of which are detailed below.

2.4 Previous Terahertz Generation via Lithium Niobate Crystals

Using a picosecond laser to generate THz from LN was first demonstrated in 1971 [97]. To this day however, phase matching remains the key issue to overcome to make significant advancements in this area. There are options to facilitate working with this mismatch, such as tilting the wavefront, or channeling the waves through a waveguide. Many of these methods prefer pulsed wave operation.

2.4.1 Cherenkov Cones and Tilted Wavefronts in Lithium Niobate

Due to the large wave velocity mismatch at NIR and THz frequencies in LN, OR for THz using LN works poorly. Methods of causing the waves to successfully copropagate must be employed. Often, the technique used is by tilting the NIR wavefront, taking advantage of the emission angle of the THz.

The emission of THz during OR occurs in a conical shape behind the NIR source wave, shown in Figure 2.14a. This is known as a Cherenkov cone.

Classical Cherenkov radiation may occur at any frequency within dielectric materials, given that a free electron is made to travel faster than the phase velocity of light through the material it occurs in. This is known as the Cherenkov threshold. Reducing this threshold has been the interest of recent work, which claims that improvements in this area may lead more viable use of not only THz frequencies but other areas of the EM spectrum too. Exploitation of Cherenkov radiation has already led to its use for light sources and detectors as well as for medical imaging purposes [99]. The Cherenkov cone has been compared to the

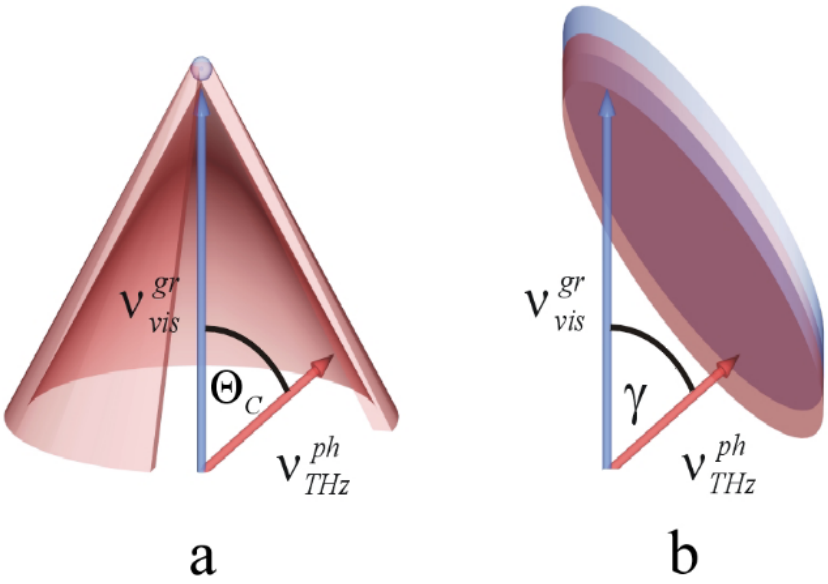

Figure 2.14: a) shows a Cherenkov cone for THz generation, while b) displays a tilted wavefront. Figure taken from [98].

collapsing sound waves which occur in a sonic boom, as the NIR wave similarly acts as a point source moving faster than the emitted THz waves [1, 22].

Cherenkov generation in EO media differs from classical Cherenkov radiation due to being a non-linear effect, and caused by a dipole moment instead of a point charge [100]. For THz frequencies, the cone is conditional upon the optical beam diameter being smaller than the THz wavelength [98]. The angle of the cone is given by:

$$\theta = \arccos \frac{v_{\mathrm{THz}}}{v_{\mathrm{NIR}}} \tag{2.27}$$

where θ is the angle and v is wave velocity. In LN, the angle is around 64° [22]. The crystal edge must be made the same angle as the cone angle to ease extraction of the THz emission. A cladding prism is often utilised for extraction to avoid internal reflection [101].

Non-linear Cherenkov radiation has been observed in both bulk and waveguided media [102]. An observed disadvantage in bulk media generation is that the width of the pump beam can lead to destructive interference due to phase mismatch of the generated THz along the width of the pump beam [103]. The phase mismatch can be countered by reducing the beam width, yet this causes a loss of interaction length. Using a waveguide has been shown to retain interaction lengths while simultaneously removing the phase mismatching issue [101].

It is ideal to have a narrow beam radius, or 'squeeze the light', as efficiency is proportional to power density. However, a limit is placed upon optical power so as to not damage the EO crystal [98]. Moreover, the bandwidth that can be used is limited [22]. The efficiency of using a Cherenkov cone to generate THz is low because THz created at one point in time cannot interact with THz created at a later point in time [98].

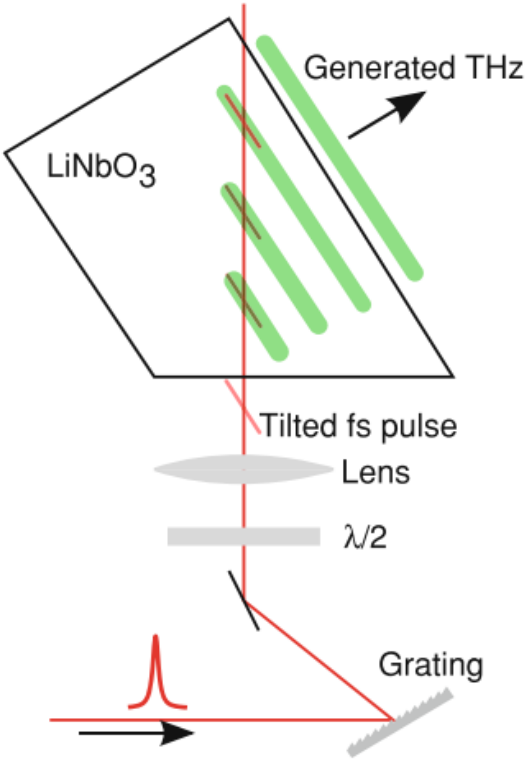

Figure 2.15: A diagram of using a diffraction grating to tilt the optical wavefront, and subsequent co-propagating THz generation in LN. Figure taken from [61].

A solution to this is tilting the optical wavefront to the same angle as the Cherenkov angle using a diffraction grating, shown in Figure 2.15, causing the optical and THz waves to co-propagate [1], as seen in fig. 2.14b. This results in a coherently amplifying THz signal, as THz generated at one point in time can interact with THz generated at a later point in time, boosting efficiency [98].

A distinct advantage of this is a large area generation of THz with a flat wavefront which is more easily manipulated than a conical wavefront. The tilted wavefront method is also not limited so much by a tightly confined optical beam size compared to using a Cherenkov cone [98].

A power of 20 µW was achieved when the tilted wavefront method was first

realised in 2003, with THz pulse energies of 98 pJ and an efficiency of less than 0.05×10^{-3}% [34]. Since then, 1.4 mJ pulse energies have been reached [104], while another experiment demonstrated a pump to pulse efficiency of 3.8% [105]. Cryogenic cooling is used to increase efficiency by reducing absorption [34].

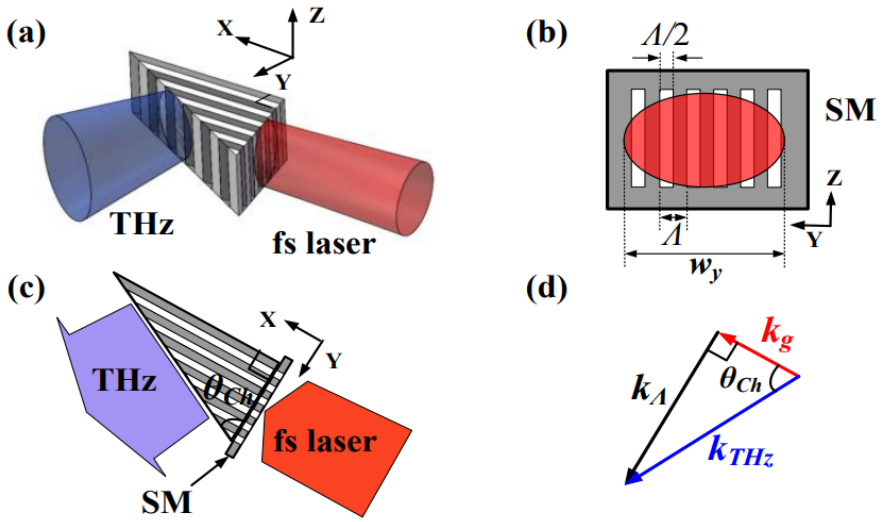

Figure 2.16: Diagrams explaining using PPLN with a shadow mask to generate THz radiation. a) shows areas of the PPLN with alternate non-linear coefficient using the light and dark areas. b) shows the shape of the shadow mask at the crystal face the pump beam enters, as well as the definition of a period of the slits. c) uses light and dark areas to illustrate illuminated areas of the crystal, as well as showing where the shadow mask is. d) illustrates the wave vectors of the technique. SM stands for Shadow Mask. Figure taken from [106].

A recent development is to perform this process using a shadow mask; a wall covering the front face of the LN with a series of periodic slits. This makes the OR process akin to using PPLN, and reduces phase mismatch along the plane of the crystal front face. The width of the periods of the slits in the mask determine the frequency, while the width of the optical beam determines the bandwidth. To have a tunable device, multiple masks with different slit size periods are required. Diagrams of this are displayed in Figure 2.16 [106].

2.4.2 Periodically Poled Lithium Niobate

PPLN has allowed QPM to be accomplished, resulting in high conversion efficiencies at low temperatures. A periodically poled material has regularly spaced layers of oppositely polarised orientation to the previous layer, resulting in a non-linear coefficient alternating between positive and negative with each period. OR of femtosecond pulses can then occur to generate THz [107].

QPM is achieved by using a crystal domain (a single orientation stripe, or half a period as denoted in Figure 2.17) comparable to the walk off length. A single domain generates a half cycle of THz field. Hence, a full period produces a full cycle of THz field. Using PPLN, the generated THz waveform is determined by the structure of the domains of the EO crystal. With a pulsed pump beam, the bandwidth of the THz wave is also determined by the PPLN, this time by the length of the crystal, as well as being affected by the pump beam spot size on the crystal [108].

Utilising surface emitting geometry in a rectangular PPLN structure can reduce THz absorption due to a reduced path length, with an emission normal to the input, shown in Figure 2.17. This however requires an extremely narrow beam width. Matching the domain width to the walk off length between the NIR and THz pulses has been demonstrated for finely tuned frequency emissions [107]. Surface emitting geometry for a waveguide has also been utilised for DFG in PPLN in CW [109], with advantages of little divergence of the THz wave, and having the optical and THz waves separated in space. Each spatial harmonic creates Cherenkov waves, and the low path length of the geometry in comparison to the THz wavelength means that the radiation will emit in phase [110]. The modulation of the structure can help mitigate the destructive interference of the THz waves to a limited extent [111]. It was proven that this method was more efficient than using a collinear approach [110].

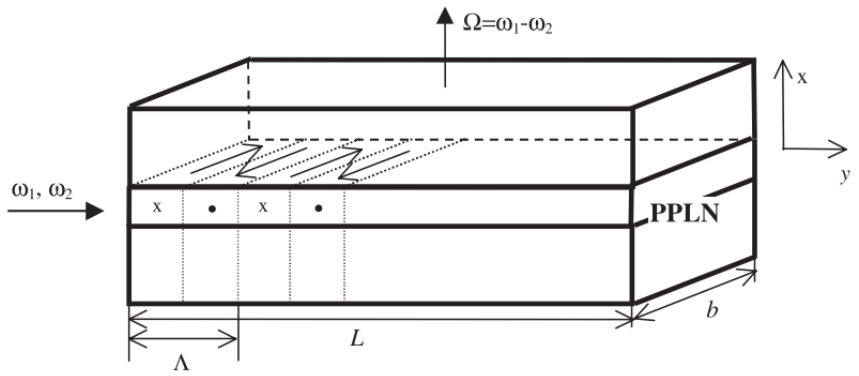

Figure 2.17: The surface emitting geometry of a PPLN device used to create THz using DFG. Λ marks one period. Figure taken from [110].

DFG in a PPLN waveguide has been extended to using bulk crystal by using a slant stripe composure, which achieves QPM in perpendicular directions to both NIR and THz propagation directions, shown in Figure 2.18 [111].

An alternate option is a prism shaped PPLN crystal. The optical beam travels parallel to the domains and is polarised vertically. The separate domains then obtain their own THz fields which will constructively interfere, giving rise to a quasi-monochromatic wave emission. The emission is determined by the period of length of two opposite domains and bandwidth inversely proportional

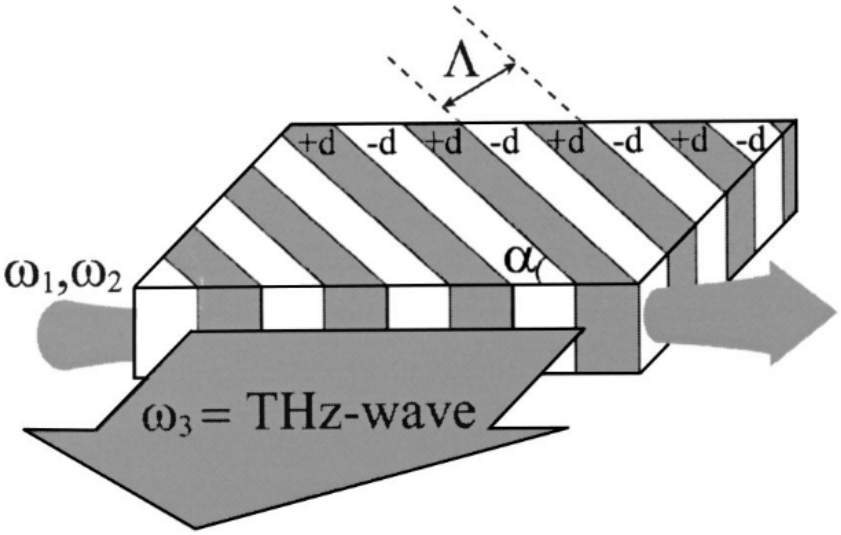

Figure 2.18: The slant stripe geometry of a PPLN device used to create THz using DFG. Figure taken from [111].

to the number of domains. It is important to note that a smaller incident beam includes fewer PPLN periods and so increases the bandwidth, therefore a wider beam is better for narrowband THz generation as well as being less likely to damage the crystal. The smallest bandwidth achieved has been 17 GHz, which was also tunable. Around 8 µW of output was achieved from this effort [108].

More recently, aperiodic PPLN, where the domains decrease in length the further along the beam propagation path travelled, in conjunction with a shadow mask, has been shown to generate THz in nearly single cycle pulses. This was achieved via chirping the delay between pulses to achieve overlap between THz pulses from domains of the same orientation. Diagrams of the crystal are shown in Figure 2.16 [112].

2.4.3 Waveguided Lithium Niobate for Terahertz

Waveguided LN for THz generation is also showing promising signs, albeit being in its infancy. Using a waveguide with its high optical confinement provides advantages such as a reduced area for interacting wavefronts [113].

A LN waveguide for THz has been developed for pulsed operation via a femtosecond laser. It uses Cherenkov radiation and a prism shaped cladding, here a silicon lens, to generate and emit THz radiation. This particular experiment incorporated ridges into the waveguide in order to concentrate the pump beams, increasing power density. It was reported that the output power obtained was one thousand times the amount from a PC antenna, with a range of

0.1 to 7 THz. Conventional Cherenkov radiation generation using a prism has issues of absorption and phase mismatch which were bypassed by using the thin film LN of this technique [114].

Attempts at CW operated THz LN waveguides also exist. An "ultra-narrow-linewidth" CW source tunable within a range of 1 to 7.5 THz has been accomplished using DFG in a silicon prism clad single mode waveguide of MgO doped LN, in a room temperature system. However, the power was low, less than a few microwatts. This waveguide had a small clad channel due to Cherenkov phase matching, where the cladding is prism shaped in order to extract the Cherenkov radiation. It was shown that with a smaller mode diameter, a higher frequency could be gained. The smaller area for wavefronts to interact provide a significantly larger bandwidth for generation than the schemes presented above. It is believed that the waveguide can be improved upon with better heat dissipation and index matched cladding to generate higher output powers [113].

2.4.4 Lithium Niobate Resonant Cavities

A resonant cavity is a space comparable in geometry to the operating frequency of the device. The space is metal clad, and resonates with the operating frequency [115]. SHG in a LN resonant cavity at NIR frequencies has been accomplished using low pump powers in CW, by using an L3 cavity design. An L3 nanocavity is a deliberate defect in a photonic crystal membrane to increase the Q factor, fabricated by creating a lattice of holes and missing three specific holes out of the structure [50].

Pulsed THz generation at around 1.5 THz has been demonstrated with Optical Parametric Oscillation (OPO) by using a resonant cavity to achieve parallel propagation between the pump and emission beams, resulting in better interaction between the beams. This was done by having the cavity equal to the length of a multiple of the pump wavelength, allowing enhancement, and QPM the waves with a grating, with a prism for extraction. The resulting emission had a tunability of 100 GHz, with a 3 GHz bandwidth. However, large losses are shown due to the linear cavity, and from Fresnel losses in the THz extraction [116].

A different pulsed effort utilised a Cherenkov cone in a MgO doped LN crystal to generate radiation between 1.5 and 4 THz. By resonanting the transmission inside a cavity, available pump power is increased. The maximum THz signal is only available briefly due to high thermal drift within the cavity. The maximum THz power seen is more than double that of a single pass crystal. Not all of the power can be seen however, due to the time before the thermal drift causes power degredation being shorter than the bolometer time constant available. It is estimated that inside the crystal almost 14 times the pump power exists, which would produce a higher THz output and broader spectrum. As is common with LN devices for THz, a silicon prism is used to reduce the path length inside the crystal, reducing losses by a factor of five [117].

2.5 Project Motivation

A desire for compact CW sources with narrow linewidths for the 1 to 5 THz region is apparent within the research area. Existing sources in this frequency range suffer from issues such as not working at room temperature, such as with a QCL. A compact room temperature source with a narrow and stable linewidth would be useful for applications such as high resolution THz spectroscopy, and injection locking a QCL to stabilise its emission. Currently photomixing is the best source of narrow linewidth THz at room temperature. However, photomixing has a low power output, especially above 2 THz, resulting in poor efficiencies [118]. Additionally, photomixers do not provide a large operating bandwidth [1, 34].

As an alternative, LN has been shown to generate THz at room temperature [106]. Often used in pulsed generation schemes, advantageous features of the EO crystal such as its large susceptibility coefficient and transparency over a wide frequency spectrum see it used for generating high-field THz pulses. It does have its drawbacks however; very different indices between THz and NIR frequencies, and high losses in the THz range. Techniques such as periodic poling and tilted wavefronts have been used to overcome some of these short-comings but very high peak input powers are typically required. Recent advances in LN technologies, particularly LNOI and micro-fabrication techniques, appear to offer a route to overcome these issues [113]. Waveguides fabricated from LNOI have excellent confinement and strong guiding capabilities due to the high index contrast between LN and insulator material, which is typically SiO_2 [53].

Using a waveguided approach to generating THz, utilising the properties of LN, will fill a niche where compact, tunable, and efficient room temperature CW sources are lacking. This project aims to develop this waveguide, for applications including pulsed and CW THz spectroscopy. The proposed device, introduced at the start Chapter 3, aims to improve on existing LNOI work by attempting to fully phase match the waveguide by using a dielectric layer to perform mode matching. Through this, it aims to succeed in the outline given in Section 1.1.3.

To fulfil the vision of this device, several steps are required, which the ensuing chapters follow. First of all, the device design must be outlined. This entails discussion of what the device is and how it shall work. It extends into simulations of how the device is expected to perform. Following this, the practicality of fabricating such a device must be investigated, analysing optimal materials and deposition techniques. Once a sample has been developed, the performance of it must be experimentally tested. This must happen both at the frequencies of the pump beams and the THz emission.

Chapter 3

Device Design and Simulations

In this chapter the design and simulation of a device to perform efficient optical rectification is introduced. This device utilises a thin film of LN and has the capacity to generate THz in CW operation.

The chapter sections are outlined below:

- Proposal
- Simulation Software
- Waveguide Design
- Projected Performance

3.1 Proposal

To fulfil the ambitions defined at the end of the previous chapter, a device is proposed capable of performing OR in CW operation. To achieve efficient OR, tight confinement is required over a long interaction length. Consequently, the device must adhere to the specifications below:

- The device must be a waveguide.
- The NIR and THz waves must co-propagate.
- The device must be index matched between the frequency regimes.

The design shown in Figure 3.1 has been conceived to fulfil this criteria. A ridge waveguide is proposed, comprised of an LN rib which channels the NIR pump beams and performs DFG to generate the THz, while cladding materials match the index between frequency regimes and provide confinement.

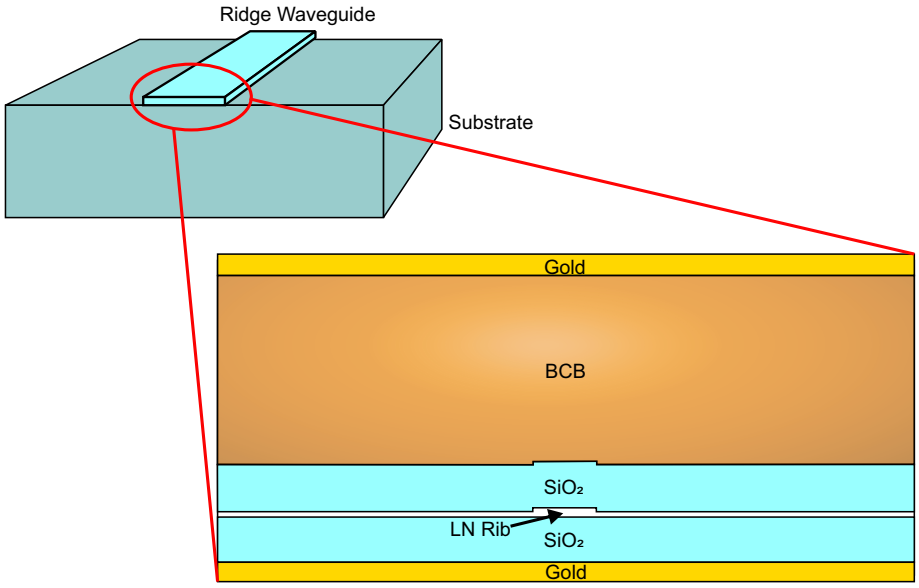

Figure 3.1: A diagram of the proposed waveguide, showing its structure. The top image shows the ridge on the substrate, while below the ridge composition is broken down, detailing the LN rib and its surrounding materials.

The choice of a rib waveguide is to confine the NIR waves for a high intensity, leading to a high emission, while also keeping the loss lower than a ridge waveguide due to less sidewall interaction. The larger ridge waveguide contains the generated THz emission. LN has been chosen due to its high susceptibility coefficient, making it efficient at non-linear generation techniques. The high index mismatch is often an issue with OR via LN, however, the device will attempt to phase match the co-propagating waves via mode matching.

SiO_2 is used to confine the NIR waves to the LN rib, due to having a lower refractive index than LN at NIR frequencies. It has been demonstrated as an effective technique in other LN waveguides [119]. This is shown by the red area in Figure 3.2. Gold cladding is used also, in order to contain the THz waves via the SPP effect. This is shown by the green area in Figure 3.2. It is expected that the THz waves will largely escape the NIR rib into the larger ridge.

A dielectric layer is included in order to help facilitate the mode matching criteria. The material chosen is Benzocyclobutene (BCB), which can be spun on and used to adjust the height of the device, amending the overall effective index. The substance has also been shown to be capable of being used as an index matching material at THz frequencies via doping with Barium Titanate ($BaTiO_3$) particles [120].

The device will have a stable emission frequency. This is because the device will be pumped by highly established NIR lasers, which can have a narrow linewidth within the kilohertz range [30] as well as a low amount of jitter. The

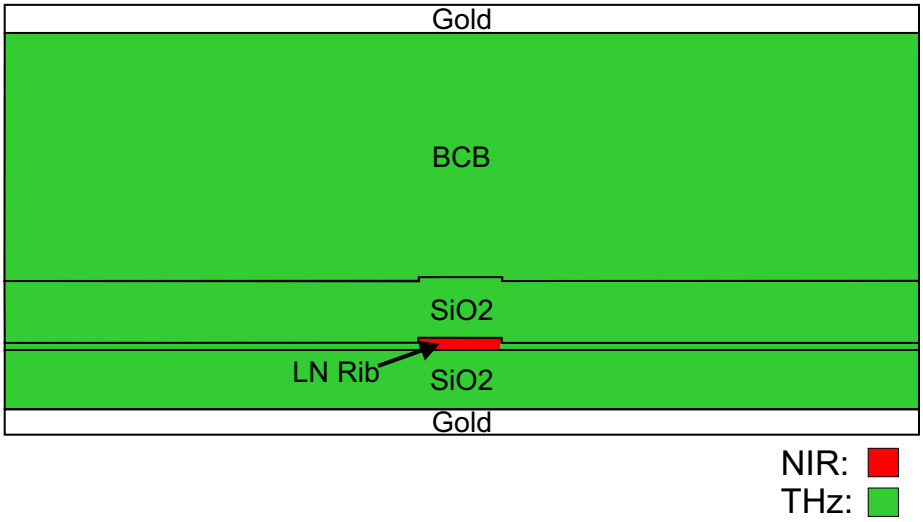

Figure 3.2: A diagram of the cross-section of the proposed device, showing where the NIR waves (red) and THz waves (green) are intended to propagate, through the use of cladding materials for confinement of the waves. It is expected that the THz waves will largely escape from the LN rib into the larger ridge.

quality of the pump beams will dictate the quality of the emission. The THz frequency can be further stabilised via the use of a locking method such as a frequency comb or a phase locked loop. The device shall also be tunable, with the emission frequency determined again by the pump beams. Using a non-linear generation method means that the device shall work at room temperature, but additionally, the capacity of the device to be tunable means that if the mode matching is disrupted by a temperature shift (because refractive index is temperature dependant) then the device can be rematched by tuning the pump beams appropriately. The device shall also provide a continuous THz emission as DFG is a CW technique.

These properties will allow the device to be used as an ultra-stable linewidth source. This would allow it to be used in the future either to perform spectroscopy experiments, or to stabilise a higher power THz emitter, such as a QCL, via injection locking.

3.2 Simulation Software

Two pieces of software were used for estimating the performance of the waveguide and establishing parameters the waveguide must conform to, COMSOL Multiphysics and MATLAB. MATLAB is a coding language, used here to solve differential equations relating to how much power the waveguide will produce over its length. COMSOL is a multiphysics program used here to solve Max-

well's equations in order to calculate mode indices.

COMSOL is a finite element modelling program. With it a user can create an assortment of different geometries using up to three dimensions, pick a physics package, and simulate how their structure will react in the given topic. This is done by selecting materials for different components of the geometry, providing them with the relevant property information, and then constructing a mesh of the geometry; breaking it up into many small pieces and seeing how they interact.

In this work, the physics package used is 'Electromagnetic Waves - Frequency Domain'. A two dimensional structure was developed, as displayed in Figure 3.3, showing a cross section of the waveguide ridge face. The materials involved are allocated to the different areas of the ridge, and detailed in Table 3.1. The complex refractive indices are included in the material parameters, detailing both the real index and the absorption. A more complete list of the refractive indices used in this section can be found in the appendix in Section 8.1.

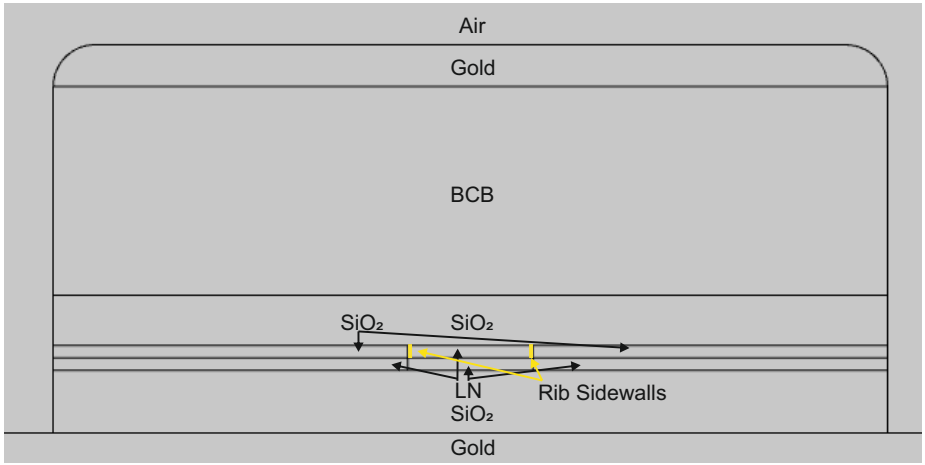

Figure 3.3: A two dimensional geometry of the device design presented in Figure 3.1, constructed in COMSOL. Displayed is a cross-section of the proposed waveguide design. Materials are assigned to the geometric areas. The rib sidewalls are highlighted, which are an area of interest, analysed in detail in Section 3.3.1.1.

The model is then broken up into the mesh; many fine triangles known as finite elements which the software can model as individual segments, shown in Figure 3.4. The mesh is finer around the borders between materials, as the mesh must be made to fit each geometry. COMSOL can have trouble solving the solution around vertices. A way to minimise this issue is to round the corners, increasing the mesh around it, as seen at the top of the ridge in Figure 3.4. The mesh seen in this diagram is deliberately finer in the rib due to being an area of high importance to the waveguide, as that is where the NIR mode is confined.

Finally, the software must be told what to solve. A frequency is input, here

Material Indices at 2 and 193 THz				
Material	2 THz n	2 THz k	193 THz n	193 THz k
BCB	1.42	0.025i	1.55	0i
Gold	296	385i	0.52	10.8i
LN	5.01	0.03i	2.14	0i
SiO_2	2.01	0.001i	1.47	0i

Table 3.1: A table displaying the real refractive index and the loss values at 2 THz of each material in the proposed waveguide [47, 121, 122]. n represents the real part of the refractive index while k represents the imaginary refractive index; the extinction coefficient.

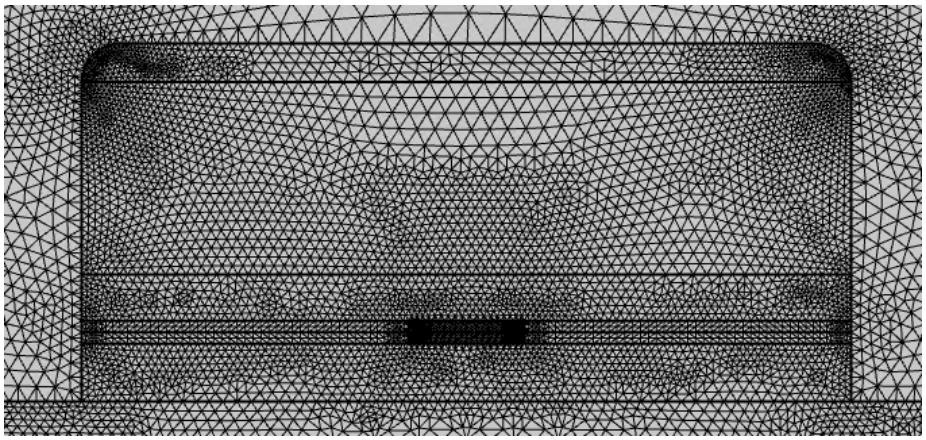

Figure 3.4: A two dimensional geometry of the waveguide with a built mesh. The mesh is built of adjacent triangles, and the area of each triangle is solved separately when computing solutions. A smaller mesh is deliberately used in the LN rib due to being the main area of interest.

either a THz or a NIR frequency, as well as a value of mode index to search around. A mode index of around 2 is chosen for both frequency regimes. This is as the NIR mode will have a high overlap with the LN which has an index close to 2 at NIR frequencies [123].

Various possible options for the exact mode index and shape are shown. The most low-loss and physical solution should be taken, with guidance taken from what is being aimed for, which is a single mode solution in the rib. A solution in the NIR regime is shown in Figure 3.5.

COMSOL provides many different solution options; for example, as well as simply solving for a given frequency, elements of the geometry can be iterated in size and a solution provided for each, allowing for comparisons. This is helpful for testing such items as the best waveguide width. Also, a cross-section of any part of the geometry can be taken to see the value of mode intensity at any point

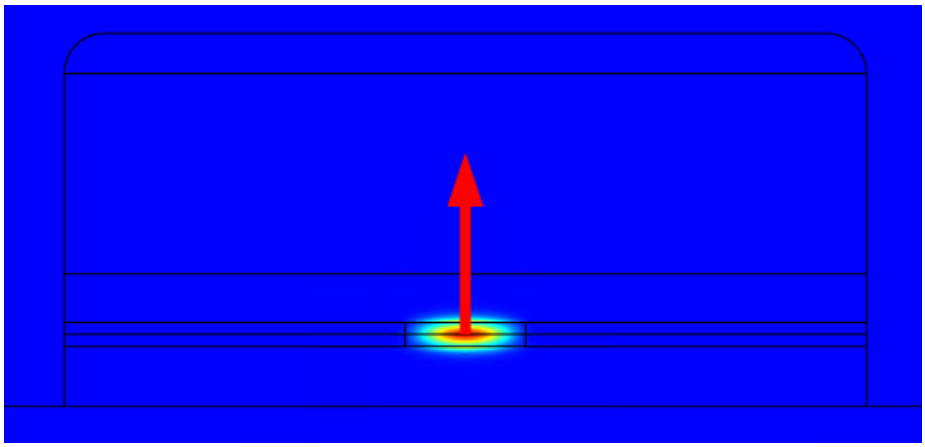

Figure 3.5: A solution to the waveguide mode solved for 193 THz in COMSOL. The brighter area corresponds to where the mode is more intense. The red arrow displays the direction of the electric field; the polarisation.

along the line. Another option is displaying polarisation direction on the model. This can be set from any fixed point on the model, to see how the polarisation changes across it. Any part or all of the model can also be selected so that the electric field in that specific region can be integrated, in order to evaluate the power in that part of the waveguide. This can be used to calculate a figure of merit based on how well confined the power is to the LN rib of the waveguide.

3.3 Waveguide Design

The device has to work at two different frequency regimes. Consequently, it acts as two separate waveguides, one for each regime, and must balance the two to work in tandem. The key elements of the waveguide are defined as the sections below.

- Near Infra-Red Waveguide
- Terahertz Waveguide
- Matching the Waveguides

3.3.1 Near Infra-Red Waveguide

The first frequency regime the waveguide must operate in is the NIR frequencies. The main component of the waveguide is a rib of LN to perform DFG in. This is where the NIR conversion into THz occurs within the waveguide. A single pass LN crystal is used rather than PPLN because the mode index is used for phase matching. This removes the need for the quasi-phase matching of a

PPLN crystal. Working without a PPLN crystal also allows the waveguide to not be restricted to a single frequency of operation but rather enjoy broadband operation. Because the device is designed as a metal-metal waveguide, the THz polarisation must be vertical, and so in turn the NIR polarisation must be vertical to ensure successful concurrent propagation. To accommodate vertical polarisation, Z-cut LN is used. Z-cut LN also supports extraordinary polarised optical modes with a high purity [51]. To consider using a horizontal polarisation within the device using an X-cut wafer, the THz waveguide design would need to change.

The LN is clad in SiO_2 to provide mode confinement in the NIR regime and reduce scattering loss from the rib sidewalls. The high confinement in the rib occurs due to the lower refractive index of the SiO_2, and because the size of the wave in comparison to the rib is large which means the wave interacts with the rib boundaries at shallow angles. Consequently, the total internal reflection condition is reached. Unable to escape the LN crystal, the amount of available source signal to be utilised for THz conversion is maximised.

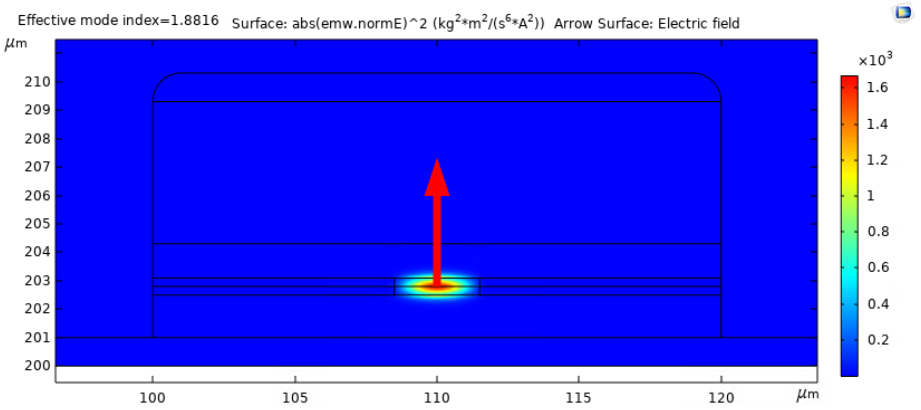

Figure 3.6: A simulation showing the frequency mode at 193 THz. The wave propagates perpendicular to the page, with the field direction parallel to the page, vertically oriented, shown by the red arrow. The colour map shows a higher electric field intensity where the colour is more vivid. The mode is strongly confined to the LN rib.

The highly confined mode is shown in a model in Figure 3.6, and a vertical cross-section of the model along the line x = 110 µm showing mode intensity along the height of the ridge is shown in Figure 3.7. It can be seen that almost all of the field is contained within the LN rib. There are areas either side of the rib in the cross section where the field has escaped to the other side of the LN material boundary.

In the NIR regime solution there is no loss value for the index, meaning it is negligible. This means that all of the source beam is available for pump depletion, ignoring coupling losses. However, this does not take into account

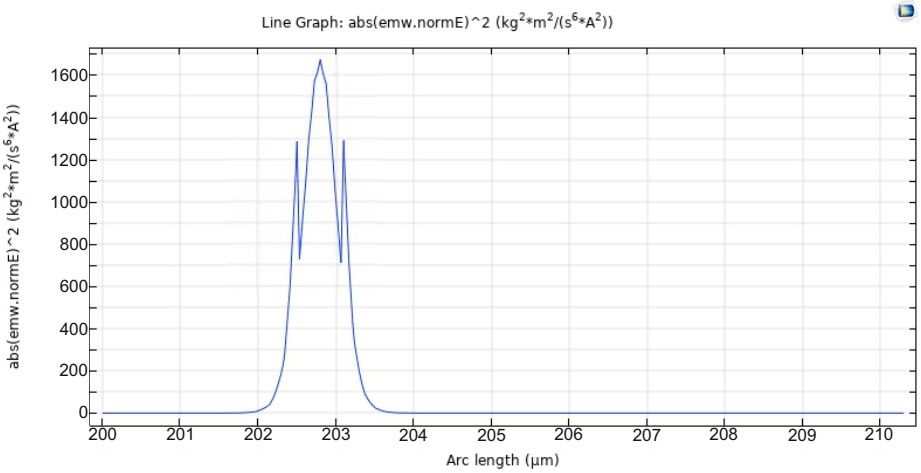

Figure 3.7: A cut-section down the middle of the model shown in Figure 3.6 on the line x=110, displaying the electric field strength through the height of the waveguide. Almost all the mode has been confined in the LN rib. A small amount of signal has escaped into the cladding layers, represented in the plot as the sharp spikes either side of the peak.

scattering effects from the rib sidewalls along the length of the device.

3.3.1.1 Rib Width and Polarisation

An important aspect of the waveguide is the width of the LN rib. The width must be narrow for a high confinement of the NIR mode to ensure single mode operation and a high mode intensity, which is essential for THz conversion. The waveguide rib is designed to be micrometre scale. This allows the confinement needed for high intensity at the trade off of less effective coupling.

A simulation was run on COMSOL, Figure 3.8, to see how altering the rib width changed the device properties. The orange plot of Figure 3.8 details how using a wider rib decreases the difference in index between two NIR frequencies which may be used for DFG. When considering the waveguide, it must be kept in mind that it needs to run in two frequency regimes simultaneously. To avoid destructive interference between the different frequency waves, the mode indices of the two effective waveguides must be matched as best as possible, in order to provide phase matching through the length of the waveguide and gain a high walk off length. However, if ignoring the tunability potential of the waveguide, then the NIR and THz frequencies could be perfectly matched in an ideal waveguide, by adjusting the matching parameters presented in Section 3.3.3. In this scenario, the walk off length of the waveguide is limited by the matching between the NIR waves. Thus, the NIR frequencies must be as closely matched as possible.

It is predicted from similar waveguides in literature that EO wave interaction

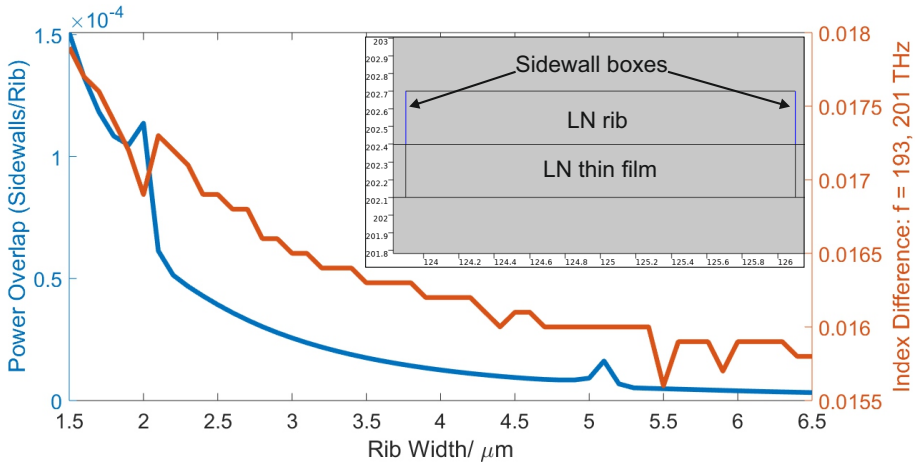

Figure 3.8: A plot of the index mismatch between two NIR frequencies (orange), and how increasing the rib width influences the power in the sidewalls of the rib in comparison to the rib as a whole (blue). The sidewalls are the areas at the sides of the LN rib, analysed by creating 1 nm wide geometries here to check the amounts of power in them. This is seen in the inset in the top ridge corner, where the 1 nm wide boxes are labelled and highlighted in blue. The overlap data was simulated at 193 THz. The spikes in this line are due to difficulties finding a vertically polarised fundamental mode solution in COMSOL at those rib widths. The deviations in the orange plot are due to reaching the highest level of precision available.

with the waveguide sidewalls will be the dominant form of loss in the proposed waveguide [124]. Thin ribs will have increased sidewall interaction compared to wider ribs, meaning a balance must be struck with width on providing high confinement while limiting the sidewall interaction. It is a key fabrication aim to have the rib sidewalls as smooth as possible in order to reduce loss from what interaction there is. The optimum rib width will be determined experimentally because the sidewall scattering loss is fabrication dependent.

The amount of signal interacting with the sidewalls was investigated in Figure 3.8 by creating small boxes in the geometry at the rib sidewalls, which could have the electric field strength in them evaluated. These boxes were 1 nm wide. The power in the sidewalls divided by the total power in the rib provides an evaluation of the proportion of power interacting with the sidewalls. This is seen in the blue plot in Figure 3.8. The average power flow in time through an area is calculated by taking the integral of the area in COMSOL. Doing this for two areas and then dividing one by the other will present the power between them as a proportion.

From both data sets given in Figure 3.8, it is indicated that a wider LN rib is more beneficial. However, this must be weighted against the need for a high mode confinement for efficient NIR conversion into THz. This is exemplified

by COMSOLs struggle to find fundamental mode solutions above a 6.5 µm rib width. Therefore, a rib width of 3 µm appears to be a sensible compromise.

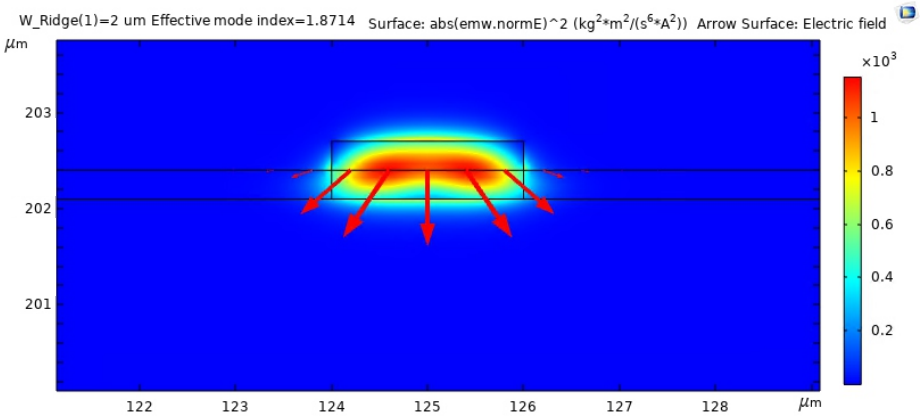

Figure 3.9: A screenshot of the vertically polarised mode profile when the rib width is set at 2.0 µm width. It is noticeably warped in comparison to the circular shape of a fundamental mode, as seen in Figure 3.6. The red arrows show the polarisation direction and magnitude at different points along the x-axis.

There are other rib widths in Figure 3.8 at which COMSOL struggled to find sensible fundamental mode solutions, seen in the blue line of the plot. These occurred at rib widths of 2.0 and 5.1 µm. The 2.0 µm wide rib is shown in Figure 3.9, which portrays a vertically polarised mode but of a different shape to the example given in Figure 3.6. The differing polarisation direction along the width of the rib displays polarisation mixing occurring. This occurs due to a larger influence from the electric field in the x plane, presumably caused by resonance in the system, although it is unknown for sure.

In the simulations, several solutions for the modes were solved. These consisted of solutions containing both vertical and horizontal polarisations. Vertically polarised solutions were deliberately searched for. This is to ensure matching to the proposed THz waveguide, which must be vertically polarised due to the use of a metal-metal structure. It also allows the device to be QCL integration compatible, via injection locking. However, it can be seen in Figure 3.10 that horizontal solutions successfully contain more of the power in the rib that in vertical solutions. This means that horizontal polarisations will produce a higher waveguide transmission at NIR frequencies.

The solutions found at THz frequencies, detailed in the the next section, Section 3.3.2, were found at vertical polarisations. No fundamental horizontal solutions were solved by COMSOL in the THz regime. As both frequency regimes will need to be orientated the same way for DFG to work effectively, vertical polarisation is necessary, despite the poorer performance in the NIR simulations.

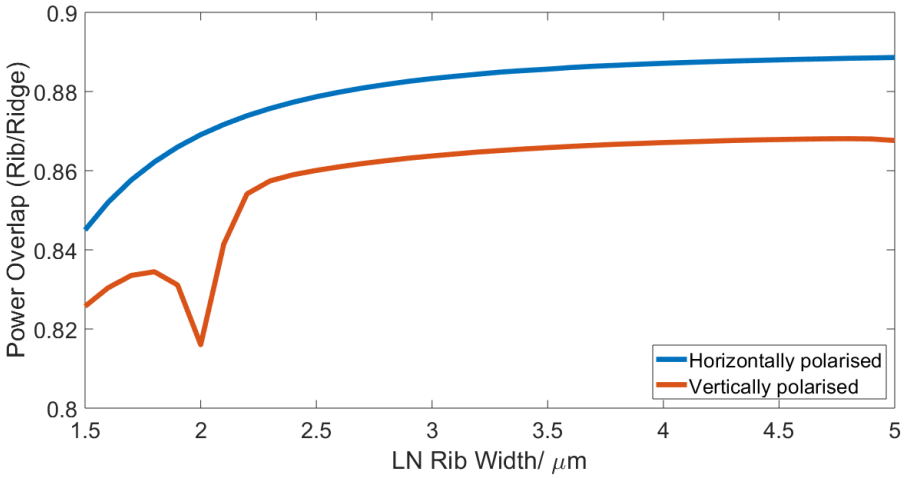

Figure 3.10: A plot of the mode overlap of the rib against the ridge, compared to ridge width, at both horizontal and vertical polarisations. The spike in the vertically polarised plot line is where mode warping is seen, as shown in Figure 3.9. Simulated at 193 THz.

3.3.2 Terahertz Waveguide

A layer of the hydrocarbon BCB is added on top of the SiO_2 clad LN. This is done to engineer the THz frequency waveguide index to the desired value to match the NIR index. Because the index of BCB (1.42 at 2 THz) lies below the index of LN (5.01 at 2 THz) and the target mode index (around 2), it can be used to reduce the mode index to the desired value. BCB is chosen as the material for this purpose because it has a low permittivity and low loss at both NIR and THz frequencies. It can also be spin coated to thicknesses of more than 10 µm and, because it is a photoresist, can be patterned with photolithography [125]. It has a proven record of being used in THz waveguides [126]. BCB additionally comes with the convenience of being easy to dope. By stirring in $BaTiO_3$ nano powder, the refractive index of the BCB can be adjusted, helping with phase matching in the waveguide [120]. Doping for index matching is explored further in Section 3.3.3.1.

The top and bottom of the waveguide is coated in gold. This helps with mode confinement at THz frequencies, as the metal layers create surface plasmon resonances. Having gold cladding both above and below makes this device a double metal, or SPP, waveguide. This is necessary for confinement of the THz wave as its larger wavelength in comparison to the NIR wave means it is not confined into the small LN rib.

Comparing Figure 3.6 and Figure 3.11 shows that the mode is much more confined at NIR frequencies than in the THz regime. This is because the THz mode is confined by the two further away metal layers. At the dielectric metal

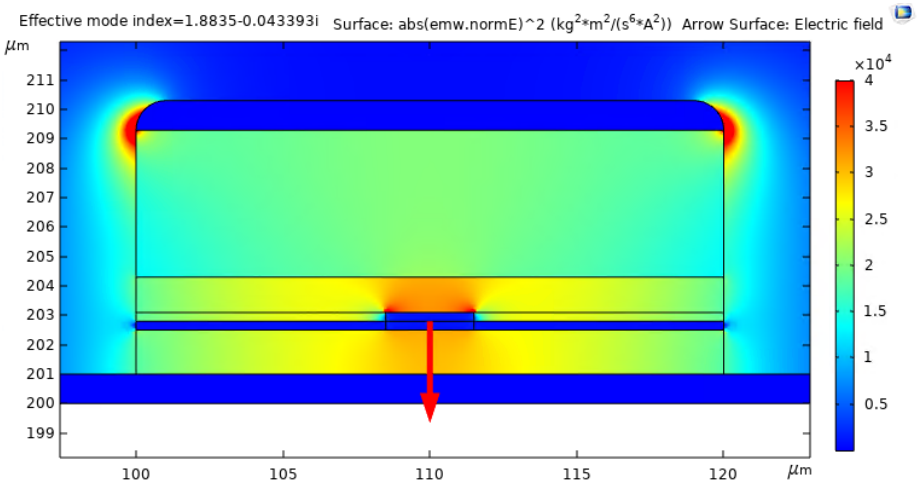

Figure 3.11: A simulation showing the guided mode at 2 THz. The colour map shows a higher intensity where the colour is more vivid. It can be seen that much of the signal has escaped the LN. This lowers the waveguide losses by avoiding the high index material as well as the large phonon modes in this region. The high intensity areas at the top corners and outside of the simulated device are areas which COMSOL has struggled with, and are false. The corners of the simulated device are rounded to limit this effect.

interface, SPPs are caused by the approaching EM waves. The induced charges along the material boundary keep the mode contained [127]. Figure 3.12, a cut-section of Figure 3.11 on the line x=110, highlights that almost all of the THz has escaped from the LN. In the COMSOL solution, the THz frequencies are not shown to be most intense in the LN rib where it is generated because the eigenmode solver does not take into account the gain of the system.

It is worth noting that because this is a waveguide and not a laser, it is less important to have a high mode overlap [113]. The low overlap means that the waveguide is less sensitive to loss, a distinct advantage over any bulk LN method of creating THz due to the high loss values of the EO crystal at these frequencies, especially above 2 THz as this is a region with large phonon modes [47]. An example of this low overlap advantage is the prism clad waveguide discussed in Section 2.4.3, which simply extracted through the prism instead of needing a high mode overlap through the waveguide [113].

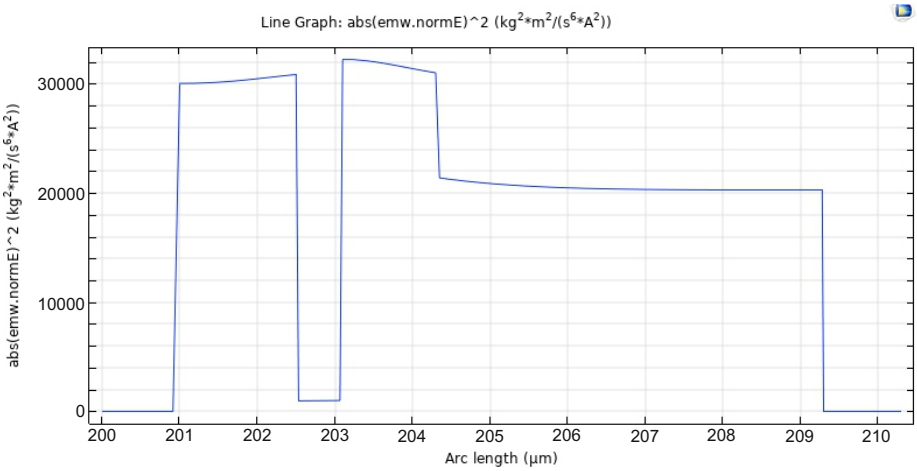

Figure 3.12: A cut-section down the middle of the model shown in Figure 3.11 on the line x=110, displaying the electric field strength through the height of the waveguide. It can be seen that almost all of the field has escaped from the LN layer, with a large dip in field at this point while it is high in the surrounding SiO_2.

3.3.2.1 Ridge Width

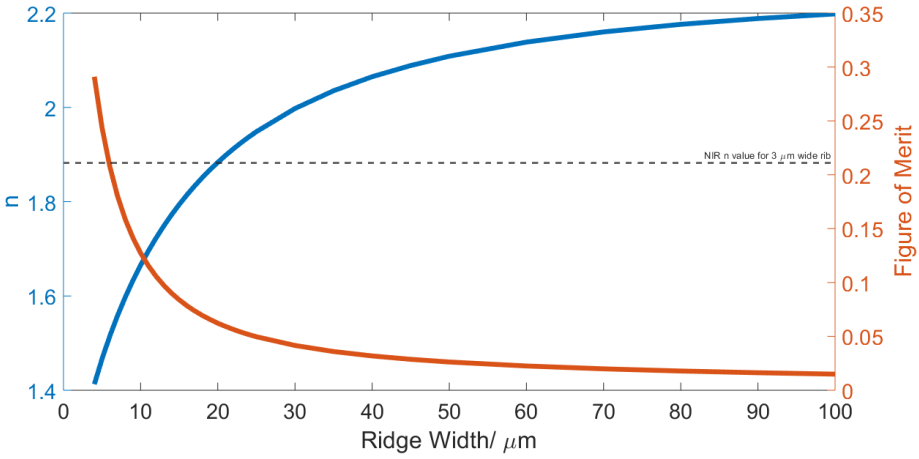

Figure 3.13: A plot showing the effect of ridge width on the waveguide mode index and its Figure of Merit (FOM). The width was changed an equal amount each side of the ridge. The dashed line shows the mode index in the NIR regime when using a 3 µm wide rib. Simulated at 2 THz, with a 5 µm thickness of BCB and 10% doping.

The ridge is the structure containing the guiding rib and cladding materials atop the substrate. Figure 3.13 shows that a wider ridge provides a slightly higher mode index in the THz regime, but also less available power due to lower confinement. The height of the rib is analysed later, in Section 3.3.3.1. Increasing the ridge width causes the index to increase rapidly before levelling off, while the FOM follows the same trend but decreasing instead. The FOM is defined as the proportion of the power confined to the LN rib out of the whole ridge, divided by the extinction coefficient, k, seen in Equation (3.1). The change in property response is much sharper when dealing with thinner ridge widths as the amount of material for the THz mode to escape into is more limited and closer to the LN rib.

$$FOM = \frac{(\frac{P_{\text{rib}}}{P_{\text{ridge}}})}{k} \tag{3.1}$$

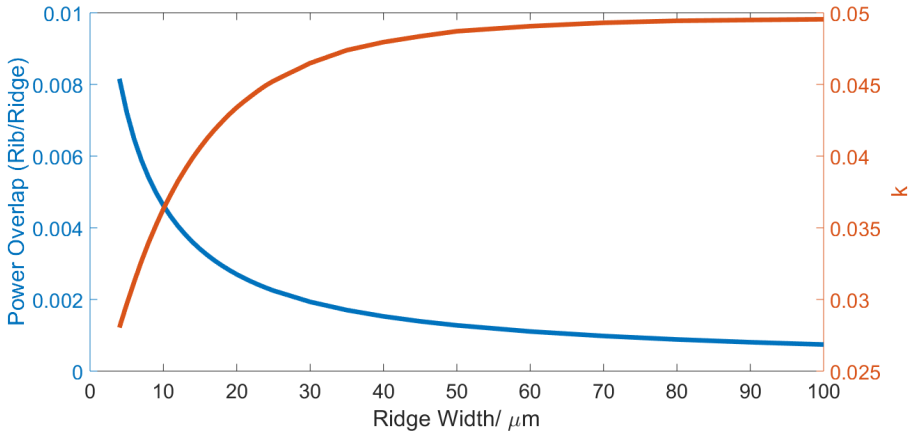

Figure 3.14: A plot portraying the influence of ridge width on the overlap of power between the rib and ridge, and the extinction coefficient k.

The components of the FOM can be broken down into its constituent components, power overlap and k. These are shown in Figure 3.14. It can be seen that as the ridge becomes wider, loss increases as the mode confinement is reduced. This indicates that widening the ridge should only be done if needed to adjust the n value for mode matching waveguides. This is discussed further in Section 3.3.3. Increasing the ridge width increases the value of n. It is important to note that some ridge width is ideal in order to aid in fibre coupling to the waveguide. If the ridge is too thin, or short vertically, it will be extremely difficult to couple into the small area by optical fibre, and much of the signal may be lost if the fibre does not have a sufficiently small spot size.

3.3.3 Matching the Waveguides

Phase matching the NIR and THz regimes through the waveguide is essential for not losing the desired signal due to destructive interference. This is done by equating the effective mode indices of the waveguide at the different frequencies being utilised.

There are two important parts to matching the waveguides; how it is done, and how effective it is. These are detailed below.

- Matching Using BCB
- Walk Off Length

3.3.3.1 Matching Using BCB

Following the work on optimum ridge width, seen in Figure 3.13 above, the other variable of a waveguide cross-section is height. While obtaining a good THz mode confinement is desired, layer thickness plays another crucial role in the waveguide: index matching. By varying the thickness of the BCB layer, the effective index of the NIR and THz waveguides can be equated. This results in a matched waveguide, with no destructive interference along the length of the ridge from the concurrent travelling waves. An analysis on how the n value changes with varying BCB thickness is seen in Figure 3.15.

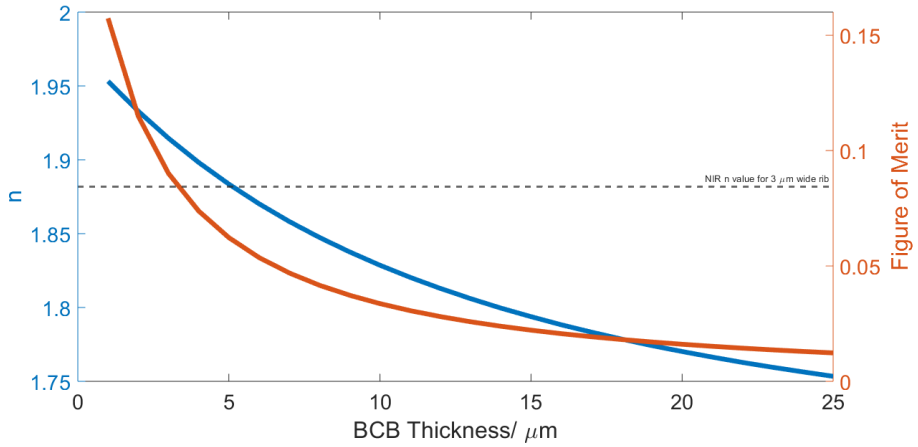

Figure 3.15: A plot displaying how the waveguide index and FOM change with increasing BCB thickness. The dashed line shows the mode index in the NIR regime when using a 3 µm wide rib. Simulated at 2 THz, with a 20 µm ridge width and 10% doping. The rib is 3 µm wide.

The more BCB that exists on top of the rib, the higher the extinction coefficient, and consequently, absorption loss. This is seen in Figure 3.16, and is

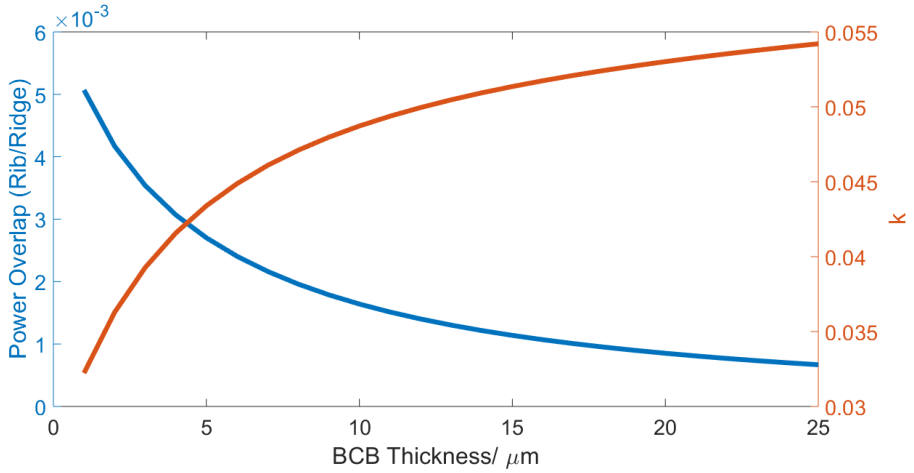

Figure 3.16: A plot portraying the influence of BCB thickness on the overlap of power between the rib and ridge, and the extinction coefficient k.

BCB Refractive Index at Different Dopant Concentrations		
Doping Level (%)	n	k
0	1.65	0i
10	2.3	0.07i
20	2.9	0.09i
30	3.8	0.17i
35	4	0.18i
40	4.1	0.19i

Table 3.2: A table providing the complex refractive index of BCB when doped with varying levels of $BaTiO_3$ powder [120]. Values correct for 0.4 THz.

because the THz mode has more area to escape into, so is less confined. However, the BCB is required to be thick to increase the size of the coupling area.

Around 5 µm of BCB was chosen to be used. This keeps the mode index high, does not degrade the performance by a large amount, and provides a reasonably sized facet to couple into using an optical fibre. A larger BCB surface area will collect more light, increasing the coupling efficiency, and much of that light can be refracted into the higher NIR index LN.

Doping the BCB with $BaTiO_3$ is a possibility for increasing the THz index if required. This allows the n value to change without needing to compromise on the ridge dimensions. The effect of doping BCB on its complex refractive index is seen in Table 3.2. The index of BCB is fairly stable across the THz band. BCB has been shown to be capable of doping up to approximately 50% before particle aggregation [120]. The change to the index of the waveguide is seen in Figure 3.17.

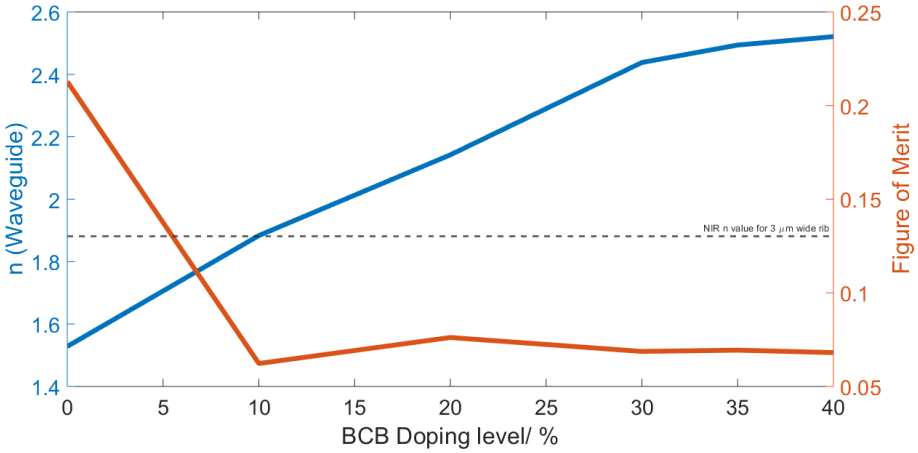

Figure 3.17: A plot showing the effect of doping the BCB with $BaTiO_3$ powder on the refractive index of the waveguide and its figure of merit. The dashed line shows the mode index in the NIR regime when using a 3 µm wide rib. Simulated at 2 THz, with a 20 µm ridge width and 5 µm BCB thickness. The rib is 3 µm wide.

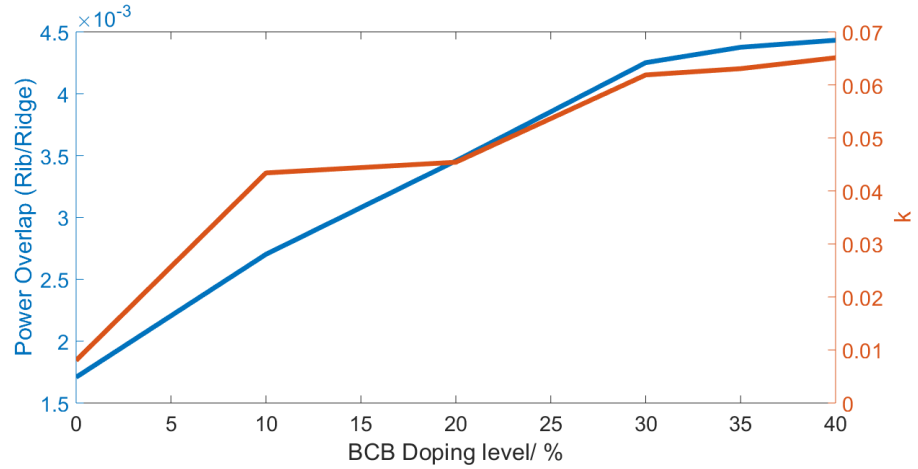

Figure 3.18: A plot portraying the influence of BCB doping on the overlap of power between the rib and ridge, and the extinction coefficient k.

Figure 3.17 shows that the index of the waveguide rapidly increases with doping level. This is because of the increased loss through the BCB, highlighted in Table 3.2. The figure of merit drops with doping, but is fairly level once only 10% doping has been used.Therefore, there is no detriment to performance by increasing the doping further if this allows more preferable ridge height and width parameters. Figure 3.18 breaks the FOM down into power overlap and k.

The power is more confined in the rib with higher doping, but this is also what increases the losses through the waveguide. LN and SiO_2 areas of the device have high losses at THz frequencies, and the waves become more prominent here with doping, however, these materials are needed for the NIR waveguide.

The demonstrated waveguide design has been doped by 10%. Without this doping, it was found that to match the THz waveguide to the NIR regime, the ridge would need to be wider than 100 µm with BCB thickness of only a couple of µm or less. A ridge this wide would have a poor performance, while a layer of BCB so thin would make the ridge difficult to couple to. Spinning a layer of BCB so thin is possible, requiring thinning using mesitylene. Increasing the doping level was also found to increase the index range of the ridge between THz frequencies. This lowers the tuning potential of the waveguide.

3.3.3.2 Walk Off Length

In order to prevent destructive interference between the waves of different frequencies co-propagating through the waveguide, the waveguide must be phase matched. This equates the velocities of the waves, despite their differing frequencies to each other. There are three waves which the waveguide must match between:

- NIR_1 and NIR_2
- NIR_1 and THz
- NIR_2 and THz

Each of these three pairs will have a length in which the waves can co-propagate before destructive interference occurs, determined by how close the phase matching is. The shortest of these three walk off lengths determines the usable device length. A longer device length allows more pump depletion to occur, leading to higher emission powers.

Matching between the waves of NIR_1 and NIR_2 has been discussed in Section 3.3.1.1, with a look at how changing the rib width affects the index range between NIR waves of different frequencies. This was shown in Figure 3.8.

The remaining matching criteria to fulfil is for matching the NIR waves to the THz wave. This can be done by adjusting the ridge in three ways:

- Height
- Width
- Doping

These methods have been evaluated in Section 3.3.2.1 in Figure 3.13, and in Section 3.3.3.1 in Figure 3.15 and Figure 3.17. These matching techniques do not affect the NIR mode index, as the mode in this frequency range is well confined in the rib.

Equation (3.2) [55] calculates the walk off length:

$$l = \frac{c\tau_P}{n_{\mathrm{THz}} - n_{\mathrm{NIR}}} \tag{3.2}$$

In this equation, τ_{P} is for the time period of a pulsed wave, so for a continuous source we can replace τ_{P} with $1/f_{\mathrm{P}}$, where f_{P} is the frequency of the pump wave. Length is represented by l, c is the speed of light and n is mode index at either NIR or THz frequencies. Walk off length is similar to coherence length, shown in Equation (3.3) [55]:

$$l_{\mathrm{c}} = \frac{c}{2v_{\mathrm{THz}}|n_{\mathrm{group}} - n_{\mathrm{THz}}|} \tag{3.3}$$

l_{c} is the coherence length, v_{THz} is the velocity of the THz wave and n_{group} is the group refractive index. This equation indicates the length before the pump is out of phase with the THz emission by $\pi/2$, describing the effective interaction length. The walk off length is used here, as this is the point after which the peak signal will start to drop off due to destructive interference, rather than the point that the system is so far out of phase it stops emitting any signal.

A plot of how closely together the mode indices must be matched for lengths up to 10 mm is given in Figure 3.19.

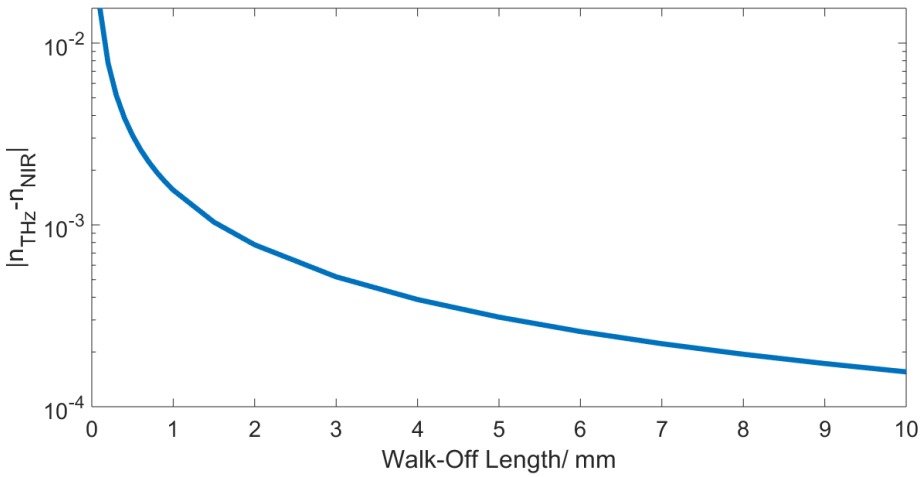

Figure 3.19: A plot detailing how close together the refractive indices must be between co-propagating waves to reach waveguide lengths of up to 10 mm. Calculated for a pump frequency of 193 THz.

Figure 3.19 shows that the matching needed to achieve minimal phase disparity is very close. It is important to note that by fine tuning the geometry into sub-micron levels and beyond, perfect phase matching between a THz and a NIR frequency is achievable. However, fabrication techniques on such small scales are not precise enough for such margins. This explains how realistically, perfectly matching the indices is not feasible, meaning that there is a finite

length to a working waveguide. Additionally, while matching between the THz and one pump beam perfectly may be theoretically manageable, it would not be possible to simultaneously match perfectly to the second pump beam.

Figure 3.20 examines the matching between the two NIR waves. In this plot, NIR_1 is set at 193 and 201 THz, and NIR_2 is swept, providing the x-axis variable. The walk off length between NIR_1 and NIR_2 is given on the y-axis.

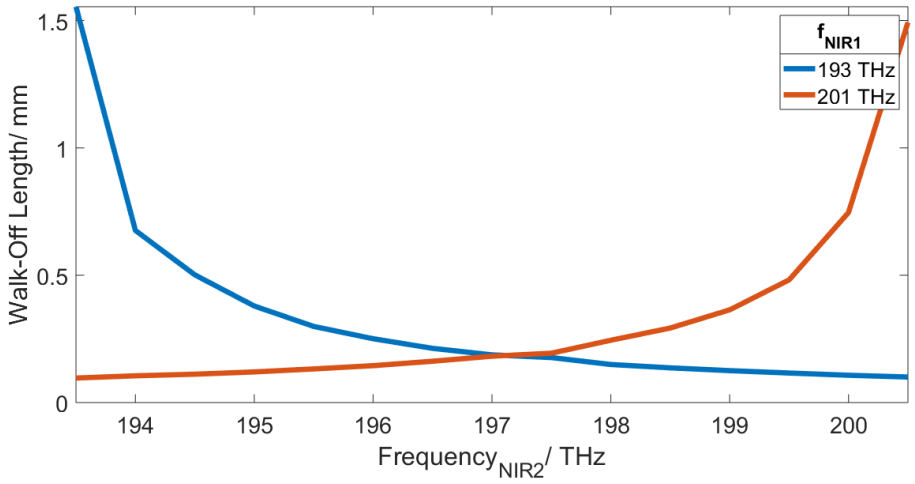

Figure 3.20: A plot of how the walk off length changes with varying NIR frequency. NIR_1 is set at 193 and 201 THz, and NIR_2 is the variable. The rib width for this plot was 3 µm.

The NIR matching is shown to only provide a short length; less than 1 mm when tuning for a frequency difference of as little at 1 THz. This is consistent between the two NIR_1 values used.

The matching of the NIR waves to THz frequencies is given in Figure 3.21. In this graph, each NIR frequency is a plot line between axes of THz frequency and walk off length. The plot aimed to match 2 THz to 194 THz. 194 THz was chosen as it is the centre frequency when using 193 and 195 THz pump beams for 2 THz generation. For this simulation, the scale uses geometry precision of a tenth of a micron. Peaks of data sets are seen due to the resolution limitation.

Figure 3.21 demonstrates that matching a NIR and THz wave together is feasible, over a short THz frequency range. When matching to around 195 THz, it can be seen that for a device length of 1 mm, a THz frequency range of more than 0.15 THz could be tuned between. A 2 mm long device has a THz tuning range of at least 0.1 THz. The shape of the plot shows that the walk-off length decreases with increasing difference in NIR wavelength from the perfect matching frequency. The plot also follows the trend of higher frequency pump beams having a peak walk-off length at a slightly higher THz frequency. This occurs because the index increases with both NIR and THz frequencies.

While the device may be best matched to a single NIR frequency, the THz

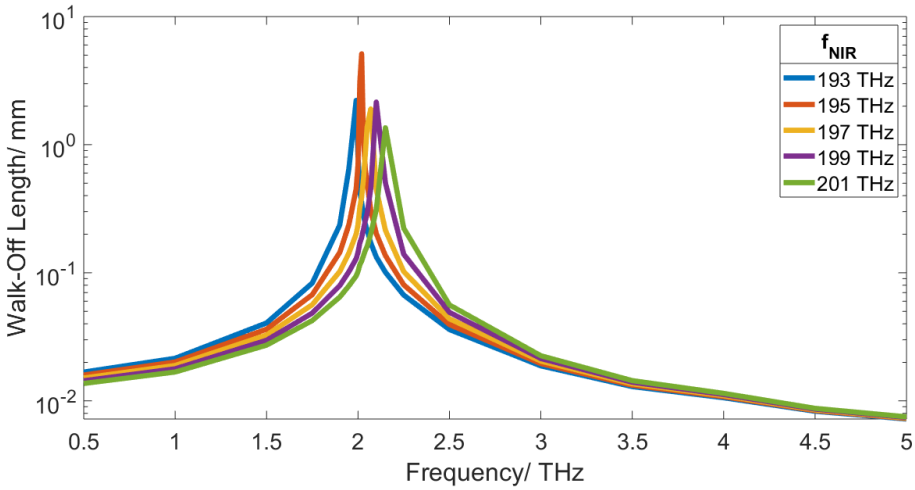

Figure 3.21: A plot detailing the walk off length between NIR and THz frequencies. The mode index of the waveguide at 2 THz was aimed to be matched to the index of the NIR waves at around 194 THz. The rib width was 3 µm. The ridge was 20 µm wide, with 5 µm of BCB thickness, and 10% doping by $BaTiO_3$ powder.

mode must however be matched to two NIR frequency waves. When generating 2 THz using a 195 THz pump beam, a second pump beam at either 193 or 197 THz must be used. The length achievable shown in Figure 3.21 from using a 193 THz pump beam is 2.2 mm. This is a considerable length for THz generation, but it is shorter than the peak value of 5.1 mm shown for matching at 195 THz, and so limits the device length. The THz frequencies at which these peaks occur is slightly offset too, with a 0.03 THz difference. Maximising the walk-off length at one of the NIR frequencies may reduce the length achievable by the second pump frequency used. When looking at generating 2 THz exactly, the lower value of walk off between the 193 and 195 THz pump beams is 0.7 mm.

Because refractive index is temperature dependant, the results displayed in Figure 3.21 would be adjusted in environments that are significantly hotter or colder than room temperature. While this would disrupt the peaks seen in the plot, by simply tuning the pump frequencies to the new refractive index the device can be phase matched again.

The shortest walk off length when aiming for a 2 THz emission is shown in Figure 3.20; the NIR walk off graph. This plot shows that when using 193 and 195 THz for DFG to generate a 2 THz signal, the walk off between them is 0.38 mm. This is shorter than the 2.2 and 5.1 mm peak lengths given between the NIR and THz frequencies, as well as the 0.7 mm length for walk off when considering both pump beams at exactly 2 THz generation. As the waveguide must match all three conditions, the shortest of the three walk off lengths in-

dicates the overall device length, here limited to nearly 0.4 mm. The issue presented is that aside from a minimal change by adjusting the rib width, the device mode index range at NIR frequencies is not easily changed. This then is the limiting factor for the length, and therefore emission power, of the proposed device. There is potential to improve the NIR matching with an adjusted rib design, using periodic width variations [128], or adjusting the shape of the rib.

Figure 3.21 also shows that the tunability of the waveguide is quite low. When using a device matched to 2 THz, tuning instead to use 1 THz lowers the walk off length to 0.02 mm. Tuning to 5 THz restricts the length of the waveguide to the region of micrometers. The poor tunability arises from a large device index change when changing THz frequency. Therefore it is optimal to have separate waveguides for different desired THz emission frequencies, rather than a single tunable device. For example, at 2 THz emission using 193 and 195 THz pump beams, the device can then remain at 0.4 mm length instead of needing to be shortened to accommodate other frequencies.

The THz frequency can be created using different pump frequencies. For example, a 2 THz emission can be made using either 193 and 195 THz or from 199 and 201 THz. When considering the walk off from the centre NIR frequency between the two pumps, the trend is the same as seen in Figure 3.21. By taking the smallest walk off distance from NIR_1 and NIR_2 either side of the centre frequency, it is discovered that the NIR frequency used to match the device is more important to the walk off length than the potential to create the same THz frequency using different pump NIR frequencies. This is because of the amount the refractive index changes with NIR frequency within the device.

A device of 0.4 mm length justifies the requirement of a rib for confinement in the device. The equation for Rayleigh range is as follows [129]:

$$Z = \frac{\pi w^2}{\lambda} \tag{3.4}$$

Where Z is the Rayleigh range and w is the beam waist. Using Equation (3.4), a pump beam at 1550 nm can have a Rayleigh range of around 50 µm when using a beam with a waist of 5 µm. This is already less confinement, and making the waist larger to gain a longer Rayleigh range will result in lower intensities, resulting in lower THz generation efficiencies.

3.4 Projected Performance

The power of the waveguide emission is dependant upon the input intensity for generation, and absorption and scattering for loss, assuming that the length of the ridge is phase matched. Knowing the emitted power means an efficiency can be established for the waveguide.

3.4.1 Absorption

The absorption of light by the medium it traverses is an aspect which plagues the output power. The output wave must gain power via pump depletion at a

greater rate than is lost to absorption in order to obtain a non-zero signal.

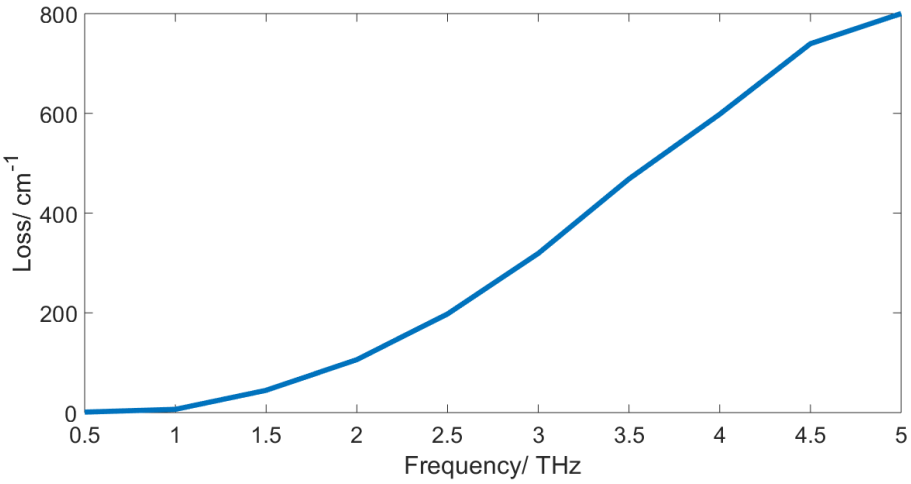

Figure 3.22: Graph showing the loss value of LN in the THz frequency range [1, 47].

A plot of the absorption of LN in the THz regime is displayed in Figure 3.22 [1, 47]. The plot shows higher losses at higher frequencies. This demonstrates that at the higher end of the THz range, where sources such as photomixers drop off in power, the low overlap between the NIR waves in the LN rib and the THz waves that escape into the larger ridge is good as it reduces loss.

In contrast, the absorption of NIR waves in LN has been shown to be negligible [130].

3.4.2 Generated Terahertz Power

The amplitudes of the electric fields of both the input and the output waves follow a slowly varying envelope approximation, due to the change in amplitude over a single wavelength being small.

Starting with the formula shown in Equation (3.5), given in ref. [1], for DFG in a non-linear medium, the amplitude of the THz wave follows:

$$S_{\mathrm{THz}}(L) = \frac{2id_{\mathrm{eff}}\omega_{\mathrm{THz}}}{\epsilon_0 n_{\mathrm{THz}} c} S_1 S_2 \int_0^L e^{i\Delta k z} dz \tag{3.5}$$

where S_{THz} is THz amplitude, L is the length propagated along the THz source, d_{eff} is susceptibility coefficient, ω_{THz} is angular frequency, ε_0 is the permittivity of free space, n_{THz} is the refractive index at THz frequencies (in this instance for extraordinary rays), c is the speed of light, S_1 and S_2 are the amplitudes of the two NIR pump beams, Δk is the momentum mismatch, and z is the direction of propagation [1]. The refractive index value n_{THz} used was the effective index for the whole ridge at THz frequencies, rather than only the

LN, as the THz amplitude will not be confined to the LN rib. The amplitudes of the input waves follow nearly identical equations to this one.

The relationship between amplitude and intensity is:

$$S \propto \sqrt{I} \tag{3.6}$$

where I is intensity. Using the Beer-Lambert law to take into account the loss due to absorption, the amplitude of an otherwise undisturbed wave can be written as:

$$S = S_0 e^{-\alpha L} \tag{3.7}$$

where α is the absorption coefficient. Integrating Equation (3.5), and assuming that I_1 and I_2 are constant due to low pump depletion, output intensity is then, in the ideal case [1]:

$$I_{\text{THz}}(L) = \frac{1}{2}\epsilon_0 c n_{\text{T}} |S_{\text{T}}(L)|^2 = \frac{8 d_{\text{eff}}^2 \omega_{\text{THz}}^2 I_1 I_2}{n_1 n_2 n_{\text{THz}} \epsilon_0 c^3} L^2 \text{sinc}^2(\frac{\Delta k L}{2}) \tag{3.8}$$

While Equation (3.8) provides the intensity of generated signal at a given length through the device, it does not account for pump depletion, or the absorption losses of both the pump and the emission beams. These can be accounted for by differentiating Equation (3.8) with respect to L. By also assuming perfect phase matching, Equation (3.9) and Equation (3.10) are formed.

$$\frac{dI_{\text{THz}}}{dL} = (2ALI_{\text{NIR}}^2) - (I_{\text{THz}}\alpha_{\text{THz}}); \tag{3.9}$$

$$\frac{dI_{\text{NIR}}}{dL} = -(I_{\text{NIR}}\alpha_{\text{NIR}}) - (B\frac{dI_{\text{THz}}}{dL}); \tag{3.10}$$

I_{THz} is the THz intensity, and I_{NIR} is the NIR intensity. A and B represent constants, and are defined below in Equation (3.11) and Equation (3.12).

$$A = \frac{8 d_{\text{eff}}^2 \omega_{\text{THz}}^2}{n_1 n_2 n_{\text{THz}} \epsilon_0 c^3} \tag{3.11}$$

$$B = \frac{2 f_{\text{NIR}}}{f_{\text{THz}}} \tag{3.12}$$

The first term on the right side of Equation (3.9) gives the rate of growth in the THz signal, generated by DFG. The second term accounts for the absorption loss of the generated THz signal.

Equation (3.10) describes the change in NIR intensity; both right hand terms represent losses. The first is the absorption loss. The second term is the pump depletion, indicating that for every THz photon created, two NIR photons are used. It considers what is shown in equation (3.12) - that in the ideal scenario, for every two photons in, there is one photon out.

The terms for THz growth rate and NIR pump depletion are multiplied by length as the values change over the distance through the device. The absorption terms however are constant over the waveguide.

The intensities of the waves given by the differential equations can be used to calculate the power, by using Equation (3.13):

$$P = IA \tag{3.13}$$

where A is area [1, 131]. The area used for the power in the following simulations is a circular approximation. This is because the NIR mode is confined both vertically and horizontally, and less intense radially with distance from the centre of the rib. The intensity is approximated to be constant because while the centre of the mode is more intense, the outer area of the mode will be less intense and create an average intensity across the mode area. The results of using these equations are seen in the following graphs, from Figure 3.23 to Figure 3.29. The values of the variables used in the simulations unless otherwise stated can be seen in Table 3.3.

Simulation Settings	
Variable	Value
Pump power	100 mW
Pump frequency	194 THz
Generated frequency	2 THz
Refractive index	1.8835
Rib cross-sectional area	$\pi(0.3\text{x}10^{-6})^2$ m^2
LN susceptibility	27 pmV^{-1} [22]
Speed of light	$3\text{x}10^8$ ms^{-1} [132]
Permittivity of free space	$8.85\text{x}10^{-12}$ Fm^{-1} [133]
NIR absorption coefficient	0.007 cm^{-1} [53]
THz absorption coefficient	36.35 cm^{-1}

Table 3.3: A table providing the values the variables of the following simulations are set to, unless otherwise stated. The pump power value is set to an easily achievable output for an EDFA. A single pump frequency is used because phase matching is assumed, and a centre frequency of the two pump beams can be used as an approximation of the total NIR power. A single refractive index value is given as phase matching is assumed meaning that the index at both NIR and THz frequencies is equal. The rib area is set as a circle taking into consideration the higher intensity in the centre. Other values are derived from either literature or COMSOL simulations.

The following plots are solved analytically in MATLAB using Equation (3.9) and Equation (3.10). Phase matching is assumed, meaning the plots show how the power functions change by length considering only absorption and pump depletion.

Figure 3.23 depicts the input and output power of the device at a 2 THz emission frequency. The input power decreases over the length of the waveguide

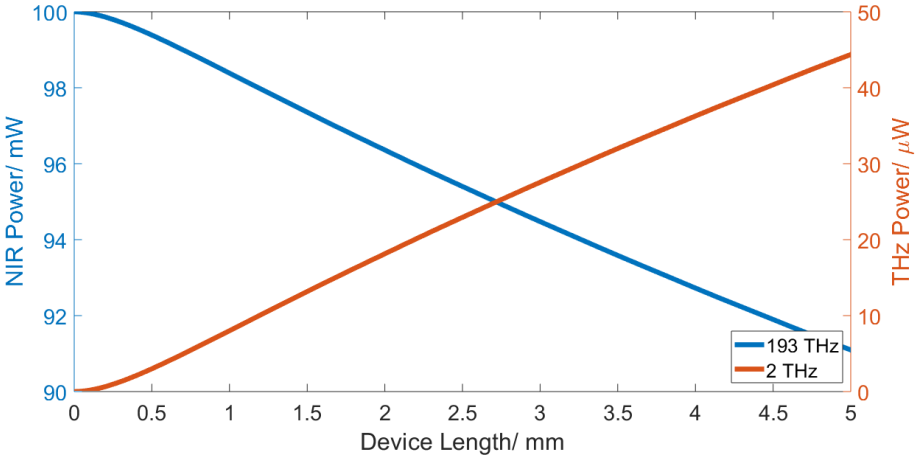

Figure 3.23: Assuming a waveguide with no phase mismatch, meaning no destructive interference from walk-off length, a plot showing how the input pump power and the emitted THz signal varies for a 5 mm long waveguide.

as it is converted. As the pump power depletes, the THz signal increases. Pump depletion is shown to not be reached by the length of the waveguide.

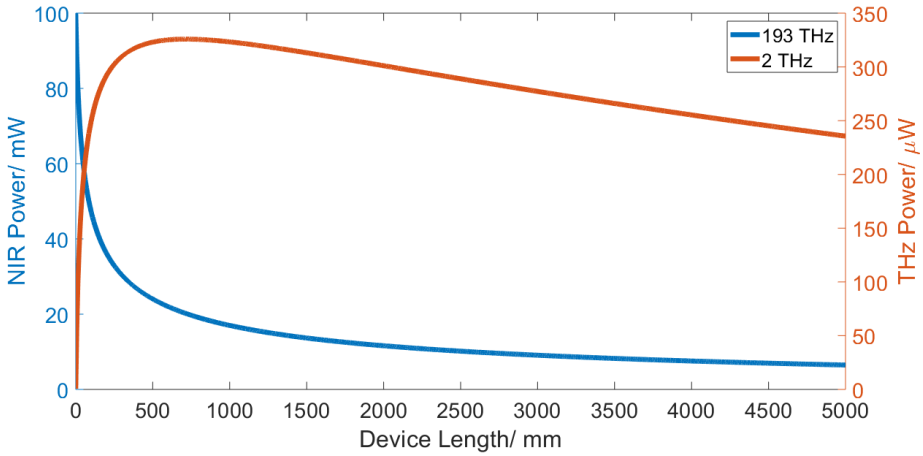

Figure 3.24: Figure 3.23 over a longer waveguide length. The plot depicts an unrealistically long waveguide, showing the theoretical peak of THz generation that could be reached in this process. The plot ignores walk off length, but includes both NIR and THz absorption, as well as pump depletion.

Figure 3.24 shows the same plot as Figure 3.23, over a much longer device length. It demonstrates that there is a peak in THz power available from this process. This peak is difficult to reach; even if phase matching was perfect,

fitting a waveguide of over 50 cm on a semiconductor wafer is impractical. Nevertheless, the plot demonstrates the impact of pump depletion and absorption on the performance of the waveguide. The drop off after the peak is due to the losses overtaking the NIR conversion. As the pump depletes, the efficiency of the process drops due to the decreasing pump intensity.

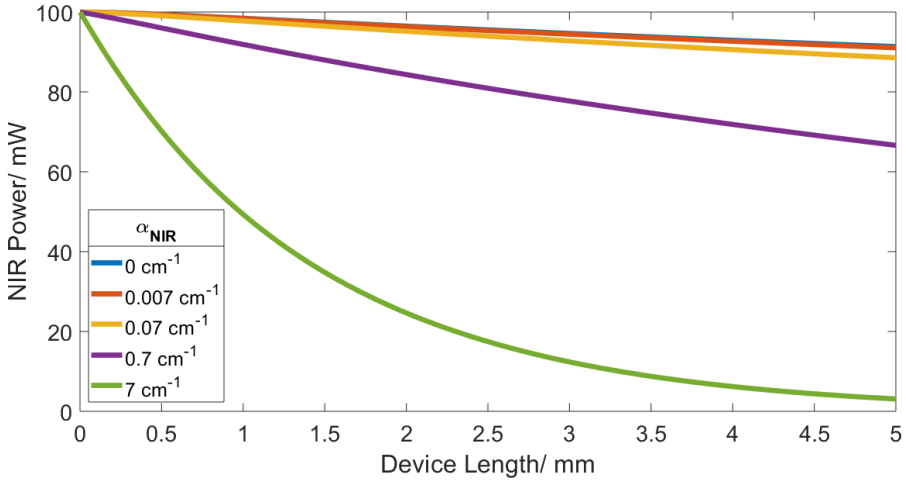

Figure 3.25: A plot displaying how differing absorption values for the NIR regime influence the pump beam depletion. The loss values above 0.007 cm^{-1} are arbitrary and for comparison, up to a 7 cm^{-1} absorption coefficient which translates to around 30 dB/cm loss.

The influence of NIR absorption coefficient on NIR power through the length of the device is shown in Figure 3.25, and its influence on generated THz power through the length of the device is shown in Figure 3.26. High quality waveguides have reported a minimum loss of 0.03 dB/cm, which, using Equation (3.7), is an absorption coefficient α_{NIR} of around 0.007 cm^{-1} [53]. This loss value is shown to be small enough that the plot line in both graphs is almost identical to the zero loss line.

Figure 3.27 shows the THz response for varying pump powers. The response shape is shown to be the same for increasing NIR powers. In Figure 3.28, these response shapes are normalised, and it can be seen that in reality a higher pump power reaches the maximum THz power faster. This makes sense, as a higher intensity has a higher efficiency for frequency conversion via DFG.

These simulations forecast an emission power in the range of tens of microwatts. To generate, for example, 10 µW of THz power using a 5 mm long device, α_{NIR} could be up to 1.75 cm^{-1}, far higher than the 0.007 cm^{-1} demonstrated in similar style high quality waveguides [53]. In this scenario, with the 5 mm length and high α_{NIR}, the losses have started to overtake the emission gain, so a shorter waveguide would provide even more power. Using the low α_{NIR} from other work, a 5 mm long device operating at 2 THz could create

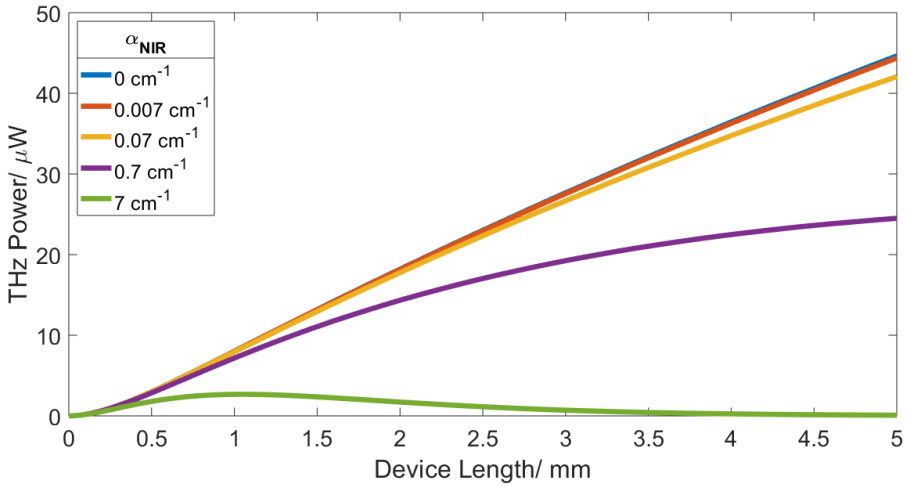

Figure 3.26: A plot displaying how differing absorption values for the NIR regime influence the peak value of THz emission.

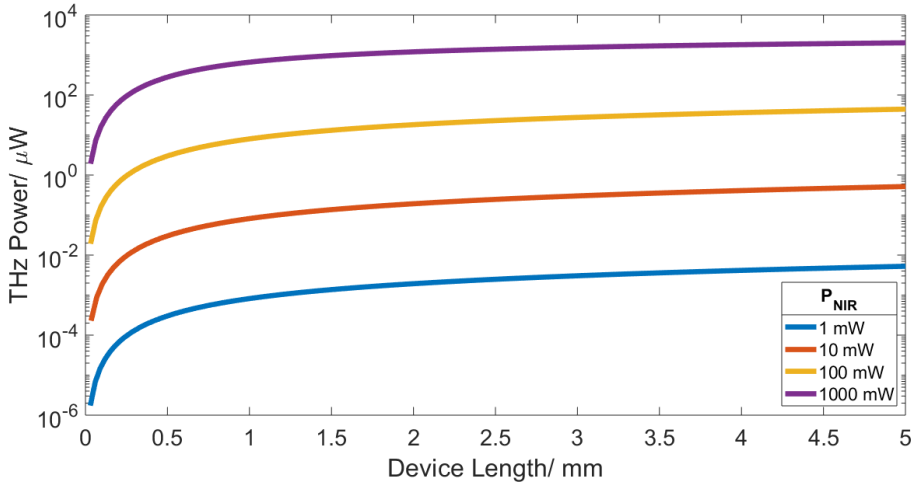

Figure 3.27: This graph shows the output response shape for differing pump powers.

approximately 44 µW of THz power. To remain with a generation of more than 10 µW at 5 mm length using the low α_{NIR}, α_{THz} could afford to increase from its simulated value of 36.35 cm^{-1} to approximately 190 cm^{-1}. Repeating this series of measurements for a 2 mm long device, α_{NIR} could be up to around 1.75 cm^{-1} to keep the power at 10 µW or higher (this time before peak emission), using the low α_{NIR} means 18 µW of power can be generated, and an α_{THz} of 72.5 cm^{-1} or better will keep the THz power above 10 µW.

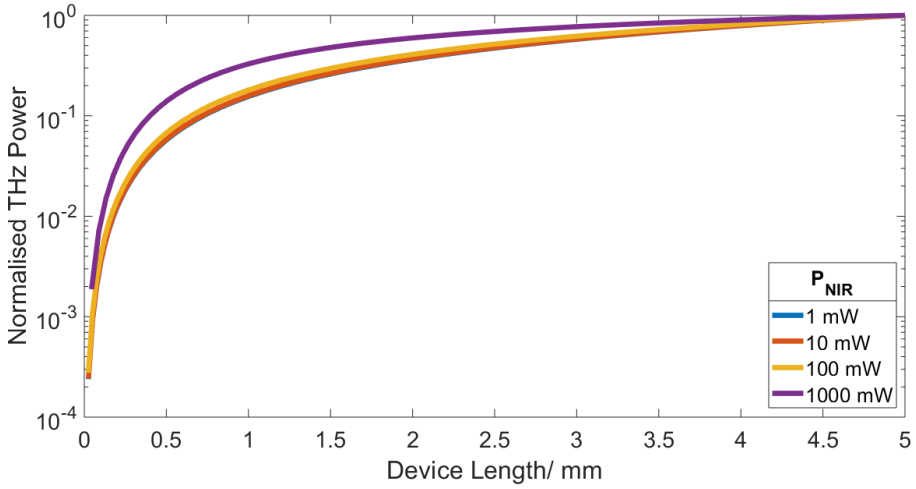

Figure 3.28: This graph shows the data from Figure 3.27 normalised. It can be seen that higher pump powers tend towards their maximum value faster. This proves how higher pump intensity leads to a more efficient THz generation.

This device will then meet the aim set in Chapter 1 of providing a THz output in the range of microwatts within the frequency region of 1-5 THz. While tens of microwatts may not be a comparable power to, for example, a QCL [134], it is enough to perform THz spectroscopy, or injection lock the example higher power QCL. The device is also superior in generatable THz power to a photomixer, which is a comparable room temperature CW THz generation source. Current photomixer technology is only capable of less than 1 µW at frequencies of 2 THz or higher [32].

3.4.3 Efficiency

The efficiency of the waveguide is low. In an ideal system, every NIR photon pair creates a single THz photon; so two photons in for one photon out. This has already limited the maximum photon efficiency for this technique to 50%. In a non-ideal system, absorption issues also arise. To achieve THz emission out of the waveguide in the µW power region then tens of mW must be input from the pump beam. Consequently, to get a reasonable power out, the system must be run at powers close to the damage threshold of the waveguide.

The Manley-Rowe relation is maintained within the waveguide; more power in provides more power out [135]. This follows what can be shown using a variation of the Planck-Einstein equation:

$$E_{\text{eff}} = \frac{hf_{\text{THz}}}{hf_{\text{NIR1}} + hf_{\text{NIR2}}} \tag{3.14}$$

In Equation (3.14), the Planck's constants all cancel, leaving only frequency

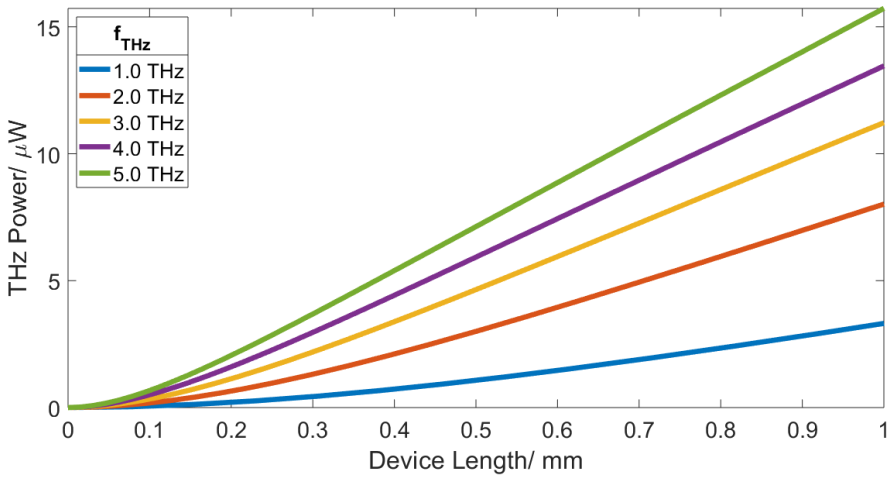

Figure 3.29: The graph shows that more THz is emitted when generating higher frequencies from the same source power. This agrees with the Manley-Rowe relations. The NIR frequencies, refracted index values and THz absorption coefficients were adjusted for each THz frequency. These values can be found in the appendix in Table 8.3. Plotted with a varying pump frequency to simulate scanning NIR_2 to adjust emission frequency.

elements. The THz frequency component is the difference between the two NIR frequencies, therefore the larger the spacing between the NIR photon pair, the larger the numerator becomes. This leads to higher efficiencies for larger emission frequencies, as shown in Figure 3.29. Using two lower frequency input beams increases the efficiency through the same method. This stands in stark contrast to other room temperature THz sources such as photomixers, which have a sharp power drop off above 2 THz. The data shows that the device will operate within the 0.5 to 5 THz range, and there is no implication that it will not work beyond that to higher frequencies. The device will not be sensitive to the higher LN absorption loss at the higher frequencies because of the low overlap.

It can be also be seen from Figure 3.29 that aiming for a 2 THz emission with a device length of 0.4 mm, which is realistic based upon the shortest walk off length as calculated in Section 3.3.3.2, will provide an emission power of just over 2 µW. If the NIR matching is overcome by altering the rib with periodic width variations or similar, a 0.7 mm long device, as dictated by the walk off seen by a centre NIR frequency of 194 THz to 2 THz matching, will provide around 5 µW of THz power. If instead matching to a 5 THz emission, the output power will increase to over 10 µW according to Figure 3.29.

There is potential for even greater amounts of power with better matching, but this is already strides ahead of the power output of a photomixer, which is limited to a few nanowatts in the THz region [32].

The list of aims given in Chapter 1 is as follows:

- Be tunable within a range of 1 to 5 THz
- Provide powers of at least a few microwatts within this frequency range
- Provide a low linewidth
- Operate at room temperature
- Provide a CW emission

Revising this list, Figure 3.29 demonstrates the accomplishment of both the first two points under the conditions of the last two points. Given that the middle criteria of a low linewidth can be accomplished simply by using highly established telecommunications frequencies, this proposed device covers all the desired targets of a THz generation source operating at room temperature in the THz gap.

Chapter 4

Fabrication

In this chapter, the device fabrication developed in the University of Leeds (UoL) cleanroom is discussed. At the start of this project there were no established procedures in the UoL cleanroom for LN processing so much of the process was developed for this project.

The chapter sections are outlined below:

- Review of Fabrication Techniques
- Fabrication of Lithium Niobate Ribs
- Waveguide Facets
- Benzocyclobutane Processing
- Fabrication Summary

4.1 Review of Fabrication Techniques

In this section the fabrication techniques to be used for each step of the process are reviewed. The key steps are:

- Definition of a Rib of Lithium Niobate
- Deposition of a Near Infra-Red Cladding Layer
- Deposition of a Terahertz Index Matching Layer
- Deposition of a Terahertz Cladding Layer

The LN must be waveguided, in addition to clad in SiO_2, for the purpose of confining the NIR pump beams to ensure high intensity and therefore high conversion efficiency, as established in Section 3.4.2. A rib over a ridge of LN is sought in order to reduce the sidewall interaction, discussed next in Section 4.1.1,

while maintaining the lateral confinement [83]. Gold cladding is also used above and below in order to confine the generated THz waves via SPP interactions, shown in Section 2.3.3. This allows the THz to be waveguided to the end of the device, and emitted as a point source, rather than requiring the use of an extraction prism which would result in a beamshape less useful than from a point source. Before the top gold layer goes on, BCB must be deposited in a specific thickness in order to provide the mode matching between the different frequency waves through the device, as discussed in Section 3.3.3.

4.1.1 Definition of a Rib in Lithium Niobate

Etching LN waveguides is challenging [124] because it is difficult to obtain smooth sidewalls [74]. Roughness in the sidewalls results in scattering, leading to high losses. The impact of roughness can take a waveguide from less than 1 $dBcm^{-1}$ to more than 17 $dBcm^{-1}$ [74]. A range of methods for etching LN waveguides have been published, some of these have been summarised in Table 4.1. Many methods involve using a mask; a different material on top of the LN protecting the areas which are not to be removed, leaving behind a three dimensional structure.

One form of LN rib fabrication is wet etching. This involves using chemical solutions to react with the LN layer, reducing the thickness. One such solution is a Hydrofluoric acid (HF) and Nitric acid (HNO_3) mixture, used in conjunction with a chromium mask. Wet etching has an issue with leaving behind rough surfaces, but mixing ethanol into the aforementioned solution has been shown to reduce this roughness, while also reducing the etch rate. Another key issue with wet etching is that the etchant undercuts the mask, although this has been shown to be reduced by annealing [136]. Another experiment used HF acid in combination with implanting copper ions into the LN to achieve a high aspect ratio [137].

Various methods of dry etching LN exist, with varying levels of quality. The simplest is perhaps mechanically dicing a ridge, using a wafer saw. This has a high material removal rate, although requires high precision equipment. This technique has been shown to produce a high quality ridge when successfully performing ductile dicing [72]. Another advantage is that the sidewalls are much closer to being vertical than through other methods, with one paper quoting an angle of 88° [138]. It is restricted, however, to only fabricating ribs consisting of straight lines, and has been quoted as not leaving sidewalls as smooth as other techniques such as Reactive Ion Etch (RIE) [137]. An attempt at fabricating ridges using this method is detailed in Section 4.2.4.

Ultrafast laser machining has been shown as another good method of fabricating waveguides with quick process times, but suffers from extremely poor surface qualities in comparison to other dry etching methods [139].

Plasma etching using fluorine as a reactive gas, in such compounds as SF_6 or a CHF_3 and argon mixture [140], is another method of fabricating LN ribs. However, this deposits a lithium fluoride compound, which is even more difficult to remove than LN [74], while having a low etch rate and sidewalls far from being

vertical [140]. Performing proton exchange on the LN will partially mitigate the redeposition, while changing from parallel plate RIE to Inductively Coupled Plasma Reactive Ion Etching (ICP-RIE) will help straighten the sidewall angle [140].

Another dry etching method is ion milling, which involves bombarding the LN surface using argon ions. Variation of beam voltages and sidewall angles has given the ability to produce an etch with comparatively smooth sidewalls [141].

Based on the information shown in Table 4.1, dry etching is the best option, carried out by ion milling. The UoL cleanroom possesses a Scia Mill 150 ion beam etcher by Scia Systems, which features:

- A 2.45 GHz circular ion beam microwave plasma source (via electron cyclotron resonance)
- 200 to 2000 eV ion energy
- The capability of physical, reactive, and chemically assisted ion beam etches
- Substrate rotation from 1 to 20 rpm
- Substrate tilt from 0° to 165° in 0.1° steps
- Stage backside cooling

A diagram of the milling chamber is shown in Figure 4.1.

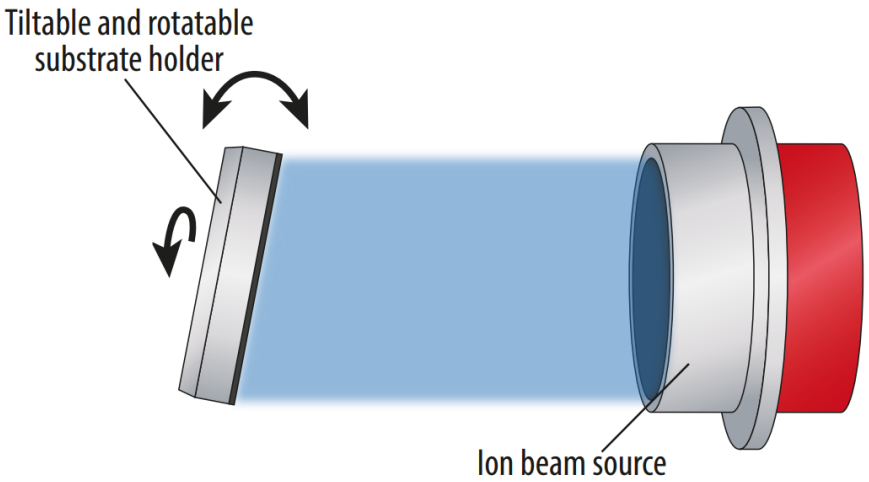

Figure 4.1: A diagram of the the chamber in the miller, showing the tiltable and rotatable stage. Diagram taken from the Scia website [145].

Thin film LN Waveguide Fabrication Comparison			
Fabrication Method	Propagation Loss (dB/cm)	Waveguide Width (µm)	Source
Argon Ion (Ar^+) Etched Rib	17.4	4	[70]
Ti-Indiffused Ridge	0.5 (TE), 0.8 (TM)	6	[138]
Tantalum Pentoxide (Ta_2O_5) rib on LN thin film	5	1	[80]
Strip Loaded Rib	5.8 (TE), 14 (TM)	6	[142]
Wet Etched Ridge	7 (TE), 6 (TM)	1	[143]
Argon plasma ICP-RIE ridge with Wet Etch Re-deposition Removal	5	5	[124]
Diamond Blade Diced Ridge by Wafer Saw	1.2 (TE), 2.8 (TM)	2.1	[144]
Ar^+ Milled Waveguide with Clustered Ion Beam Smoothing	0.33 (TE), 2.8 (TM)	5	[74]
Ar^+ Milled Waveguide with Clustered Ion Beam Smoothing	0.268 (TE), 1.3 (TM)	7	[74]

Table 4.1: A table showing different methods of generating LN ridges, along with the degree of propagation loss. TE and Transverse Magnetic (TM) polarisation data both given if available. Table taken and edited from [74].

An issue faced in similar waveguides produced from ion milling is sidewall angle, which tends to be sloped due to mask shadowing. The proposed waveguide is designed for single mode operation, and the sidewall angle is less of a problem when working with single mode waveguides than multimode, as higher order fields collect more at sidewalls than the fundamental mode [74]. Poor sidewall angle is also partially caused by redeposition, another key milling issue. This is a key factor leading to a high sidewall roughness, which increases waveguide loss. It can be minimised by utilising the rotation of the milling stage to etch with uniformity. Of particular interest is the research which acknowledges the redeposition caused by the process. In one paper, an extra milling step is added where the ion miller is used at an angle much further from perpendicular to the sample surface for a short time at the end of the etch in order to target and smooth the sidewall [74]. This technique has also been employed in other works [141]. By using tools such as the Scanning Electron Microscope (SEM), the effectiveness of milling trials can be viewed and evaluated to determine the optimal settings.

Particular care was taken when looking at the temperature of each etching method. Because LN is both piezoelectric and pyroelectric, it can become charged when heated rapidly, causing Electrostatic Damage (ESD) to the surface. Indeed, audible crackling sounds and macroscopic damage were made during processing trials. This was countered by placing the sample on a glass slide when using a hotplate, causing a gradual temperature change to the LN sample over time when heating and cooling. Ideally, this slide is gold coated to help dissipate the charge. While using a glass slide reduced the risk of ESD, it was not mitigated against completely.

In order to pattern the waveguide, so that a rib is left when milling the LN, a mask must be created. The low feature size of the mask is vital in creating smooth ribs. Lithography with a contact aligner was the first choice for the rib processing. The contact of the mask with the sample means that the mask quality should be very high, due to the limited space for Fresnel diffraction of the Ultra Violet (UV) source beam. Consequently a smaller feature size is offered than with a maskless aligner. Two mask aligners in the UoL cleanroom were used, an EVG610 by EVG, and an MJB-3 UV400 IR UV by Karl Suss. An alternative to contact alignment is Electron Beam (E-Beam) lithography. E-Beam lithography is ideal due to the small feature size and low line edge roughness capable from this instrument. A JBX-6300FS by Joel is in the UoL cleanroom, capable of a 0.125 nm minimum step size.

If the surface roughness of the fabricated ribs was still too high, one option was to make the rib wider. This reduces interaction with the sidewalls and provides a higher Q factor [119]. However, a wider ridge also results in the mode being less confined, which hinders device performance, as demonstrated in the simulations in Section 3.3.2.1.

4.1.2 Deposition of a Near Infra-Red Cladding Layer

The cladding layer above the LN thin film should be low loss for NIR and provide a lower index than the LN. SiO_2 is ideal since this is already used below the LN film in the wafer obtained for this work, detailed in Section 4.2.1. SiO_2 also has the potential for a rib to be defined in it via HF etch if desired. Another key artefact of using SiO_2 is the oxide component. The saline in the BCB layer bonds well with oxygen.

There are many ways of depositing an oxide surface. These include:

- Plasma Enhanced Chemical Vapour Deposition (PECVD)
- Sputtering
- Spin on glass
- Flowable Oxide (FOx)
- Atomic Layer Deposition (ALD)
- E-beam evaporation
- Thermal evaporation

Many of these methods were ruled out from being appropriate for this project, for reasons such as a high temperature profile, which will cause issues with the LN pyroelectric properties, or creating a surface profile undesirable for the device design. This rules out the evaporation techniques, as well as the spin on glass, which requires thermal treatment after the material is spin coated for Silicon (Si) diffusion and for oxidation. Ion sputtering has a chance of substrate damage due to high pressure and ion bombardment, which is not ideal due to the thin film surface structures of the LN [146], while radio frequency sputtering is known to cause thermal damage [147].

The main options considered were PECVD and ALD. These provide comparatively low temperature depositions [119, 148] and can be performed in the UoL cleanroom. PECVD was attempted first. Then, if the results were not good enough due to a non-conformal layer, ALD stood as an alternative. However, ALD is not well suited to layers thicker than tens of nanometres, with low deposition rates [149]. FOx was a good candidate, demonstrated in other work [119], but was not an established technique in the UoL cleanroom.

4.1.3 Deposition of a Terahertz Index Matching Layer

A low loss dielectric material is required for matching the THz mode index to the NIR mode index. BCB has been chosen for this role. BCB is a hydrocarbon, with chemical formula C_8H_8. There are both photosensitive and non-photosensitive forms of it. It can be spun on, at different speeds for different thicknesses, and then requires baking to drive out the solvent. A spin curve

is provided in Section 4.4.1. It is recommended to use an adhesion promoter, AP3000, before depositing a layer [150].

BCB can be mixed with mesitylene, a benzene derivative, to thin the liquid for thinner spun layers. The layer should be cured in a vacuum oven, and other UoL work has shown that curing BCB improves its THz transparency [151]. Multiple layers of BCB can be spun on top each other for a thicker overall layer. When doing so, lower layers should be subjected to a partial, or 'soft', cure to improve layer adhesion.

BCB is a dielectric which has been used in many other LN waveguides, for purposes such as being a lower index layer [144], or a bonding layer [70]. It has previously been used in THz applications due to its low loss in the region [152], and has also been established as a suitable material for index matching at THz frequencies [120].

An alternative to BCB is polystyrene, which has been shown to be a low index material at THz frequencies with low transmission losses [153]. However, the stresses induced in spun polystyrene lead to poor homogeneity [154, 155].

4.1.4 Deposition of a Terahertz Cladding Layer

Gold is used to clad the THz because the THz waveguide is based on the SPP effect. It has been used in many devices for this purpose previously [3, 89].

Gold deposition can be easily performed in various ways, such as evaporation and sputtering. However, deposition on to BCB is more difficult. Gold evaporation onto BCB has been successfully demonstrated before at UoL by using an in situ argon plasma etch to improve adhesion [152].

4.2 Fabrication of Lithium Niobate Ribs

The fabrication of ribs of LN is detailed in this section. First, the wafer used is described, before detailing the efforts of the rib fabrication itself. Further trials are then described following the initial rib batch, with the aim of refining the process. Finally, precision cutting a rib is also looked at.

The process steps for milling a rib are outlined in Figure 4.2.

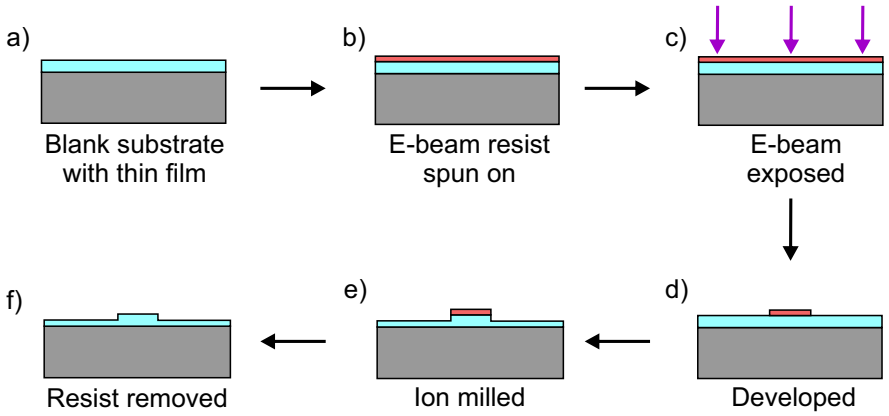

Figure 4.2: The steps of fabricating a rib in thin film LN using an ion milling procedure.

4.2.1 Lithium Niobate Wafer

The waveguides were fabricated on a wafer bought from NanoLN. This wafer is henceforth referred to as 'Wafer 1'. The wafer specifications and layers are detailed below:

- 0010 LN thin film wafer
- 3 inch diameter
- Z-cut

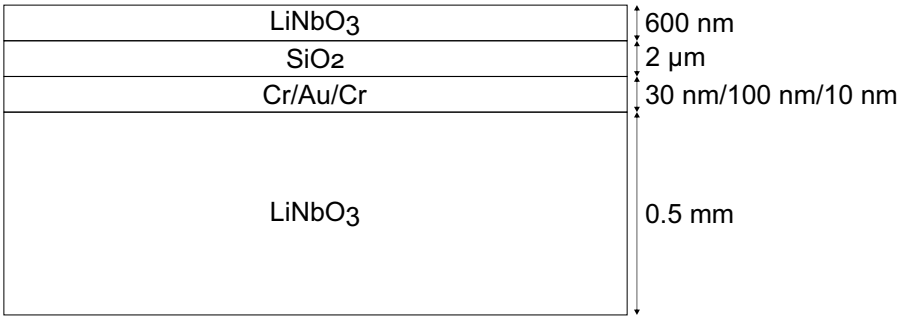

Figure 4.3: The layers and thicknesses of the LN thin film wafer.

The four tensor wafer description provided above relates to the four crystal planes detailed in Figure 2.4, which are associated with the three non-central

mirror planes through the crystal structure. Ideally, the wafer would have MgO doping in the thin film LN to increase the optical damage threshold. However, the wafer manufacturer could not provide both the MgO doping and the metal layer in the same wafer. The metal layer was chosen, in order to provide the THz confinement. A LN substrate was chosen for thermal stability, as cooling may be desired to examine the device when cooled for lower LN absorption, or in the application of injecting a QCL which must be run under cryogenic cooling.

4.2.2 Lithography and Etching a Rib

4.2.2.1 Test Rib Design

A mask is a pattern on a substrate which protects chosen areas from processes such as etching or deposition, used to create three dimensional structures. The mask for the waveguide needs be thick enough to withstand the etching. The mask must also be well formed, because any roughness in the mask will transfer to the rib during the etching process.

A mask was designed for some initial test ribs, to characterise NIR transmission through the LN waveguide. Consequently, the mask was designed so that many devices could be fabricated on a single substrate, to facilitate batch testing. The mask also allowed for long ribs (a few millimetres) to be fabricated for testing of propagation losses. The mask is seen in Figure 4.4.

The rib mask was designed on KLayout, a Computer Assisted Design (CAD) program for creating fabrication patterns. Initially a mask plate was designed, for use with contact alignment. The plate consisted of many test ribs across the whole face of the plate. This provided many different lengths and widths for ribs, as well as providing duplicates of ribs in case areas of the mask plate etched poorly during its creation. Contact alignment was eventually abandoned in favour of E-Beam lithography, due to producing poor mask features, discussed further in Section 4.2.2.2. Consequently, the design needed to be condensed as the E-Beam uses a 6x6 mm write area for the substrate size being used, due to the overlap between holder and chip. The updated design was made to allow for ribs of different lengths to be compared on the same substrate, so that the waveguide loss could be estimated. This meant the ends of the ribs were all at the same y-axis values, as seen in Figure 4.4. The x-axis spacing between the start and end facets is also constant in the ribs, so that alignment is made easier by not needing to adjust the in and out coupling sides of the test system. The position of the test sample can simply be moved instead. This is accomplished by using bends, and adjusting the distance between the bends. The bends have a radius of 100 µm, significantly larger than the radius at which the bend loss in an LN ridge are reported to become negligible [48]. The bends are purely used for testing purposes to characterise the losses, while the proposed device design is not intended to contain any bends. This pattern can be repeated many times along a substrate with the widths altered to provide a second variable to examine.

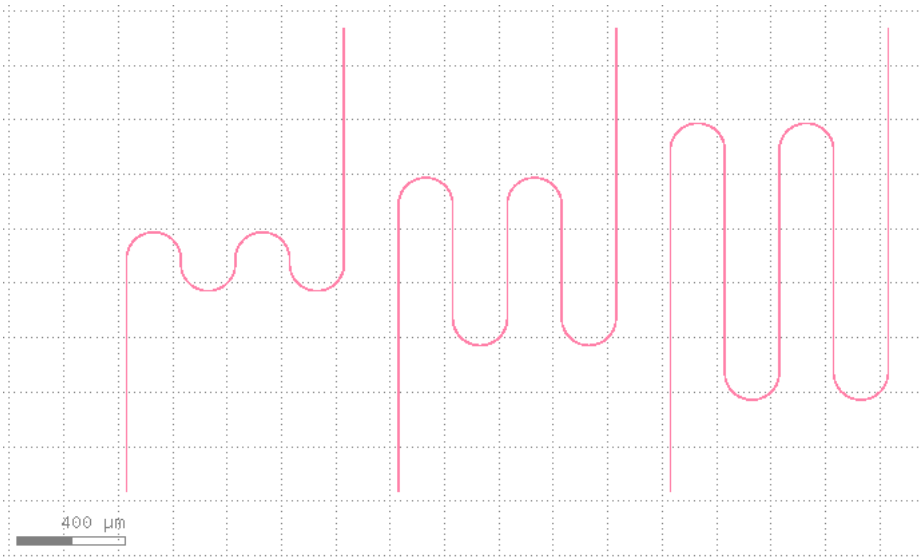

Figure 4.4: A screenshot of the rib design in KLayout. This designs allow for testing of propagation losses by having different length ribs on the same substrate, while the proposed design is not intended to contain any bends. A set of ribs with the same width is shown. The lengths from left to right are 3, 4 and 5 mm. The pattern could then be repeated with a different width, adjacent on the same sample.

4.2.2.2 Masking

When using the mask aligner, the feature size is very low due to the mask being in contact with the sample - with good contact the feature size can be sub-1 µm. However, when the light passes the mask, reflections of light within the resist occur, which can add up when working on scales of up to a few micrometers. Where these reflections have focused can cause the resist in those areas to become overexposed. This is shown in Figure 4.5a, where a cavity has formed along the length of the rib. It is particularly bad at the end of the rib, where the effect has been amplified due to where the light has reflected in from the resist end into a focused spot. Efforts to improve the contact of the mask, and therefore the sidewall quality, by removing edge bead from the sample as an additional initial step were unsuccessful, due to reflections caused by LNs optical transparency resulting in a cross-linked resist where none should have been exposed. Edge beads are areas where the spun substance has collected at the edge of a substrate due to surface tension.

After the contact aligner did not produce a good enough profile, E-Beam lithography was used to create a resist mask. The E-Beam takes the design from KLayout and precisely recreates it using a focused beam of electrons. Firing a primary electron knocks out a secondary electron and creates scatter.

Ideally the electrons scatter forwards to achieve a small write width, although they can also back scatter, displacing further electrons and widening the write width. This technique created a far superior profile to the contact aligner, as shown in Figure 4.5b.

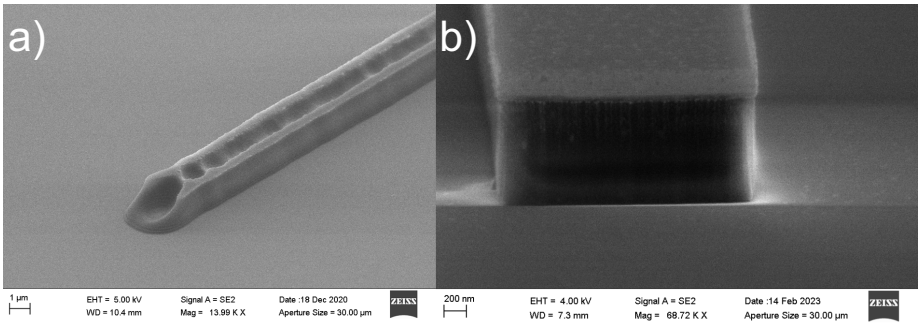

Figure 4.5: SEM images of resist masks by a) mask aligner and b) E-Beam. Images courtesy of Dr. Mark Rosamond.

For E-Beam processing, SurPass4000 adhesion promoter was spun on with in-situ IPA rinse. The resist used was MAN2403 at 2000 rpm, providing approximately 450 nm thickness, and followed by a 90°C bake for 2 minutes. ARPC5091.02, which is a water soluble polymer, was then spun on to act as a conductive film during the E-Beam lithography process.

The KLayout design was broken up into a 10 nm fine grid of many trapezoid shapes which acted as write areas for the E-Beam, and were fractured to deal with the curves of the waveguides. The ribs were written with a minimum linewidth of 300 nm. Small pecks were used for write time to obtain appropriate energy distribution for the dose in each area, where dose is equal to intensity of the UV ray multiplied by time the beam spends in one location. The minimum dwell time, 40 ns, was dependant upon the scanner frequency, which was 25 MHz. Three substrates of test ribs were written at 2 nA, with doses between 550 and 620 µC. These substrates are labelled 1, 2, and 3. After the write process, the water soluble polymer was removed with 3 baths of DI water, before development using MF-322 for 90 seconds. The initial sample batch, tested later in Section 5.1, were all slightly overdosed. This was evidenced by the test squares of each sample. These squares of resist appear a different colour under a microscope depending upon how high a UV dose they have received, which is used as an indicator of lithography quality.

After trials with contact lithography, E-Beam lithography has been chosen as a more successful mask making process for fabricating these low loss LN waveguides with smooth sidewalls, due to a small feature size and lack of undesired reflections. Using this high quality mask, the next step is to trial etching the mask using ion milling in order to establish which process parameters provide the smoothest sidewalls for the waveguide.

4.2.2.3 Etching

The angle of the sample in the ion beam is a key parameter for ion milling. One paper of relevance, *Ultra-low loss ridge waveguides on lithium niobate via argon ion milling and gas clustered ion beam smoothening* by Siew et al., stated that they milled at an angle close to the normal (83°) for 40 minutes, before switching to milling at 30° at a lower power for three minutes at the end. This was done to remove resputtered material and reduce sidewall roughness by milling the sidewalls directly. In their experiment the sidewalls are further smoothed using a gas clustered ion beam [74].

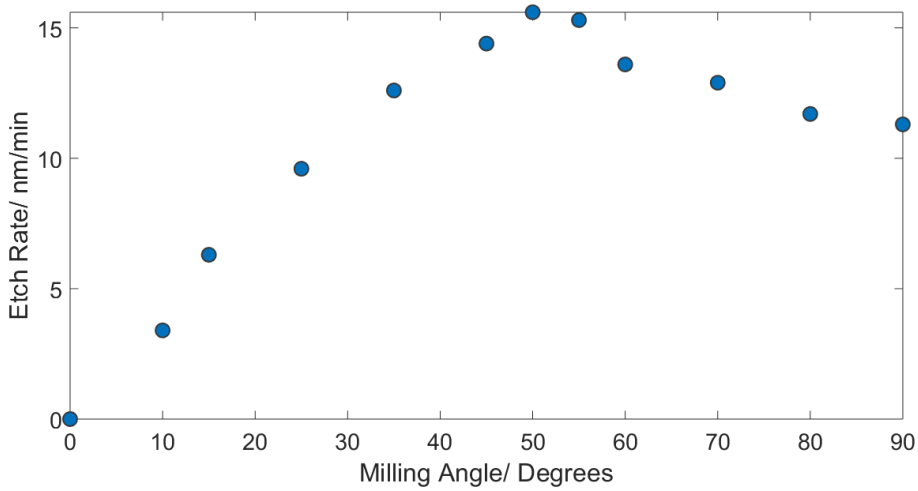

Figure 4.6: A plot displaying the effect of etch angle on milling rate of LN in the ion miller. A thin film LN sample had its film thickness measured via ellipsometry, milled and then remeasured after a set time to measure the difference and calculate etch depth by time. The measurements were taken in an inert air environment, using the following ion miller settings; 250 W, 500 V beam, 750 V accelerator, 200 mA neutraliser, 6 sccm Ar neutraliser, 15 sccm Ar source, stage rotation at 5 rpm, 7 mbar, 10°C.

To investigate the angle dependence of LN in the UoL ion miller, a variable angle experiment was performed. An etch was performed on an unpatterned thin film LN sample at angles between 0° and 90° for a known quantity of time, and the thickness of the LN thin film was measured via ellipsometry between every etch. The time was varied to ensure that a measurable amount of LN had been etched, without etching a significant proportion of the thin film away so it could be used for the next measurement. The difference in film thickness before and after each etch allowed an etch rate to be calculated for each angle. The results are seen in Figure 4.6.

The samples were mounted in the ion miller using thermal grease. This provided good thermal contact for heat dissipation. 90° is defined as the angle

when the beam is normal to the sample top surface. At 0° the film thickness is not reduced as the beam does not hit the top of the sample. Increasing the angle increases the etch rate up to a maximum as the beam is pointed more directly at the sample surface, increasing the intensity of the etch. After this maximum at around 50°, the etch rate drops slightly and starts to level off, as seen in Figure 4.6. This is because the likelihood an ion being reflected rather than etching increases [156]. The plot follows what is expected from literature about dry etching processes [157].

Another angle dependence experiment was performed, this time on thin film LN with ribs patterned on them in resist. Five different initial milling trials were attempted:

- 90° (at normal)
- 60°
- 50°
- 25°
- Variable angle, at:
    * 60° for 3 minutes 40 seconds
    * 30° for 1 minute 20 seconds
    * Repeated twice

The variable etch was an attempt to replicate the results given by Siew et al. [74]. Each etch lasted for 15 minutes. In the case of the variable angle etch, three full cycles of 5 minutes each were performed. However, the miller software crashed when attempting the variable angle etch. The etch results were examined using SEM to view the sidewall profile. The samples were sputter coated with gold in order to provide a homogeneous conducting surface for analysis in the SEM. The best etch successfully performed was the 50° etch. The 50° etch is shown in Figure 4.7. The other angles, 90°, 60°, and 25°, are shown for comparison in Figure 4.8, 4.9, and Figure 4.10 respectively. The images show the ribs sitting atop a shallow incline in the LN, an effect caused by mask shadowing. These samples had end faces exposed by snapping the substrate over a sharp edge. The sidewall angles and roughness were examined by eye using the SEM for this initial trial.

Substrates 1, 2, and 3 from Section 4.2.2.2 were milled as their next processing step. These were milled at an angle of 85°, using the same miller settings as the thin film tests, listed in Figure 4.6. This angle, close to the normal, was chosen due to causing a high amount of redeposition, which could then be used to trial wet etching as a smoothing step for the side walls. After the ion milling, SVC-14 resist stripper was used to remove the remaining resist, before putting the samples in an oxygen plasma asher for five minutes at 50 W to ensure they were clean of organic particulates. The sidewalls were measured to have an aspect ratio of 5:1, a little over 10° from vertical.

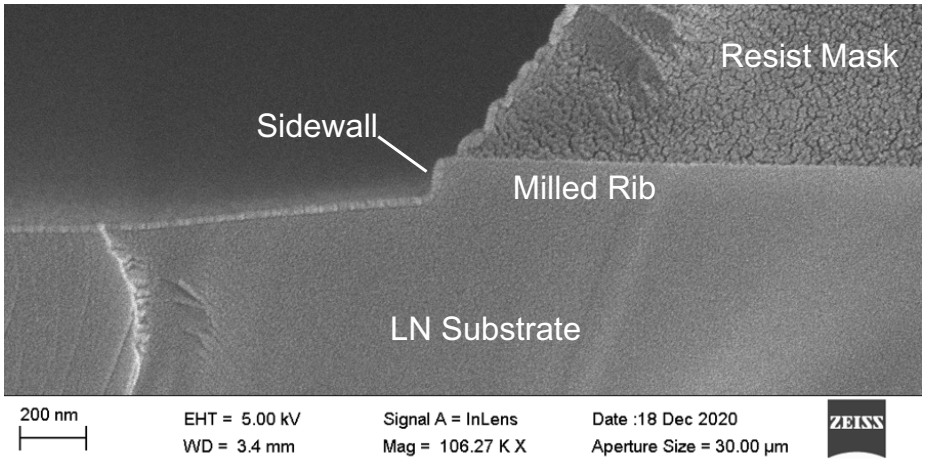

Figure 4.7: An SEM image of a rib milled in bulk LN. It was milled at an angle of 50° in the ion miller. The image shows the partially milled resist mask on top of a LN step. This angle of mill demonstrated a sidewall which was smoother and closer to perpendicular than the other attempted etches. Image courtesy of Dr. Mark Rosamond.

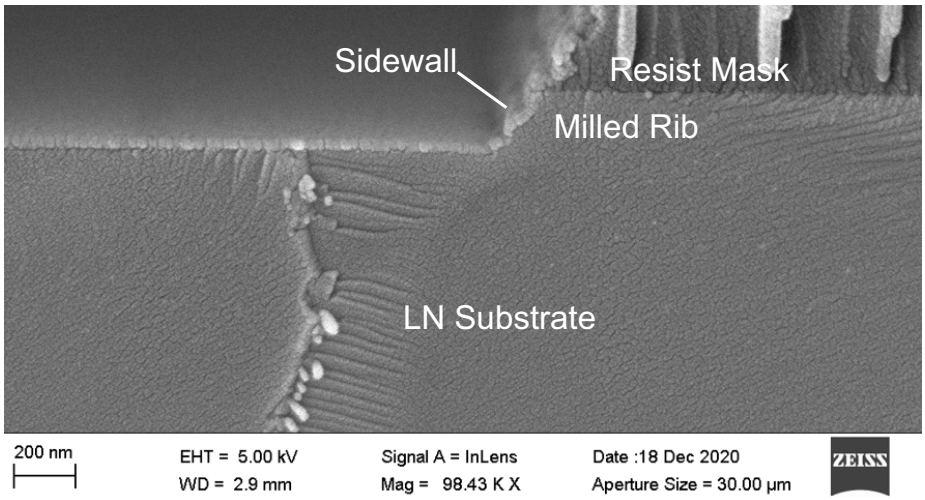

Figure 4.8: An SEM image of a rib milled in bulk LN. It was milled at an angle of 90° in the ion miller. The image shows the partially milled resist mask on top of a LN step. The sidewall from this mill is noticeably rougher than the 50° etch in Figure 4.7. Image courtesy of Dr. Mark Rosamond.

Wet etches were then performed. This was done to see if the milling redeposition could be chemically removed. Each substrate was subject to a different

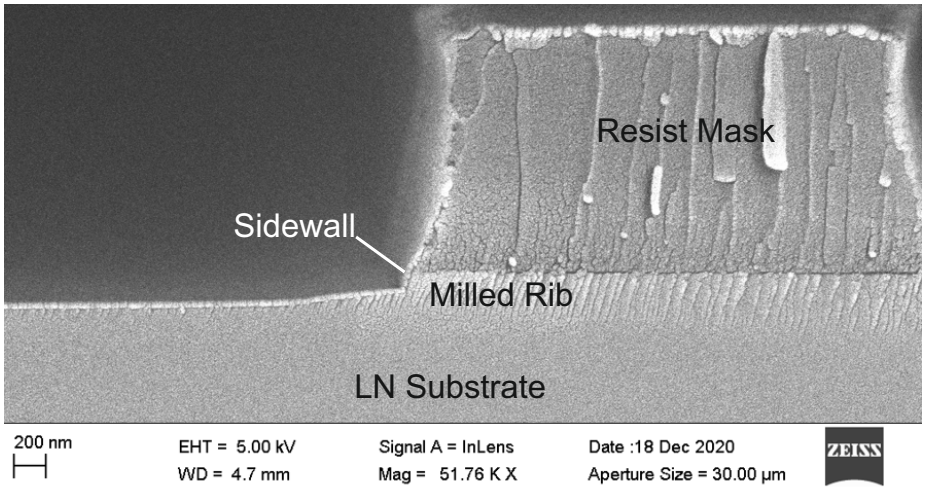

Figure 4.9: An SEM image of a rib milled in bulk LN. It was milled at an angle of 60° in the ion miller. The image shows the partially milled resist mask on top of a LN step. The sidewall from this mill is not as vertical as the 50° etch in Figure 4.7. Image courtesy of Dr. Mark Rosamond.

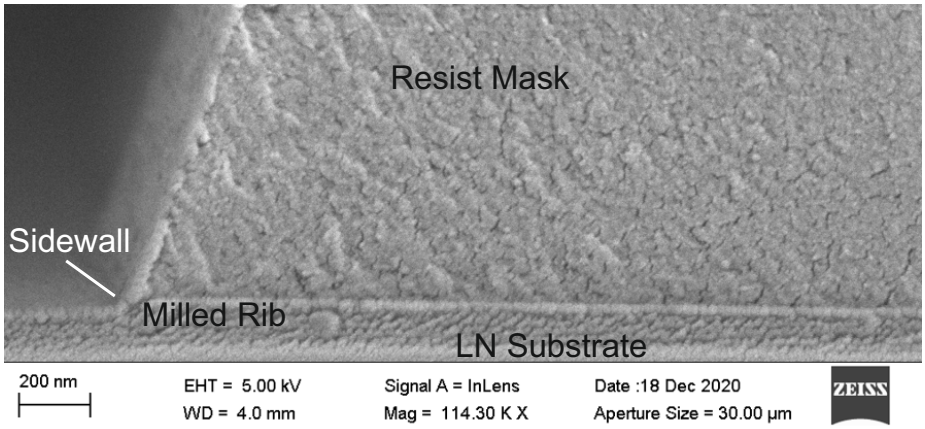

Figure 4.10: An SEM image of a rib milled in bulk LN. It was milled at an angle of 25° in the ion miller. The image shows the partially milled resist mask on top of a LN step. The etch has not created sidewalls as large as the other etches, and they are less vertical than the 50° etch in Figure 4.7. Image courtesy of Dr. Mark Rosamond.

type of etchant, in order to compare their effects. The concentration by volume of the solutions used for substrates 2 and 3 were both 3:1.

- Substrate 1) Buffered HF: No change to substrate.

- Substrate 2) H_2SO_4:H_2O_2: 3 nm change to substrate after 30 minutes, a negligible and unreliable change.
- Substrate 3) NH_4OH:H_2O_2: High etch rate and ruined substrate surface with high roughness, etched 200 nm in 27.5 minutes.

The results were measured using ellipsometry, as any wet chemical etch will remove the ridge and substrate surface at the same rate, resulting in no step change to be measured using a surface profiler. The results led to the conclusion that the sidewall roughness is difficult to chemically remove. Therefore, it is best to optimise the milling angles and times.

Following the wet etch trial, Substrate 1 was diced into 27 test ribs. These ribs are characterised in the NIR regime in Chapter 5.

4.2.2.4 Chrome Mask

A chrome mask was tested as an alternative to a resist mask, following promising results from literature [158]. The chrome mask was applied via evaporation on to a sample. This was done after lithographically defining a rib in resist, so that lift off could then be performed in a solvent, resulting in the patterning of the chrome mask. The lithography therefore needed to be good quality, like the resist mask, due to using it to form the chrome mask.

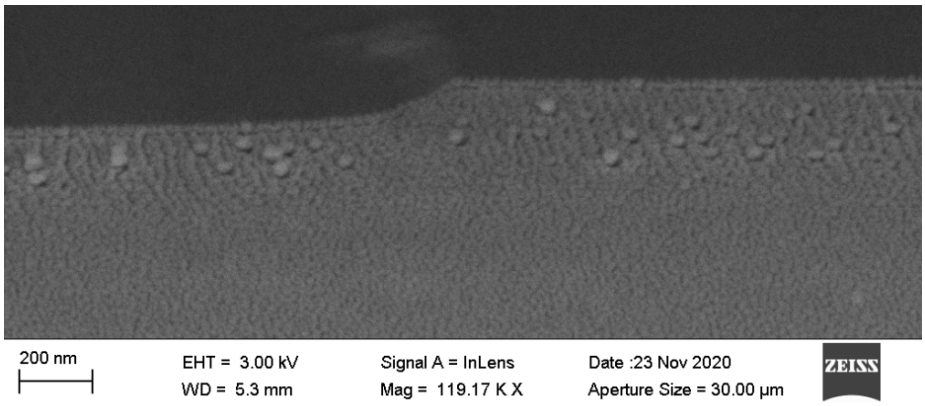

Figure 4.11: An LN rib formed using a chrome mask and milled at 50°. The sidewall angle is notably shallow in comparison to the resist masked rib milled at 50°, caused by the chrome mask being completely milled away. Image courtesy of Dr. Mark Rosamond.

The chrome mask created a rib with a shallow sidewall angle, shown in Figure 4.11, compared to a resist mask formed rib, shown in Figure 4.7. This is because the chrome mask was completely etched away before the completion of the milling process. The conclusion drawn from this is that the chrome etches much faster than a resist mask. This means a tall chrome mask would be needed

for a successful etch, which could lead to substrate shadowing and consequently poor etches. For this reason the resist masking was chosen as the preferred processing step.

4.2.3 Etching with a Charge Dissipating Layer

A second thin film LN wafer was obtained, henceforth referred to as 'Wafer 2'. This wafer differed from Wafer 1 by having an Si substrate rather than an LN substrate. A Silicon substrate simplifies processing because there are no charging effects. Additionally, Wafer 2 had MgO doping in order to facilitate a higher damage threshold, rather than the implanted gold layer. The gold layers are not required if using horizontal polarisation, which is expected to provide a better performance following the simulation work in Section 3.3.1. The absence of a gold layer facilitates the extraction of THz through the substrate, as discussed later in Section 6.1.

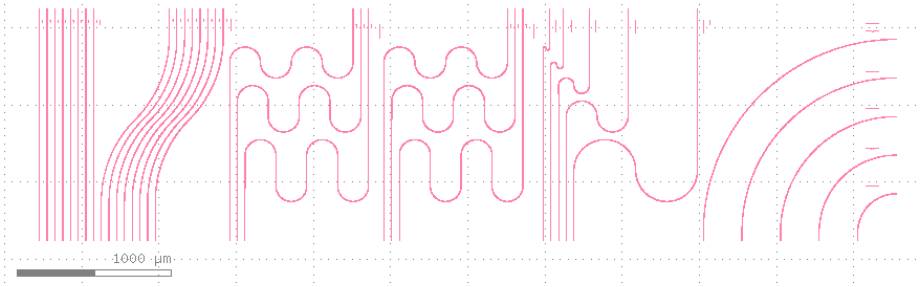

Figure 4.12: A screenshot of the E-Beam lithography design for ribs for the later batch of ridges. The design was made using K-Layout. These designs allow for testing of propagation losses by having different length ribs on the same substrate. Different rib shapes are added for purposes of analysing bend loss, and avoiding scatter of input light at the detector of the testing setup.

Wafer 2 was processed into further test ribs. Some changes were made to the fabrication while trying to optimise the milling process. New rib designs were created using K-Layout, for NIR performance tests. The design is seen in Figure 4.12. The variety of ribs here allows for a greater breadth of testing. They use the premise of helping alignment by having an equal distance between ends of ribs, like the ribs fabricated for Wafer 1 seen in Figure 4.4. The straight ribs are the style required for the finished waveguide, and are desired for testing as it is unknown how much bend loss there was on the previous test ribs from Wafer 1. Straight ribs can be tricky to characterise during NIR testing however, due to the scatter from the input optical fibre, as there are no cladding layers for the test ribs at this point to stop light going over the top of the rib. This is described further in Section 5.2. The aim of having smooth 'S' shape bends is that they will take away some of the scatter by displacing the end detection system while not providing large bend losses. Further to this, there are more

ribs of the previous bend shape for a comparison to the ribs from Wafer 1. There are also ribs with a single bend, where each rib has a progressively larger bend, in order to measure bend loss. This allows for experimental confirmation that the bend loss above 20 µm is minimal [48]. Finally, there are some ribs that gently bend to 90° in different lengths, in order to characterise the ribs without so much glare from the input fibre if scatter issues persist, with the system set up so that the detector can be placed that side of the sample.

4.2.3.1 Oxide Mask

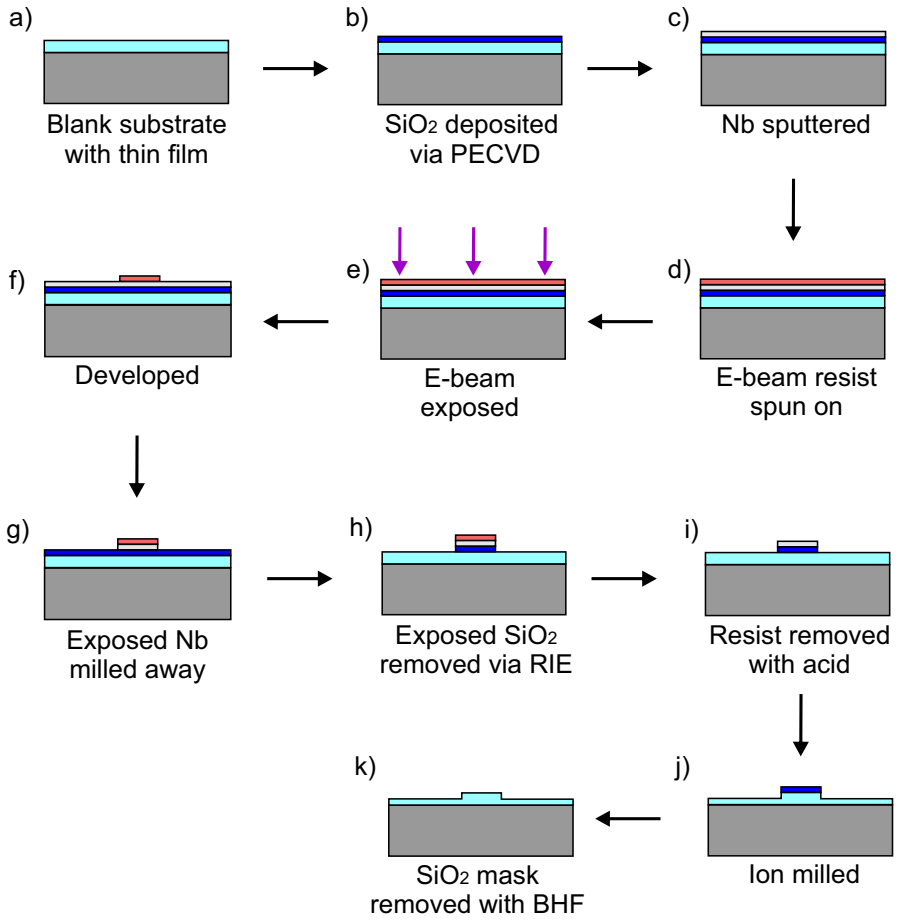

Figure 4.13: The steps of fabricating a rib in thin film LN using an ion milling procedure. BHF stands for Buffered HF.

A new type of mask was attempted using samples of Wafer 2, to see if it provided a better rib shape. The processing steps are illustrated in Figure 4.13.

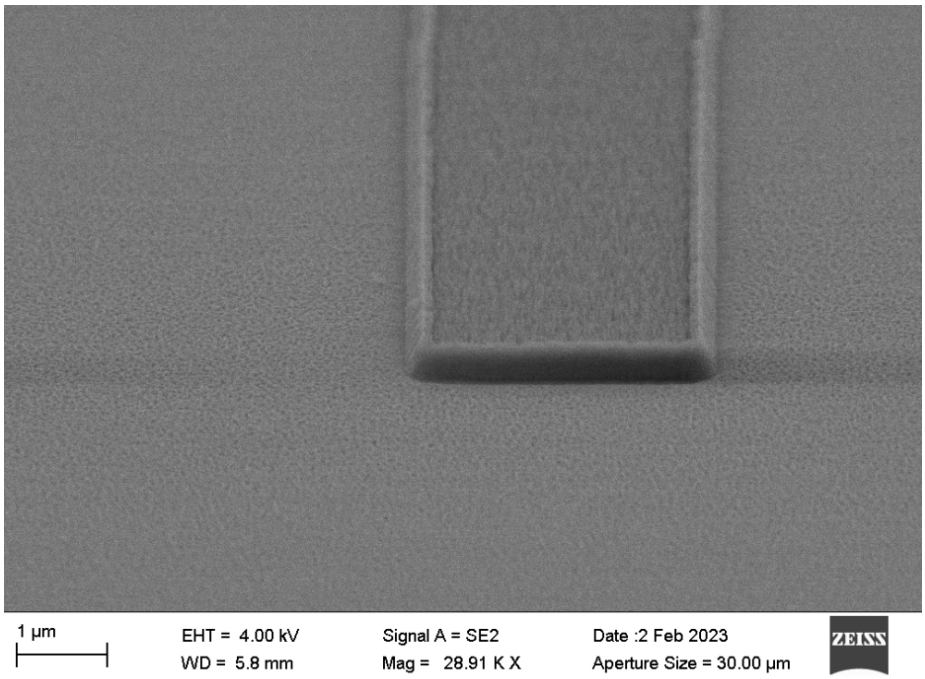

Figure 4.14: An SEM image of the oxide masked sample after RIE and H_2SO_4:H_2O_2 etching, and before milling. Image courtesy of Dr. Mark Rosamond.

The new mask was an oxide mask, consisting of PECVD deposited SiO_2, with a layer of niobium sputtered on top. This was done to form a conductive layer for E-Beam lithography. Sputtering was used as the deposition method because it results in a good quality thin film. ARN7520.11 was spun on next, which is an E-Beam resist. This was used instead of the MAN2403 E-Beam resist used for the previous ribs as it was believed it would provide increased adhesion, due to the UoL stock of ARN7520.11 being in date while the MAN2403 resist had expired. Ribs were then defined using E-Beam lithography, and the niobium milled away after. The sample was then RIE etched, to expose the LN surface by removing the unwanted areas of SiO_2. RIE was performed because it reacts with SiO_2 for the etch. An additional buffered HF rinse at this point can be used to clear the areas between the ribs of remaining SiO_2, with care taken not to start etching the mask. An H_2SO_4:H_2O_2 solution was used to remove the resist, leaving the SiO_2 mask. The mask is seen in Figure 4.14.

After the ion milling, the SiO_2 mask was removed using buffered HF acid. Figure 4.15 shows the final product. The resulting sidewalls from these samples were very rough, much more so than expected from work in a different UoL project using an oxide mask. This is believed to be due to the large spaces between the ribs, rather than etching smaller features. It is worth noting that

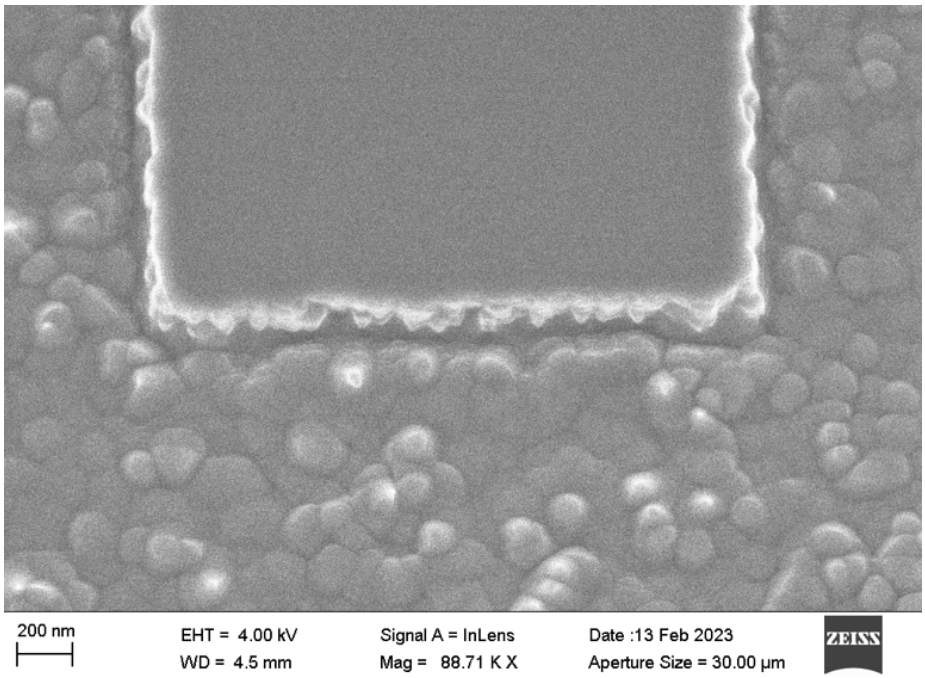

Figure 4.15: An SEM image of the milled LN ridge after the remaining oxide mask has been removed. A large surface roughness is seen around at the sides of the rib. Image courtesy of Dr. Mark Rosamond.

the RIE process parameters were not optimised for ribs and large spaces between features. There was also an oxide film forming on the LN surface during the milling process, which needed to removed post etch using an H_2SO_4:H_2O_2 solution. The oxide mask was discovered to not be very selective under ion milling, as two of the samples had the mask etched through.

4.2.3.2 Resist Mask

Due to the poor sidewalls and selectivity from the oxide mask, the resist mask was returned to for the next set of samples. An alternative resist method was trialled. The processing steps are illustrated in Figure 4.16. This differed from the earlier resist mask described in Section 4.2.2.2 due to the incorporation of a charge dissipating layer, as used in the oxide mask.

Because the E-Beam resist available would not spin to high thicknesses, a layer of S1813 resist was deposited first, and entirely cross-linked to avoid lithography. The e-beam resist available was ARN7520.11 and spins to around 0.2 µm thickness at 4000 rpm. A thickness large enough to ensure that the mask is not milled through is required, else the rib will also start getting milled, stopping it from gaining any height over the rest of the thin film as well as inheriting top

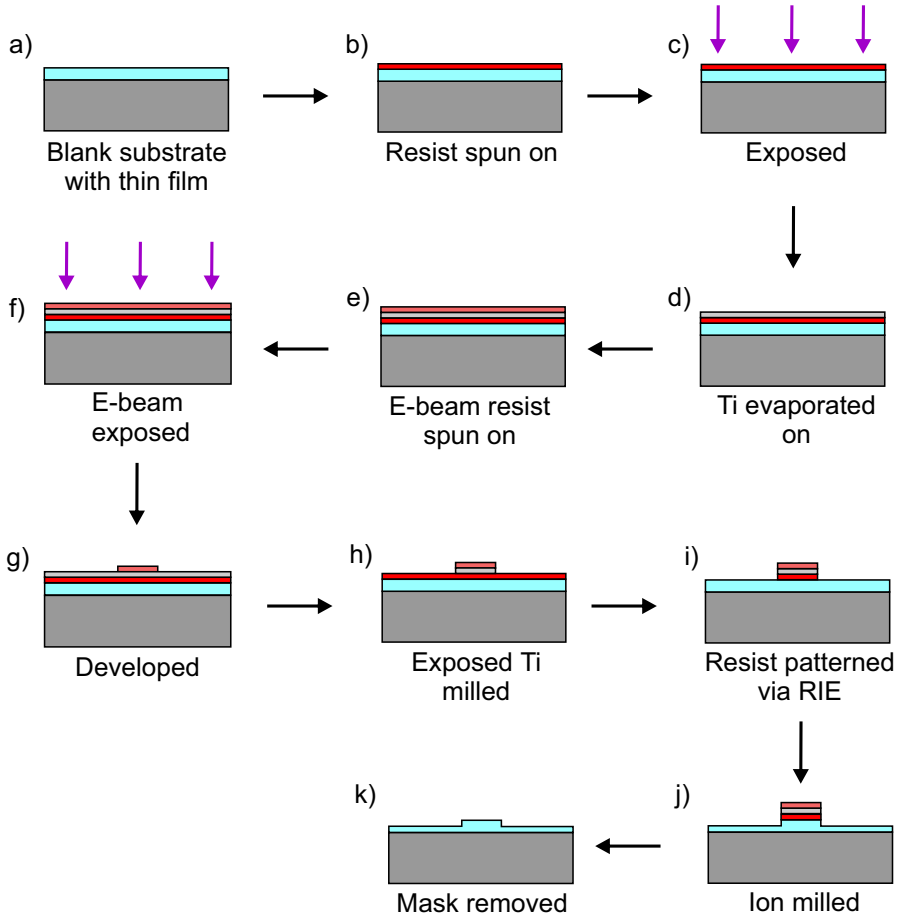

Figure 4.16: The steps of fabricating a rib in thin film LN using an ion milling procedure.

surface roughness from the resist profile. Around 0.4 µm of resist is needed for the 0.3 µm ribs being fabricated for this work. This thickness is slightly more than the rib height and will be enough because the resist and LN will mill at similar speeds, while not having too much extra height and causing shadowing during the mill. After the initial resist layer, a thin titanium layer was used, in order to conduct charge during the E-Beam lithography process. Titanium was used instead of niobium this time as the niobium was more difficult to fully remove than anticipated. Following this, a layer of the ARN7520.11 E-Beam resist was spun on. After patterning development, the exposed titanium was milled away by ion beam, before transferring the pattern into the S1813 layer using an oxygen plasma in an ICP-RIE. The complete mask is seen in Figure 4.17, approximately 0.9 µm thick. These samples were then placed in the ion miller.

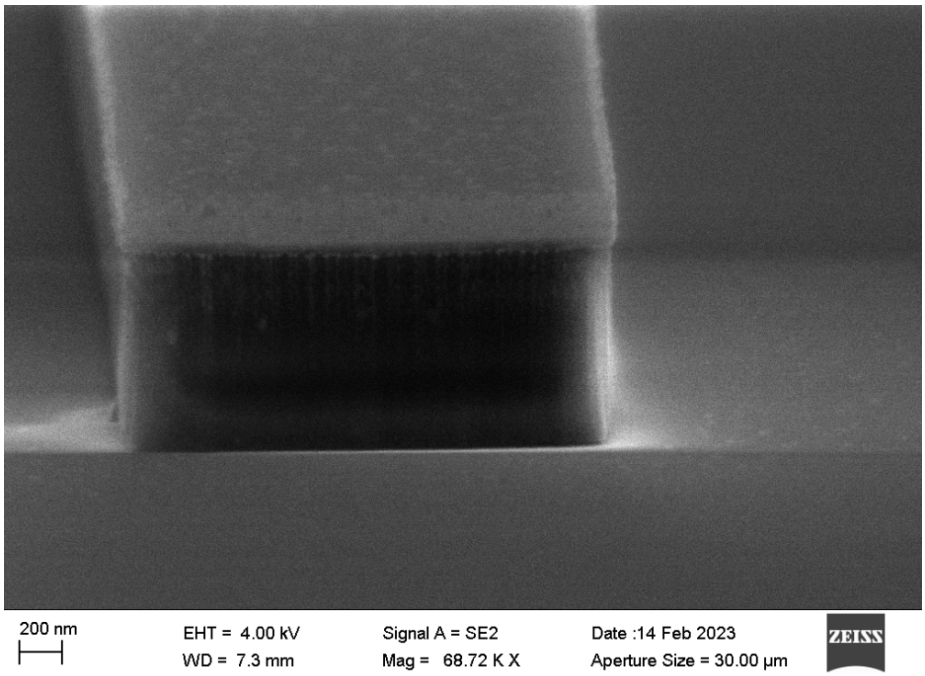

Figure 4.17: An SEM image of the resist mask before milling. Image courtesy of Dr. Mark Rosamond.

The finished rib after mask removal is seen in Figure 4.18. It can be seen that the smoothness of the sidewalls from these samples is much better than those of the oxide mask from Figure 4.15.

Having added the extra resist layer, the height of the mask was great enough to cause high amounts of shadowing, resulting in some tapered rib heights. This can be seen with close examination in Figure 4.18, and with more clarity in a surface profile shown in Figure 4.19, taken by AFM. There is a version of the E-Beam resist, ARN7520.17, which spins to a thicker layer, which has been acquired for future work. At 4000 rpm the ARN7520.17 film thickness is quoted at 0.4 µm [159]. This will remove the need for the additional S1813 layer, bringing down the overall mask height and reducing the shadowing.

The fabrication of low loss LN waveguides has been improved upon by the incorporation of a charge dissipation layer, and resist has been confirmed as the mask of choice after trialling an oxide mask.

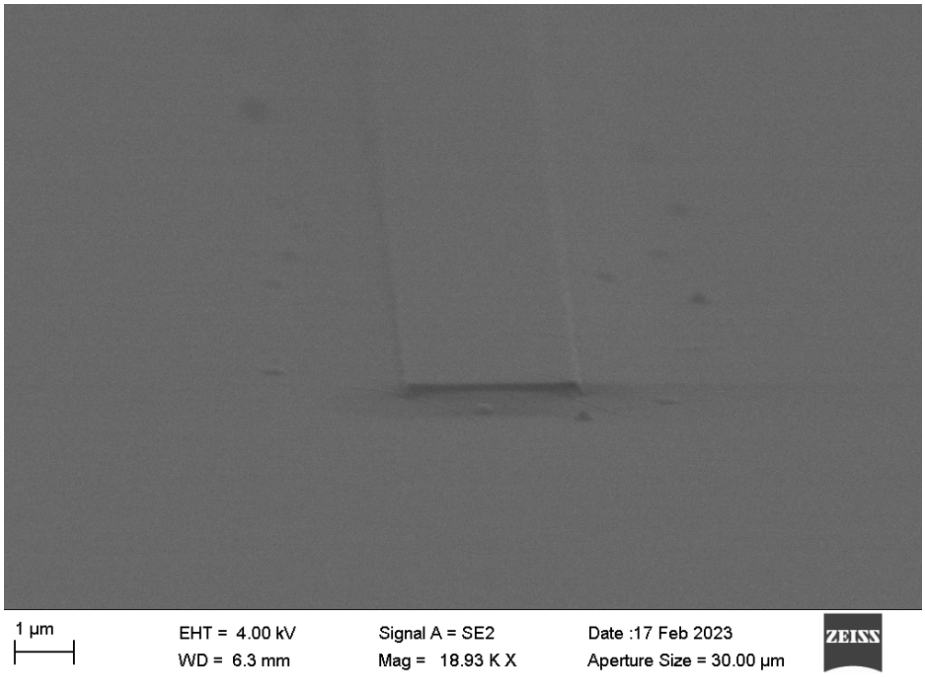

Figure 4.18: An SEM image of the milled LN rib after the remaining S1813 resist mask has been removed. The bottom of the sidewalls are sloped due to the large height of the resist mask causing shadowing. Image courtesy of Dr. Mark Rosamond.

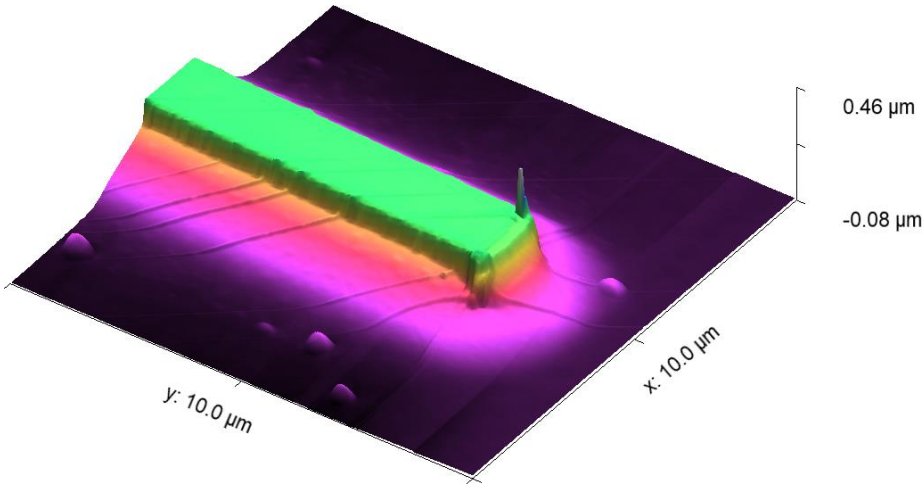

Figure 4.19: The surface profile of a rib made using an S1813 resist mask taken by Atomic Force Microscopy (AFM). Image courtesy of Dr. Mark Rosamond.

4.2.4 Precision Cutting a Ridge

Precision cutting with a circular saw was attempted as a substitute means of rib fabrication while waiting for the ion miller to receive repairs. If tests conclude that dicing is not suitable for rib fabrication, it is nevertheless important to ensure good dicing practices for the creation of the ridge facets.

The concept of dicing ridges is to cut two parallel trenches into the LN, forming a ridge between them. This has been shown by others to produce ridges with propagation losses as low as 0.2 dB/cm [160]. Ridges rather than ribs are made, as the precision of the UoL wafer saw is not high enough to restrict the cut to only the thin film of the substrate.

First, the blade is 'dressed' using a dressing board; a board that the blade is run across several times in order to wear the blade into the correct shape along the cutting axis to facilitate a better cut. Slow cutting settings were selected to try and minimise chipping of the LN. If the cut ridge is of a high enough quality, it could then be annealed at >1000°C in an attempt to reconstruct the crystal structure after minor cutting damage.

Following excessive chipping of the ridges using the UoL stock blades, seen in Figure 4.20, new fine grit blades were bought. These blades, acquired from Disco, are Z09 series; electroformed bond blades with fine grits for high cut quality, designed for deep straight cuts. The blades have a grit type of synthetic diamond and grit count of 5000. These specific blades were obtained because they match the blade used in *Ductile dicing of LiNbO3 ridge waveguide facets to achieve 0.29 nm surface roughness in single process step* by Carpenter et al. [72], work this experiment was attempting to recreate.

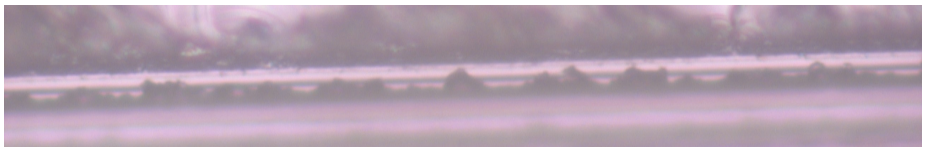

Figure 4.20: A microscope image of a cut made by using the wafer saw and the UoL stock blades to cut parallel trenches. The cut is poor due to large chipping, although it appears much worse on one side compared to the other.

These new blades were used in an endeavor to achieve ductile dicing. Ductile dicing is where the process parameters keep the material shear strain under a critical threshold value, which means that the cutting process is performed by plastic deformation, which provides sub-micron roughness and prevents chipping [161]. An SEM image from the Carpenter et al. paper displaying the high quality of their result is displayed in Figure 4.21 [72].

The blade is initially dressed on the dresser board using the following settings, aiming to wear 0.03 mm of blade:

- 20,000 rpm
- 0.3 mm cut depth

Figure 4.21: An SEM image from *Ductile dicing of LiNbO3 ridge waveguide facets to achieve 0.29 nm surface roughness in single process step* by Carpenter et al. [72]. This quality of wafer saw cut is what the ductile dicing experiments with the new blades were trying to achieve.

- 10 mms^{-1} feed rate
- 10 cut lines

These were the recommended settings from Disco.

The initial wafer saw settings used for dicing the ridges are as follows, influenced by literature [72]:

- 10,000 rpm
- 5 µm cut depth
- 0.2 mms^{-1} feed rate

Key cut parameters were varied, to analyse their influence on creating a cut with minimal chipping. This included altering the feed rate, spindle speed, and cut depth. Cuts on the sample were trialled at feed rates of 0.1, 1, and 1.5 mms^{-1}. Spindle speeds were varied between 10 and 30 krpm. The blade parameters state not to go above 30 krpm spindle speed. Cut depths of 25, 50 and 100 µm were tested. Cutting less deep allows smaller trenches to be cut, for less horizontal confinement. The blade shape however, which comes to a point at the edge rather than being the width of the blade, means that shallow cuts do not have vertical sidewalls. Additionally, shallow cuts may have high chipping at the surface. A deeper cut will be vertical as the whole blade width cuts into the substrate.

Most of these tests were inconclusive due to sample movement. The UoL wafer saw is designed to dice whole wafers, not precision cut small samples. Sample to stage adhesion was low due to the small sample size. The resulting sample movement caused cuts that were not precise. A proposal for future work is to use wax to mount a sample onto a large piece of spare wafer. This will

provide an increased adhesion to the stage due to the large size of the wafer mount. Tape with a higher adhesion for use on the wafer saw stage has also been acquired for future work as an alternative solution.

When clean cuts were successfully performed, a pattern of issues seen in the ridge shape formed. The two sides of the ridge did not have the same sidewall angle, seen in Figure 4.22, or top surface profile, seen in Figure 4.23. The tearing seen in Figure 4.23 is particularly problematic, as the damage is in the magnitude of microns; too large for use in the thin film substrates. The discrepancy between the two sides of the ridge can be explained by the blade not being aligned perfectly to direction of travel, causing damage as it runs along the samples. A possible reason for this is that the UoL wafer saw does not have an air slider, unlike those in the papers which have successfully demonstrated this technique.

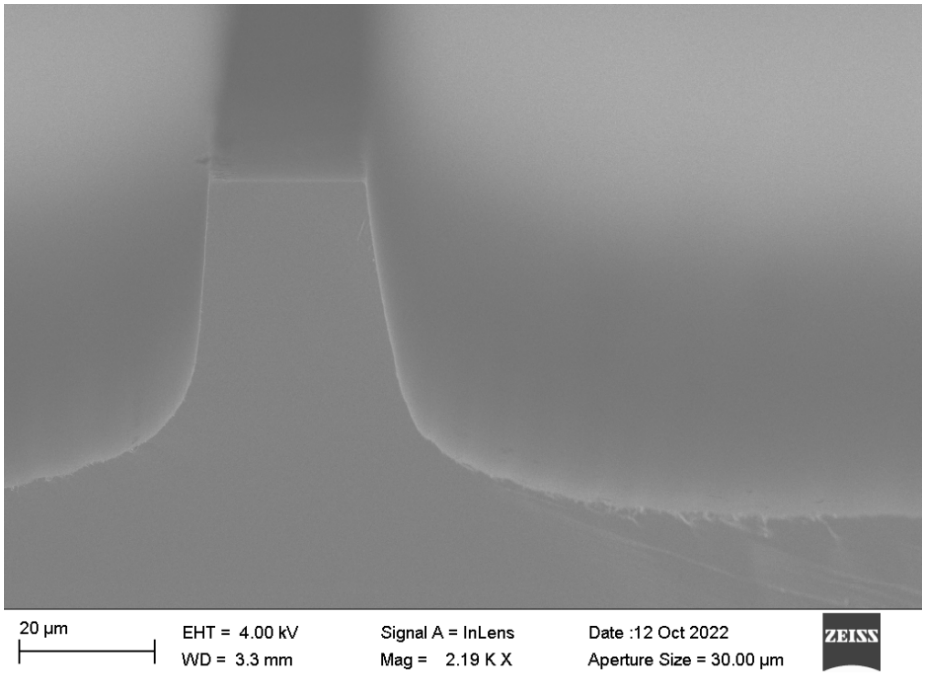

Figure 4.22: An SEM image of a 50 µm deep ridge cut in bulk LN with the wafer saw. It can be seen the profile of the ridge is different on either side, with the angle of the sidewalls different to each other. Image courtesy of Dr. Mark Rosamond.

The torn edges and sidewall angle profile can be partially remedied by rotating the sample 180° between cuts. This will mean the same side of the blade is used for either side of the cut ridge. The better side of the ridge, however, has also taken damage, though to a lesser extent, as seen on the left side of the ridge in Figure 4.23.

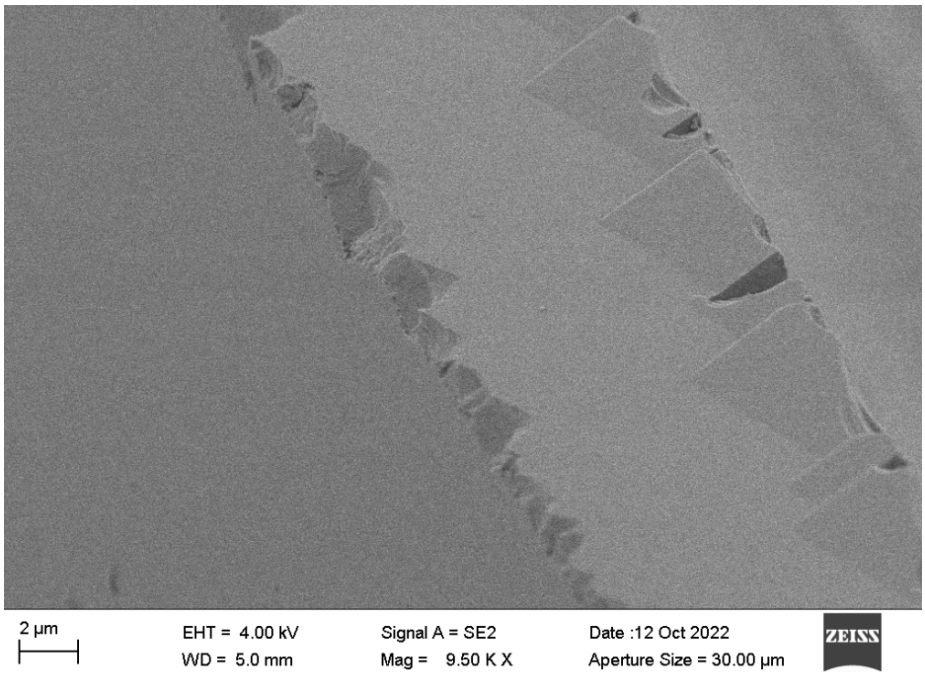

Figure 4.23: An SEM image of the top of a ridge cut in bulk LN by the wafer saw. It can be seen that both sides of the ridge have suffered damage, but the right side in particular appears to have the appearance of tearing. The size of this damage is in the order of microns, not acceptable for the thin film ridges. Image courtesy of Dr. Mark Rosamond.

An attempt was made at protecting the top of the LN by depositing a layer of SiO_2 on top via PECVD, as the rest of the cut depth past the top surface is smooth, despite the angle profile being different, evidenced in Figure 4.22. After the cut, wax was then used to protect half of the sample while it was submerged in HF acid to remove the SiO_2 layer. After removing the wax it is seen that the SiO_2 did not make a significant difference to the cut quality of the LN top surface, as seen in Figure 4.24. The chipping seen in the SiO_2 has been transferred to the LN underneath, meaning it is not a suitable method of protecting the LN ridge as it is being cut.

With the current equipment available at UoL, using the wafer saw to fabricate a rib is not a viable option due to the significant tearing seen at the sample surface. To replicate the quality of other works, such as is seen in Figure 4.21, a blade more aligned to the direction of travel is needed, from a wafer saw model with an incorporated air slider.

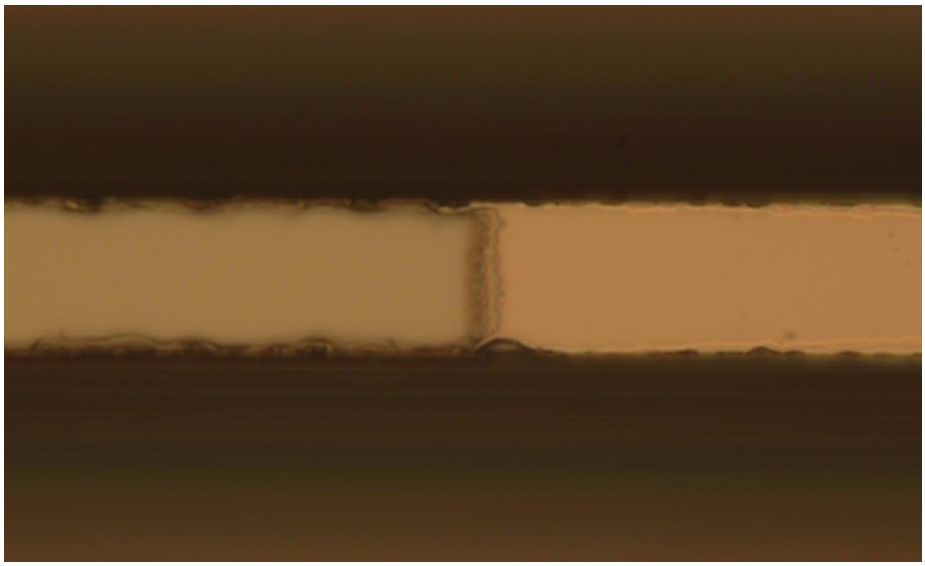

Figure 4.24: A 50x magnification microscope image of an LN ridge cut using the wafer saw, with SiO_2 covering only the left half of the sample, having been removed from the right half by an HF etch. Chipping can be seen in both halves of the sample.

4.3 Waveguide Facets

This section details different attempts to improve the coupling of light into and out of the waveguide by improving the quality of the rib facets. Fabricating a sample with a good facet is important in order to reduce coupling loss as much as possible. What is required is a sample which has a smooth end face. This reduces the amount of light scattering away when reaching the surface of the waveguide face. Commonly the fibre to LNOI coupling is more than 10 dB per facet [162], although with care these losses can be brought closer to 1 dB at 1550 nm [94]. It is especially important to have a low NIR coupling loss, as high losses of the pump beams leads to less efficient THz generation due to lower efficiencies.

The three trialled methods are:

- Wafer Saw Cutting
- Focused Ion Beam
- Polishing

A common method which has been excluded is scribing. Scribing introduces a 'V' shaped cut in the sample surface, and is then snapped along the cut line, resulting in a clean break, assuming it is along a crystal plane of the wafer. This

is unsuitable here due to the Z-cut LN wafer, which does not have a crystal plane along the wafer surface to cleave across.

4.3.1 Wafer Saw Cutting

When dicing a wafer in order to create samples, facets are made along the edge of the substrates at the sample cut. If these edges are already suitable for optical coupling then this removes the need for further processing.

An attempt at creating usable facets was performed using a two step process, whereby the high grit blade and cutting parameters detailed in Section 4.2.4 were used to create a clean cut across the sample surface, before changing the blade to one with a less fine grit and moving a few micrometres away from the initial cut to cut through the bulk of the substrate. However, this does not yield a high enough quality cleave due to the issues of blade travel and the sample adhesion, outlined in Section 4.2.4. High movement of the sample caused high chipping rates, observable by optical microscope on low magnifications, unsuitable for fibre coupling.

4.3.2 Focused Ion Beam

A Focused Ion Beam (FIB) is an instrument which ablates material in micro and nano scale quantities by firing a focussed beam of ions at a sample. The FIB model used in the UoL is the Field Electron and Ion Company (FEI) Helios G4CX dual beam FIBSEM, from the Leeds Electron Microscopy and Spectroscopy (LEMAS) department. It has a built in SEM with a Field Emission Gun (FEG) for optimal resolution. Using a FIB on end facets is a technique others have employed for LN waveguides [94, 141].

To use the FIB, the sample is placed into the SEM, which is then used as the targeting system for a focused ion beam to fire at the sample, ablating the surface, making a very clean mill on the targeted area. One aspect of the FIB method is that the facet is now recessed, as seen in Figure 4.25. This makes alignment of the rib in the testing setup more critical, because if not aligned well then the coupling loss will be larger, as part of the free space beam emitted from the optical fibre will be shadowed by the remaining un-ablated surface. This could be countered by targeting a large area around the rib. While the FIB is an ideal solution to creating good quality facets, individually targeting the facet of every waveguide is not a suitable choice when batch producing many ribs.

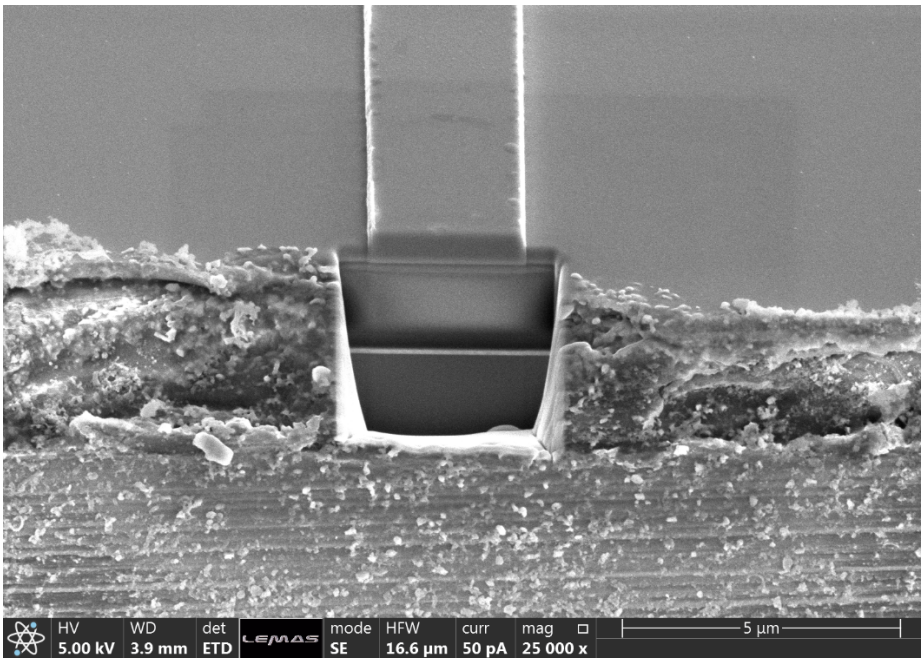

Figure 4.25: An SEM photo of the side of a sample with LN ribs milled which has had FIB work performed on it. The ion beam ablates the sample in a small area at the end of the rib, creating a smooth surface for optical work. Image courtesy of John Harrington.

4.3.3 Polishing

Mechanical polishing the side of a substrate is an alternative way to get smooth surfaces. LN has a hardness of 630±30 kg/mm^2 on the Vickers scale [163], which equates to around five on the Mohs scale, a system which measures from one to ten.

Polishing was done by hand using diamond polishing paper. The sample was mounted in a custom designed brass jig. The jig is a solid block with a 90° cut out in the middle, seen in Figure 4.26. Mounting was done by gently heating up the brass jig with a piece of wax on it, placing the substrate onto the jig, and applying light pressure to hold the substrate on while the wax cools and sets. The sample must be protruding from the jig edge, otherwise excessive polishing of the jig would need to be performed before reaching the sample. Due to the time it takes for the jig to heat up, placing the LN sample on the jig at the start of heating avoids any charging effects. Pressure must be applied to ensure sufficient adhesion of the sample, in order for it not to detach during the polishing process. Care must be taken not to damage the ridges when applying pressure. Pushing wax against the sides of the substrate provides additional adhesion. Additional wax is melted on top of the sample in order to cover and

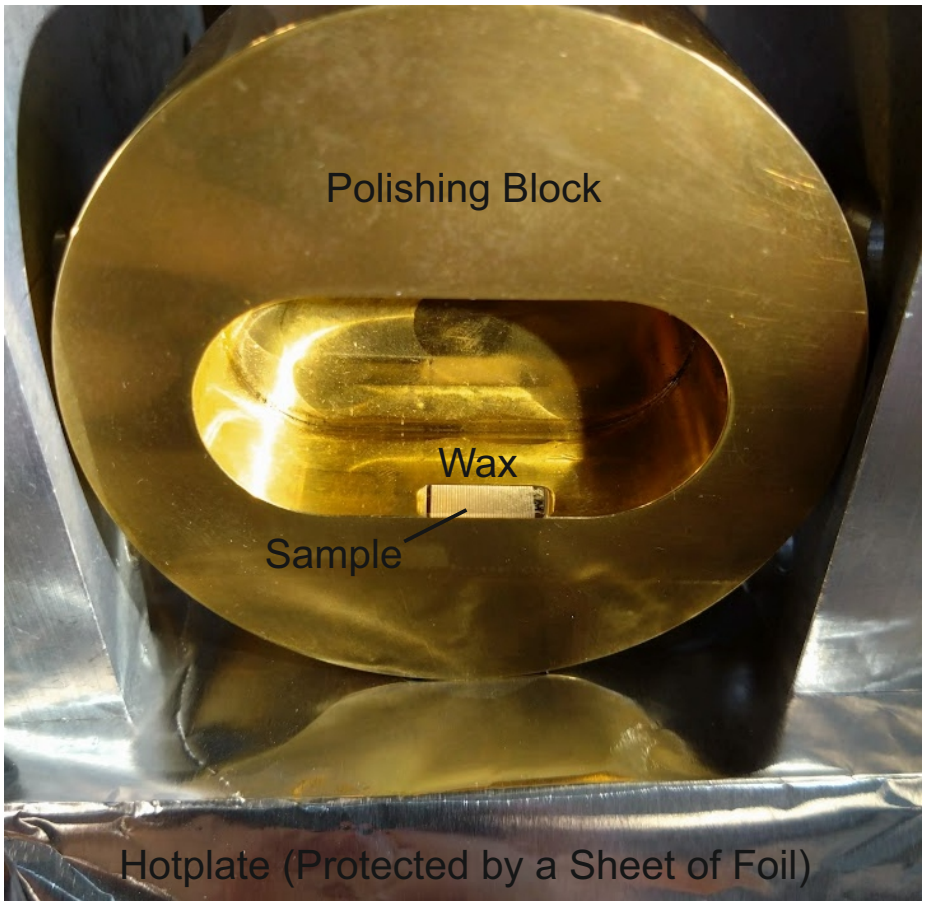

Figure 4.26: An optical photograph displaying the polishing block with a sample mounted, using colourless wax to hold it in place. The sample is sticking just over the edge of the front face of the jig to ensure contact with the polishing paper.

protect the top surface from the inorganic polishing residue, which is difficult to remove. A mounted sample is seen in Figure 4.26.

The polishing block was then applied to diamond polishing paper. 30 µm grit paper was used to begin with, working down the grits to a minimum of 0.2 µm grit paper. A sample polished to a 0.2 µm grit is seen at 4x zoom in Figure 4.27, and 100x zoom in Figure 4.28. Polishing was performed with lubrication from de-ionised water. Care must be taken when the jig is first applied to the polishing paper, as the sample edges at this point are unsupported, leaving them vulnerable to damage from the abrasion. The polishing progress was viewed under an optical microscope, with care taken to look for any deep scratches before moving onto the next grit size.

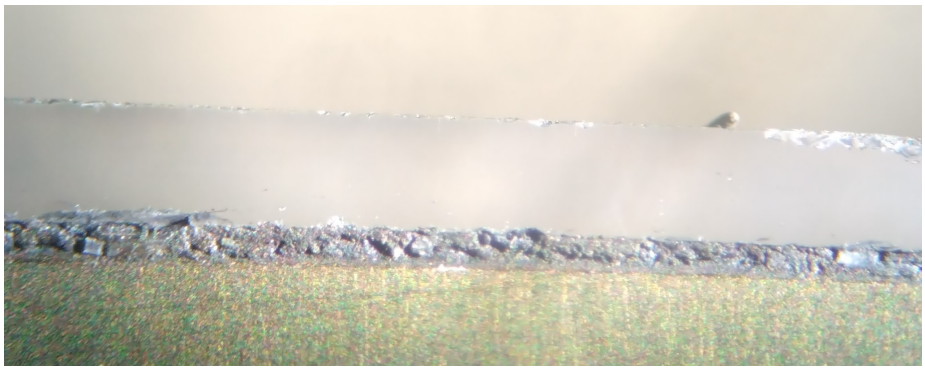

Figure 4.27: An image through a microscope at 4x magnification after a sample of pure LN has been polished using a 0.2 µm grit diamond paper. The LN is shiny and appears scratchless.

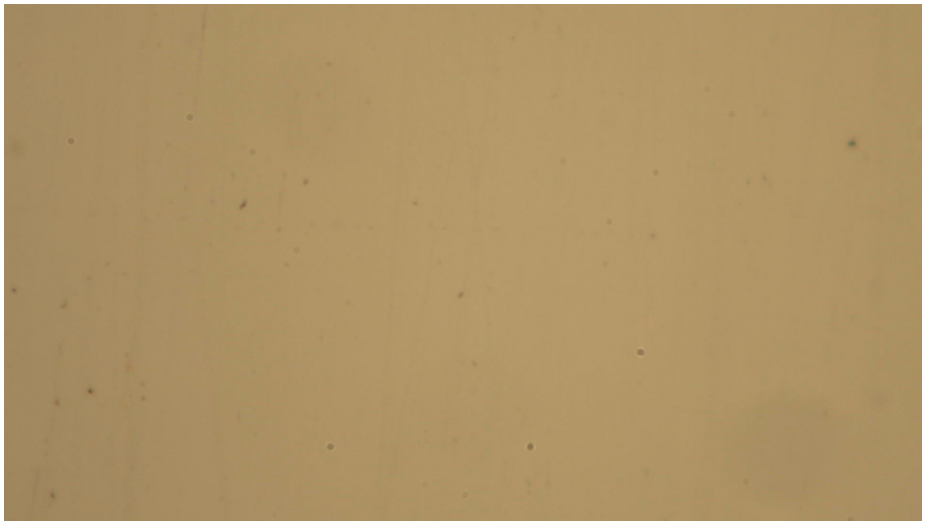

Figure 4.28: The sample in Figure 4.27 when viewed by a microscope at 100x magnification. The high magnification of the surface shows only very faint scratches.

Once polished, the sample was removed from the brass block by gently heating it to melt the wax. The sample was then either rotated and remounted to polish the other side of the waveguide, or cleaned of wax. Care was taken to protect the previously polished side from any polishing residue. When remounting the sample, wax was placed over the already polished side to protect it. When removing the sample, it is cleaned in trichloroethylene. Care was also taken to remove the wax from the sample in a way which does not compromise it by letting the inorganic polishing residue attach to the sample. A small amount of

residue can sometimes be cleaned away using an ultrasonic bath.

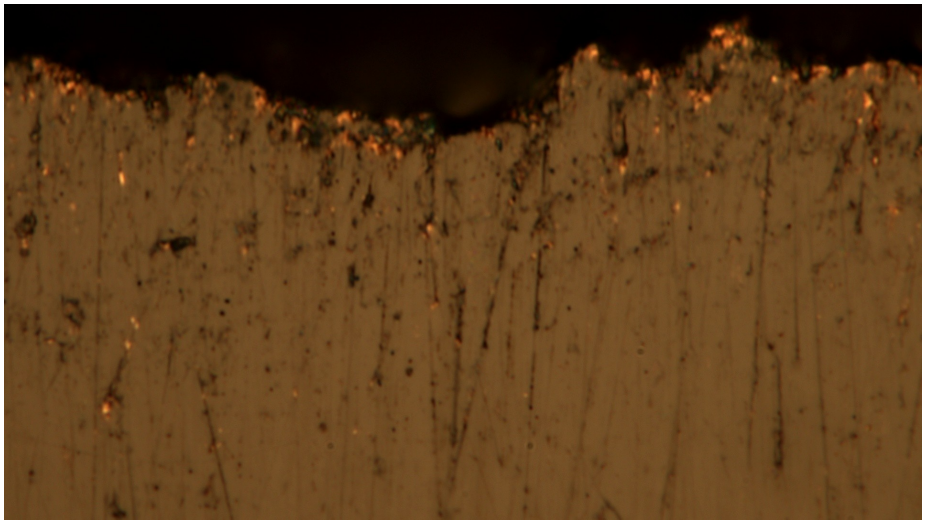

Figure 4.29: A microscope image of a 30 µm grit polished sample, displaying that there is little gold left, and that the remaining gold from the chipped edge of the substrate has smeared down the polished face. The smeared gold could cover a waveguide facet, while the greatly chipped unsupported surface shows that a thin film sample will not survive the polishing procedure.

Polishing has the advantages of being much more batch friendly than using FIB, as many ribs can be placed on a single sample. However, the abrasiveness of the technique can cause issues, such as damaging the sample edges when protruding from the jig, seen in Figure 4.29, as well as the potential for scratches from dirt caught in the polishing process. Further polishing is not a suitable resolution to the damaged substrate edges, as the sample top face is still unsupported using this polishing block. A potential solution to this would be to attach a piece of spare wafer to the top of the sample to protect it, done by melting wax between the two wafers and compressing them to micron thicknesses. The material composition of the sample must be considered as well, as a sample from Wafer 1 with the gold layer smeared due to gold softness, seen in Figure 4.29. This and polishing residue can end up covering the waveguide facets.

If the sample edge issue is resolved, the results of good polishing may be better than FIB, as the indentation of the facet from the sample edge, shown in Figure 4.25, is not present with polishing. This allows an optical fibre to be placed closer to the sample edge, potentially leading to improved coupling.

A possible redesign of the polishing block may assist in future use, by making the cutout run all the way through the jig so that the sample can be slid down flat against the edge of the polishing block, meaning that rather than sitting proud, the sample can be polished with its surfaces supported to reduce chipping.

Another useful modification would be the addition of a spring in order to gently press the sample against the jig while the wax is melting to promote adhesion rather than requiring external sources. A different option is to formulate a mount for use on a lapping station. This would allow for a finer polish, as the grit size goes down to 50 nm, a quarter of the lowest grit polishing paper. No means of doing this on the UoL lapping station currently exist due to requiring the side of the samples to be polished, rather than the top or bottom surfaces as is conventional.

4.4 Benzocyclobutane Processing

This sections outlines the work done on BCB as a dielectric layer for matching the waveguide, and increasing its overall size for coupling ease. The key focuses are:

- BCB Thickness
- BCB Refractive Index
- BCB Adhesion

4.4.1 BCB Thickness

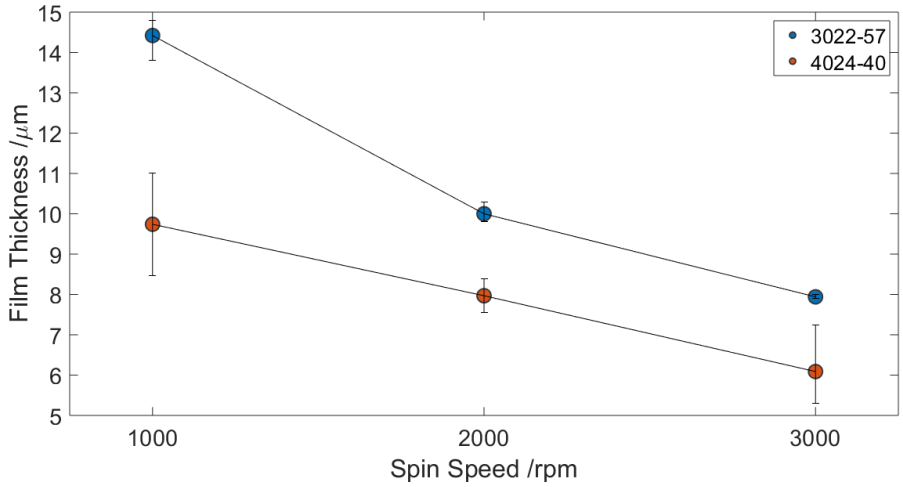

Figure 4.30: Spin curves for two types of BCB, 3022-57 and 4024-40, made using the UoL spinner. The 4024-40 film thicknesses were measured via surface profiler, while the 3022-57 film thickness was measured by reflectometer. Data points show the thickness averages, while the error bars show the maximum and minimum thicknesses observed.

BCB is an essential part of the proposed waveguide. The deposited thickness of the substance is the easiest way to match the NIR and THz waveguides. Therefore, knowing the film thickness which has been deposited on the sample is critical. Deposition is done via spinner, followed by a one minute bake at 100°C. The spin process includes a 5 second step of spinning at 750 rpm to spread out the viscous material, before speeding up to the desired spin speed for 30 seconds to create the layer. The bake drives out the solvent from the solution. A spin curve for two different types of BCB is shown in Figure 4.30. The BCB in this data has not been cured. Cyclotene 4024-40, a branded form of BCB, was initially used for these experiments. After tests showing poor lithographic qualities, a new form of BCB was acquired, 3022-57. This film spins thicker, at the expense of not being photosensitive. 3022-57 is the form of BCB used in the experiments shown in this research following the spin curve data.

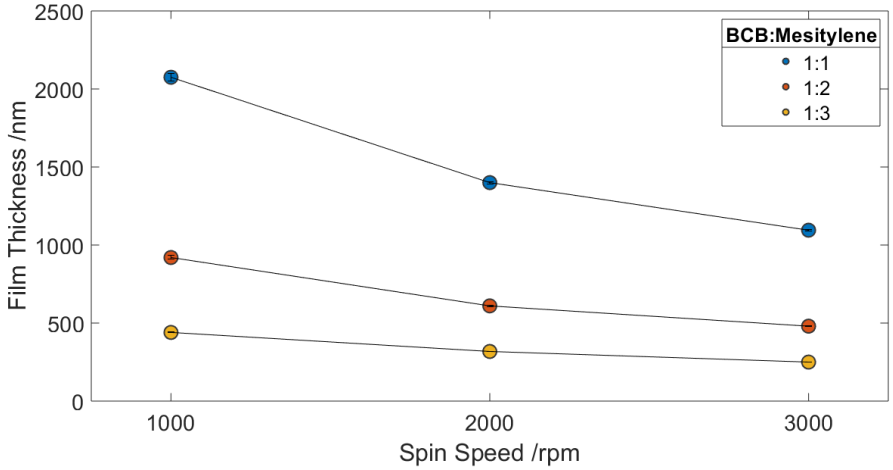

Figure 4.31: Spin curves for cyclotene 3022-57 mixed with mesitylene in varying concentrations. The film thickness were measured by reflectometer. Data kindly provided by Connor Kidd.

The spin curve data obtained for the 4024-40 variety of BCB was obtained by scratching through the film, and measuring the depth of change using a surface profiler. The 3022-57 was measured using reflectometry, which has only more recently become available at UoL. This method was more accurate, seen by the error bars for the 3022-57 in Figure 4.30. The error bars measured with reflectometry become smaller with increasing spin speed. This is expected as the film becomes more uniform from the higher spin speeds.

BCB may be diluted using mesitylene in order to thin the solution. This results in lower layer thicknesses, as seen in Figure 4.31.

When using undiluted BCB, substrates larger than the size of a waveguide sample must be used to avoid problems associated with large edge beads, fol-

lowed by dicing the substrate into the appropriate sample size. The spin time must also incorporate a period of spinning at a slow speed, 750 rpm for 5 seconds, to spread out the material, before spinning at the appropriate speed for the desired thickness [164]. Multiple layers of BCB can be spun on top of each other to increase the thickness of the layer, which may be essential for creating a layer of the correct thickness for index matching. It is important when spinning multiple layers to include a 'soft' cure for the intermediary layers; this is done in a vacuum oven at 210°C for 40 minutes. The soft cure is to ensure any remaining solvent in the film is driven off. A soft cure improves adhesion between polymer layers [164]. After the final layer was spun, the BCB was fully cured in the vacuum oven at 250°C for one hour. The final cure hardens the film to make it durable and difficult to remove.

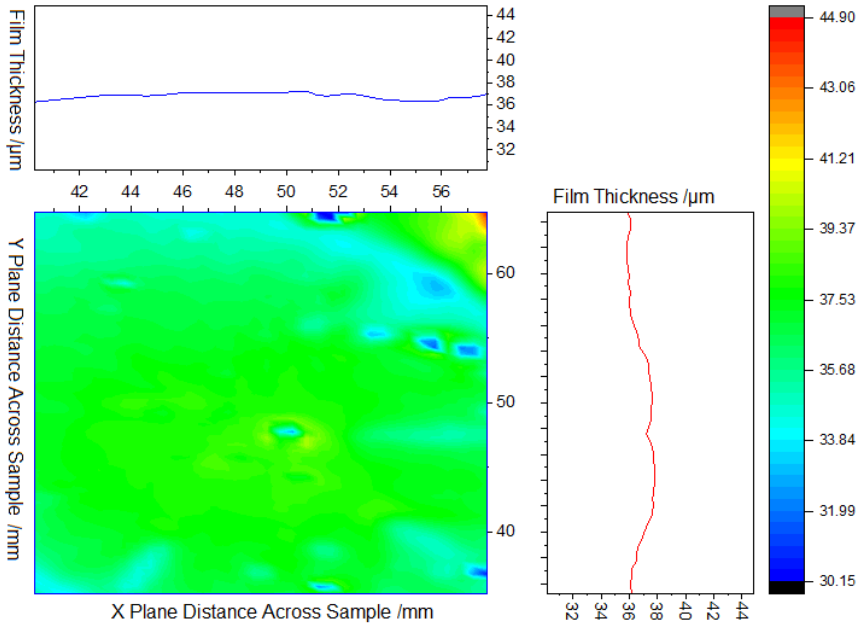

Figure 4.32: A colour map built up using a reflectometer indicating the thickness of the BCB film over an area of a substrate. The colour map displays 'warmer' colours at higher film thicknesses. The map is surrounded by plots in the x and y axes displaying the average film height in micrometres along the axis.

Figure 4.32 shows the results of spinning six layers at 3000 rpm, with soft cures between spins. The thickness was measured by reflectometer. Figure 4.33 displays a three dimensional map of this data. The large defect in the middle of the surface is thought to be caused by a bubble in the resist when the spin process began, which are difficult to remove from the viscous substance. The overall average of the film shown is 36.6 µm, while the average thickness varies by less than 2 µm. The stacked layers have started to cause a dome effect, where

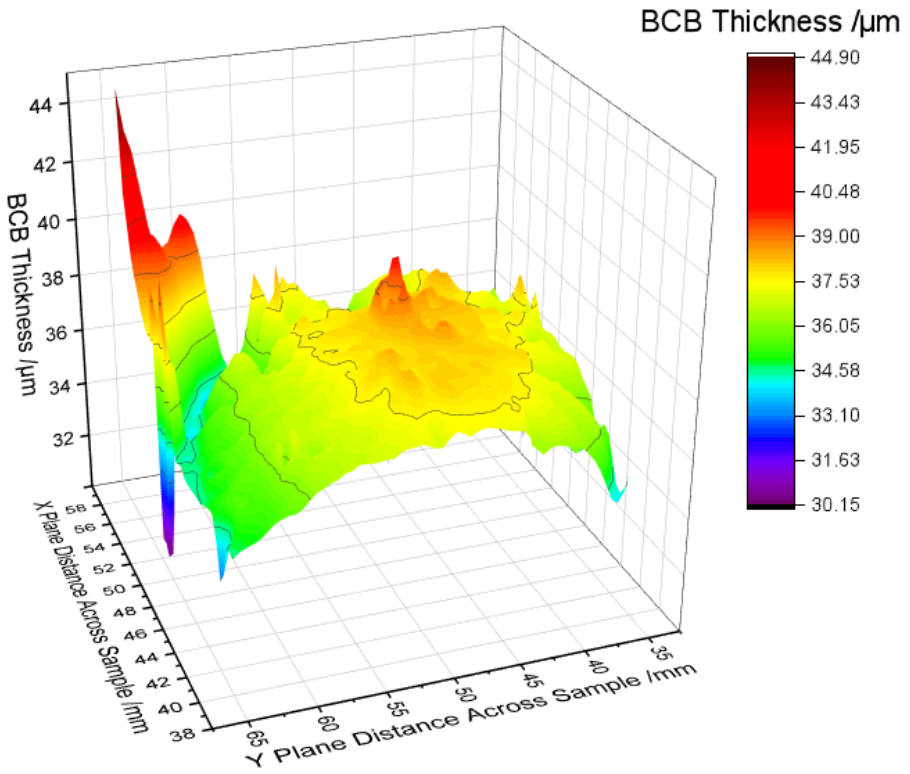

Figure 4.33: A three dimensional interpretation of the data provided in Figure 4.32.

the middle of the sample is highest, and the thickness decreases as the distance from the centre increases. The peak value in the corner of the measured area is the edge bead.

It is likely that spinning many layers at high speeds provides a better film surface conformity than fewer layers at low speeds, due to the doming effect caused by the viscosity. However, this leads to an increased chance of defects caused by dirt and bubbles to occur over the repeated spin process.

4.4.2 BCB Refractive Index

There is a lack of published refractive index data for BCB in the THz region.

This was an important input parameter for the simulations described in Chapter 3. One source provides an index of 1.65 at 0.4 THz [120], while another states 1.57 at 3 THz [165]. TDS of a BCB film was done to ascertain the index value experimentally.

Two samples of Si were taken, both from the same wafer. One was set aside to be used as a reference sample. The other was the BCB sample from

Section 4.4.1, with multiple layers of BCB spun on it. This layer needed to be thick, in order to detect phase change in the TDS system. It also needed to be a known value for an accurate index calculation. The variation of thicker films due to the high viscosity highlights the complexity of accurately determining the index value. The mapping of the film, shown in Figure 4.32 and Figure 4.33, was used to determine the value of thickness to use across the sample. Code, kindly provided by Dr. J. Freeman, was used to solve the full transfer function to calculate the value of refractive index across a THz frequency range. The index was calculated at several points along the substrate. The average of the results is displayed in Figure 4.34.

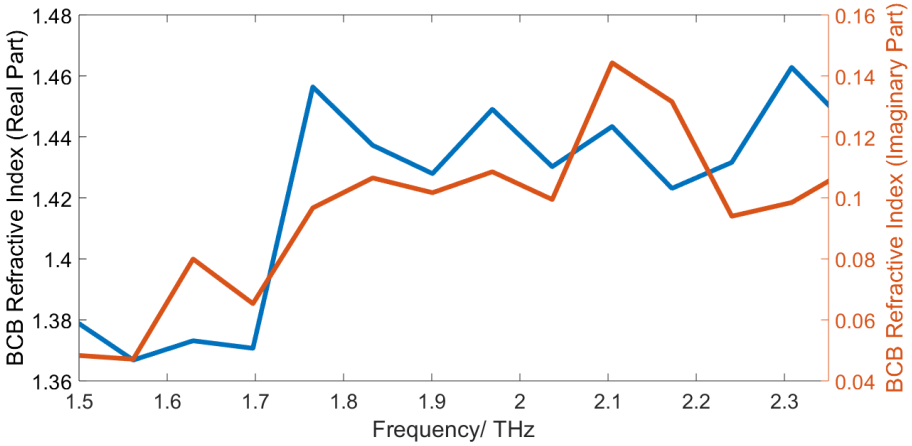

Figure 4.34: A plot of the real and imaginary parts of the refractive index of BCB against THz frequency. This plot was made using the transmission data provided by putting the BCB sample in the TDS system. Data was taken at 22 points along the BCB sample, moved across in 0.5 mm increments, and then averaged.

The trend in real index value over the frequency range displayed in Figure 4.34 is shown to be rather settled. This correlates with other work which shows a settled frequency dependence for a doped sample, of approximately 30% with $BaTiO_3$ powder [120]. A recent paper, published within the time frame of this research, has stated that the index is 1.57 at 3 THz [165]. While not reaching up to this frequency, the data shown in Figure 4.34 is not far off the value of 1.57 and can reasonably be expected to be at such a value at 3 THz.

The imaginary index is shown to be low, not rising above 0.15. This shows the material can be considered a low loss dielectric at THz frequencies.

Data from the 0 to 1.5 THz range is not displayed in Figure 4.34 due to the difficulty in measuring very thin dielectric films using THz. This difficulty leads the data in this range to appear unreliable and there is some scatter in the data.

In the NIR regime, the index of BCB was measured experimentally at 1550 nm as 1.55 using ellipsometry, with a negligable loss component. This

value is close to the value in a paper which reported the index value of BCB at 1536 nm as 1.54 [166].

4.4.3 BCB Adhesion

It is advised that BCB is spun on using a primer, AP3000, for most surfaces. This provides a notable improvement in the adhesion to most metals, such as copper and titanium. BCB sticks to a surface well when the saline in the BCB has oxygen to bond with. Gold, for example, does not form a surface oxide, and consequently BCB forms a poor contact with the metal. This can be remedied by using an intermediate layer. Two tests were used to check this; a tape test, and scribing. The tape test involves using a piece of sticky tape, attaching it to the sample surface, and checking if the layer survives the removal of the tape. Scribing induces compressive and tensive forces through the BCB layer, which can cause issues at material interfaces. A few nanometres of titanium, which can much more readily be oxidised, between the gold and BCB was found to improve the adhesion greatly.

4.5 Fabrication Summary

From the initial investigation into fabrication options, physical milling has shown the best results in other waveguides and so has been chosen for this research. E-Beam lithography has been shown to provide the best quality mask, with resist being the optimal material after comparison to chrome and oxide masks. An analysis of the ion milling etch has been performed with an angle dependence, and an angle of around 50° has been shown to provide smooth and near vertical sidewalls. The current results of this work are best seen in Figure 4.19, showcasing a distinct and uniform rib. Further work is possible in experimenting with the use of shallower angled etches to smooth existing sidewalls. An analysis on facet creation has shown that FIB work provides the highest quality facets.

27 test ribs have been fabricated on substrate 1 from Wafer 1, which are characterised in Chapter 5. These ribs were etched at 85° (5° from the beam normal to the substrate surface). After a ten minute etch, the resulting rib height was 113 nm. The facets have been created using the FIB technique. There is scope for further optimisation of the fabrication steps for future samples, as the mask for these ribs during the lithography was overdosed, and the milling process did not incorporate a smoothing step at a shallower angle to tidy up the sidewalls.

Building upon the work discussed within this chapter, further fabrication was performed for the samples used in Chapter 6. The processing for these specific samples is discussed within that chapter, in Section 6.2.

Chapter 5

Near Infra-Red Characterisation

27 LN test ribs were obtained from the fabrication processes discussed in Chapter 4. These test ribs were obtained from Wafer 1. A summary of the ribs can be seen in Table 5.1. NIR characterisation of these test ribs is described in this chapter. The chapter sections are outlined below:

- Lithium Niobate Waveguides for Testing
- Waveguide Transmission Testing
- Waveguide Efficiency
- Polarisation
- Fabry-Pérot Resonances

5.1 Lithium Niobate Waveguides for Testing

Three identical samples, labelled A, B, and C, were cut from substrate 1 in Section 4.2.2.3, each with nine ribs, labelled 1-9. The rib design is shown in Figure 4.4. The facets were formed via the FIB process, discussed in Section 4.3.2. Figure 4.25 shows a facet of one of the ribs on sample A.

The nine ribs on each sample consist of 3, 4, and 5 mm lengths at 2.0, 2.3 or 2.6 µm widths. Figure 5.1 shows an annotated sample, labelling the ribs. A table summarising all of the test ribs is provided in Table 5.1.

The ribs are designed so that the facets of each ridge are the same height and width apart, despite altering the length. This allows for ease of alignment and for ribs of different lengths to be on the same substrate. The bends allow for testing of propagation losses, and are not intended to be included in the finished device. The bend radius used to implement this is 100 µm, which is larger than the reported radius at which bend loss becomes negligible in comparable

structures [48]. Keeping the bend radius the same between ribs means the ribs can be fairly compared.

The purpose of these ribs is to establish the amount of loss generated as a NIR signal traverses a rib, to establish the quality of the fabrication work and experimentally see which rib width works best.

Figure 5.1 shows sample A. It has been mounted on a copper block by General Electric (GE) varnish for ease of handling. The LN substrate is thicker than the diameter of an optical fibre, so a fibre can align to the sample facet over the top of the copper block. The sample is at the edge of the copper block so that a lens can be used for coupling to the other side.

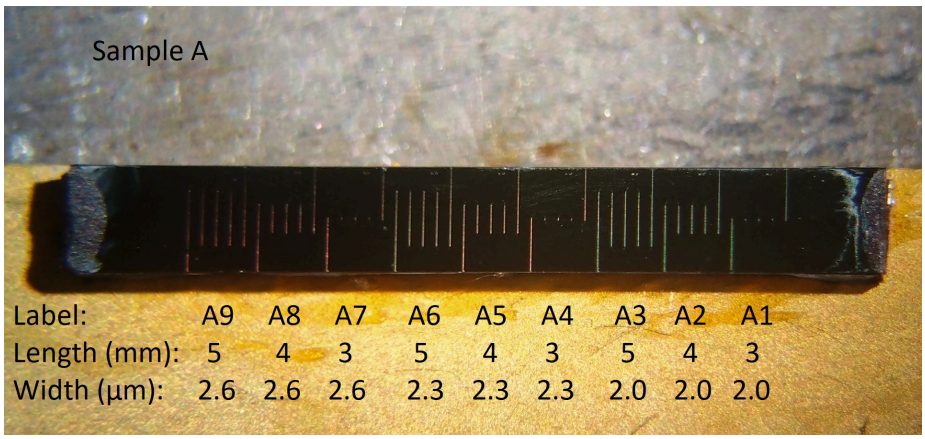

Figure 5.1: A photo of Sample A, one of three identical test substrates with ridges on, as viewed through a microscope. The substrate is mounted on a copper block, attached using GE varnish. On the substrate are ribs of three, four and five millimetre length at 2.0 µm width, adjacent to sets of ribs the same lengths at 2.3 and 2.6 µm width. The left and right ends of the sample have a residue on them from mounting in the FIB.

5.2 Waveguide Transmission Testing

A testing system was established to characterise the ribs, a diagram of which is given in Figure 5.2.

A tunable frequency NIR laser by Santec, operating around 1550 nm, acted as the input to the system. This was connected to a single mode optical fibre, which passed through polarisation paddles before pointing directly at the sample facet. Free space coupling to the sample was implemented, with the alignment of the fibre to the facet critical to the coupling quality. Initially, standard fibres were used. This was then changed to a Polarisation Maintaining (PM) tapered fibre. The PM fibre allowed an experimental polarisation analysis of the sample to be performed, while the tapered fibre end reduced the spot size of the emitted

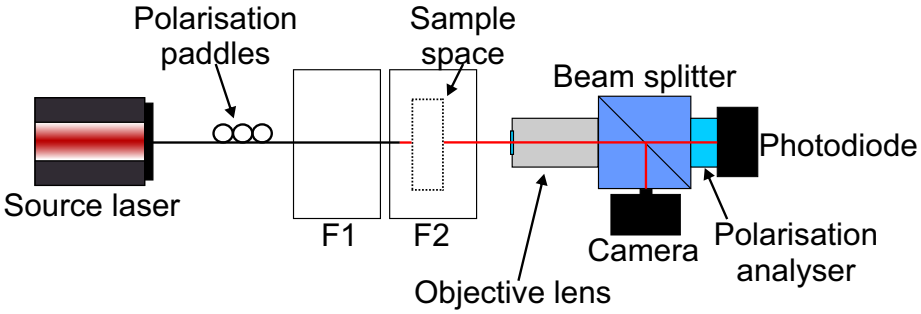

Figure 5.2: A system diagram displaying how the ridges were characterised. Black lines are fibre connections and red lines are free space connections. There are two stages, capable of three dimensional movement, labelled F1 and F2. The fibre end is mounted on F1, while the sample space (dotted outline area) is on F2. The objective lens collects the light from the sample space and passes it into the connected beam splitter. The PD connects to recording equipment.

beam onto the facet, improving coupling into to the small facet. The tapered fibres, TPMJ-3A-1550-8/125-1-10-2.5-14-1-AR, were obtained from OZ Optics. They feature a 2.5±0.5 µm spot diameter and anti-reflection coating on the tip. The fibre and sample are mounted on independently moving flextures, provided by ThorLabs. In order to align the fibre and the sample optimally, a microscope is placed above the flextures, used only when the laser is off.

The transmitted light is collected in an Olympus objective lens. This lens passes the light to both an optical camera and a PD connected via a beam splitter, all from ThorLabs. A screenshot of light seen through a rib on the camera is displayed in Figure 5.3. The PD has an adjustable gain, and is electrically connected to a Keysight voltmeter for data acquisition. Due to the output collecting equipment being fixed in space, it is easiest to align the output facet to the objective lens using the IR camera to start, before aligning the input fibre to the front facet. A separate measurement was also performed to identify where on the camera display the PD reading was highest, which was marked using a yellow ring, shown in Figure 5.3. Changing the laser from 1550 nm to a 780 nm laser allowed a more sensitive camera to be used for initial alignment, before changing back for the experiment. Due to the light scatter over the top of the ribs, a pinhole was placed in front of the PD to minimise the detection of the scatter. A polarisation analyser was also installed before the PD for the polarisation experiments.

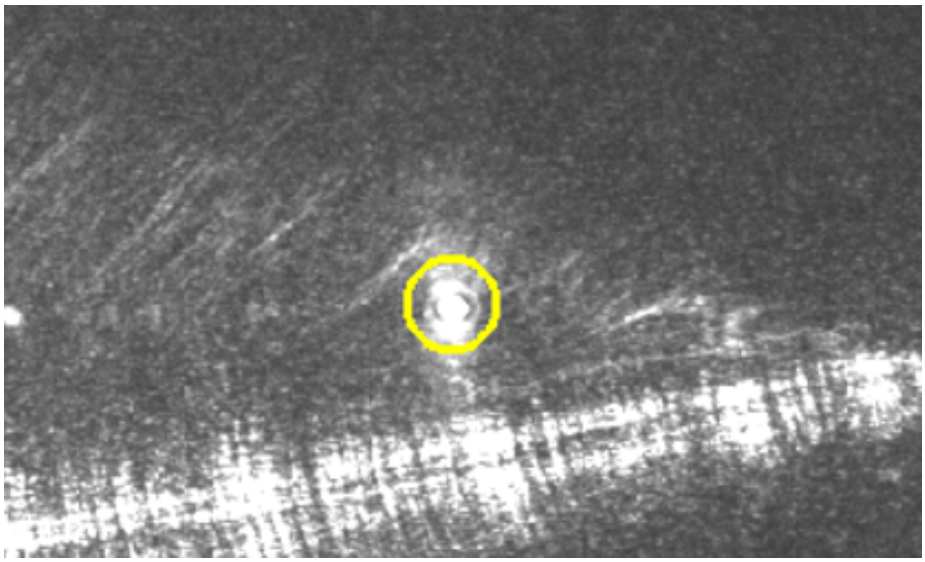

Figure 5.3: A screenshot of the display from the optical camera where light can be seen emitted from rib B7, highlighted using a yellow ring. Noticeable scatter is present around it from the optical fibre, despite the fibre being horizontally displaced.

5.3 Waveguide Efficiency

The following experiments in this section were done with a single mode fibre and no polarisation analyser. The polarisation paddles were used to acquire optimum transmission through the ribs.

These experiments were performed to ascertain the losses through the fabricated ribs. These losses would provide an idea of efficiency, and could be broken down into coupling and absorption losses. An indication of which areas need improvement for further ribs could then be obtained from this information.

There were noticeable changes in performance between theoretically identical ribs. Some ribs were damaged, a sample of which is shown in Figure 5.4. These photos show that the yield variation comes from the fabrication level, during the photolithography. The mask was not as well defined as desired. This was probably caused by the charging issues of the LN, which resulted in dirt sticking vigorously to the substrates. Bubbles in the resist may also have caused some issues. A signal was seen at the end of ribs C5 and C7, the ribs shown in Figure 5.4, indicating that minor manufacturing errors can be overcome. Ribs B1 through to B4 were destroyed through a handling error.

For some ribs, the scatter of light over the top of the ribs was so high that the emission from the rib was obscured on the camera display. For these points, the highest PD reading was taken, as the PD was highly sensitive, and then it could be assessed if these points were signal or on the noise floor. This would

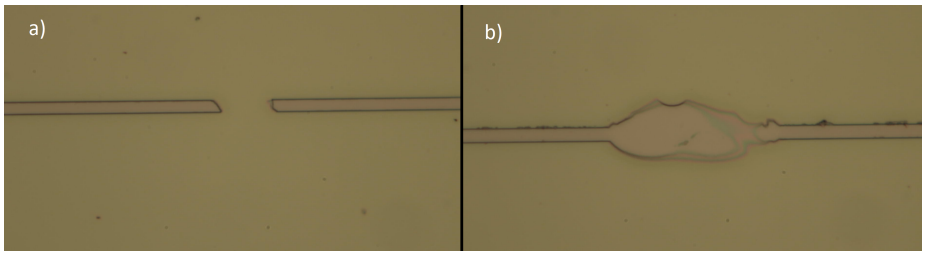

Figure 5.4: Images taken using a microscope of defects in the ribs tested in this section. a) shows a break in rib C5, while b) shows a defect in rib C7, of a section of the rib which is much larger than intended and not all the same height. Despite the defects, these ribs still produced detectable signals at the end facets. Photos courtesy by Yifan Weng.

not be an issue with the proposed waveguide, due to the cladding layers above the LN rib which would block the light from scattering over the top.

The efficiency of the ribs is analysed in the plots below. The efficiency is defined as the signal on the PD with the ribs present, divided by the PD signal with nothing in the sample space and the lensed fibre displaced to get maximum coupling into the lens. Total efficiency therefore includes both coupling and transmission losses.

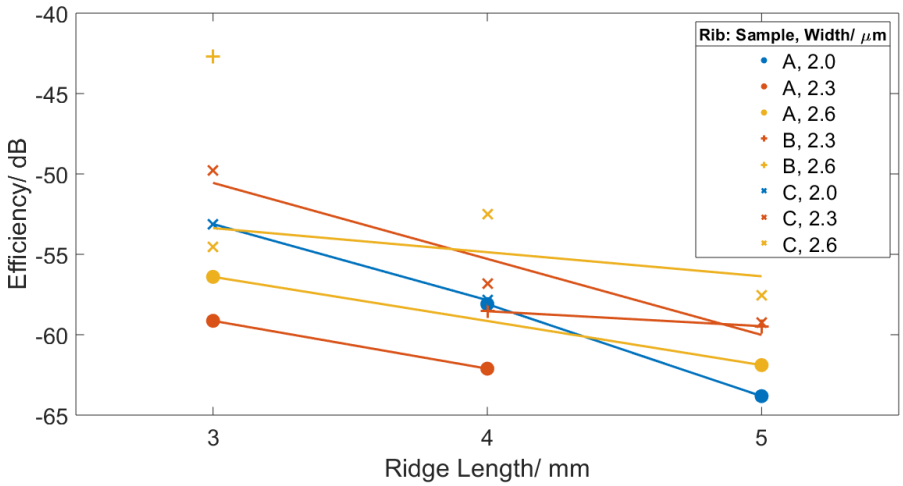

Figure 5.5: The plot of Table 5.1 with the points less efficient than -65 dB removed, due to the likelihood of them being caused by scatter rather than signal. The lines of best fit have been updated. These can now be used to more accurately calculate the propagation and coupling losses.

Table 5.1 shows the total efficiency of the ribs. As expected, the signal shows a trend of dropping as the ribs become longer, due to experiencing additional

Test Rib Summary			
Name	Width /µm	Length /mm	Total Loss in dB/Condition
A1	2.0	3	69.9
A2	2.0	4	58.1
A3	2.0	5	63.8
A4	2.3	3	59.1
A5	2.3	4	62.1
A6	2.3	5	67.6
A7	2.6	3	56.4
A8	2.6	4	69.7
A9	2.6	5	61.9
B1	2.0	3	Broken
B2	2.0	4	Broken
B3	2.0	5	Broken
B4	2.3	3	Broken
B5	2.3	4	58.5
B6	2.3	5	59.5
B7	2.6	3	42.7
B8	2.6	4	66.6
B9	2.6	5	66.8
C1	2.0	3	53.1
C2	2.0	4	57.9
C3	2.0	5	70.3
C4	2.3	3	49.8
C5	2.3	4	56.8
C6	2.3	5	59.2
C7	2.6	3	54.5
C8	2.6	4	52.5
C9	2.6	5	57.5

Table 5.1: A table summarising the test ribs evaluated in Chapter 5.

absorption from the extra length. The effects of width are harder to ascertain. The loss values also help determine which of the points may be scatter rather than signal.

Figure 5.5 is a plot with those data points likely to be scatter removed. The data points suspected of being scatter readings were those with efficiencies of less than -65 dB, as they were observed as being close to or on the noise floor. In some cases, such as for ribs A1-3, removing the scatter data points has provided the lines of best fit more reasonable looking gradients than when plotted with all data points.

By taking the lines of best fit from Figure 5.5, the loss from the ribs can be broken down into their constituent parts of absorption and coupling losses. This is done using the Beer-Lambert law. Taking the Beer-Lambert law in base 10:

$$I_{out} = I_{in}\beta_c\beta_c 10^{\frac{-\alpha L}{10}} \tag{5.1}$$

where β_c is coupling at each facet, α is loss in dB/mm, and L is length in metres. Base 10 is used for compatibility with decibel units. Taking $\log_{10}$ of each side:

$$10log_{10}\frac{I_{out}}{I_{in}} = 20log_{10}\beta_c - \alpha L \tag{5.2}$$

By plotting on dB scale, and then fitting a straight line [167];

- Intercept = $20log_{10}\beta_c = 2\gamma_c$, where γ_c is coupling loss per facet in dB
- Gradient = α, which is transmission loss in dB/mm

Knowing the best fit line gradients are equal to transmission losses and examining the data sets seen in Figure 5.5, the data sets agree well. The blue best fit lines, for ribs 2 µm wide, almost form a continuous straight line. The pair of yellow best fit lines are close to parallel, as are two of the three orange best fit lines. This shows, once outliers are excluded, that the fabrication quality between the ribs is fairly consistent, and that the major variable in rib loss is the coupling quality provided by the facets, which adjusts the y axis intercepts of the best fit lines. The erroneous data points are likely to be caused by major ridge defects during photolithography.

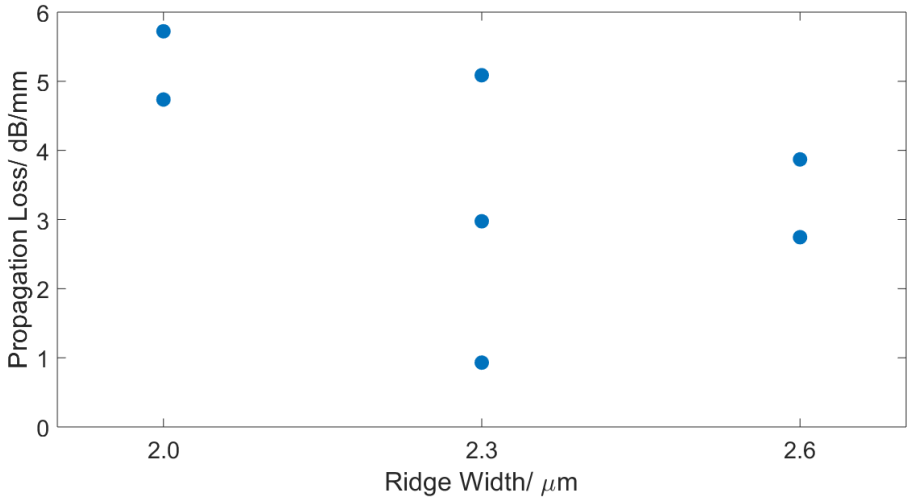

Figure 5.6: A plot using the gradients of the lines of best fit in Figure 5.5 to determine the propagation losses. The thinner ribs show a higher propagation loss.

From the lines of best fit, the absorption losses are shown in Figure 5.6, and the coupling losses are shown in Figure 5.7.

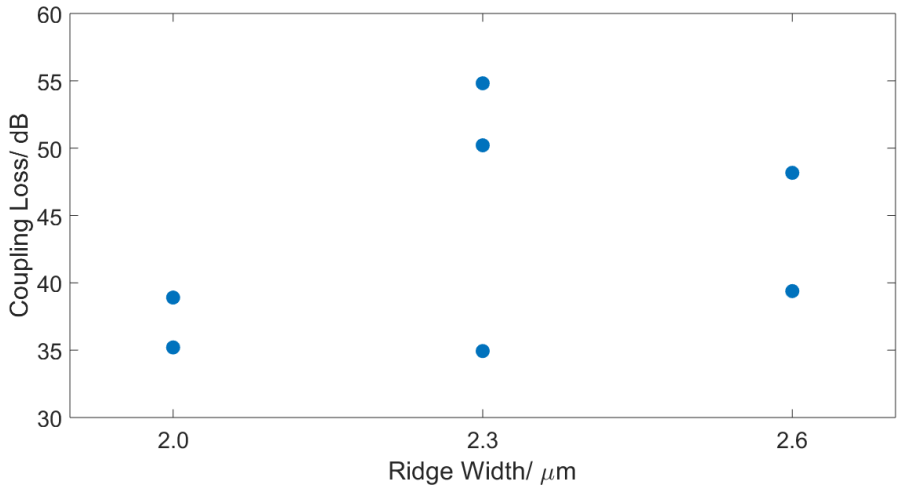

Figure 5.7: A plot using the y-intercepts of the lines of best fit in Figure 5.5 to determine the coupling losses. The values given here for each rib width include the coupling from both the input and output facets.

State-of-the-art LN ribs demonstrate a propagation loss of 0.268 dB/cm at 1550 nm [74]. Using the Beer-Lambert law in its exponential form, as shown in Equation (3.7), the loss coefficient can be calculated from the loss per unit length. Propagation losses of the test ribs from Figure 5.6 are between 1 and 6 dB/mm, and translate to a loss coefficient of between 2.30 and 13.8 cm^{-1}. This is much larger than the value of around 0.007 cm^{-1} seen from similar high quality LN ribs [53,74], showing there is much scope for improvement in the rib fabrication.

An edited version of Figure 3.26 is presented in Figure 5.8, using the loss coefficients of the measured test ribs to simulate an estimated amount of THz generated assuming perfect phase matching. It can be seen that even the highest loss coefficient of the fabricated test ribs will allow THz generation. However, at either end of the range of measured loss coefficients, there is a large contrast between the usable rib length, and between the amount of THz generation along that length, demonstrating the difference provided by having a loss coefficient at the lower end of the range. It is important to have low NIR absorption within the waveguide, in order to maintain a high NIR intensity for efficient conversion into THz. It is not, however, expected for the pump beams to be entirely used up in the conversion, or fully attenuated, and so it is expected for there to be NIR emission at the end of the proposed device. This extra emission would be ignored, taking only the THz emission.

A wider rib is shown by the data trend in Figure 5.6 to have less loss. This will be due to a lower sidewall interaction. As described previously however, this will come at the expense of having less mode confinement, so it is a trade-off. A wider rib has a slightly larger area to collect more light at the input facet,

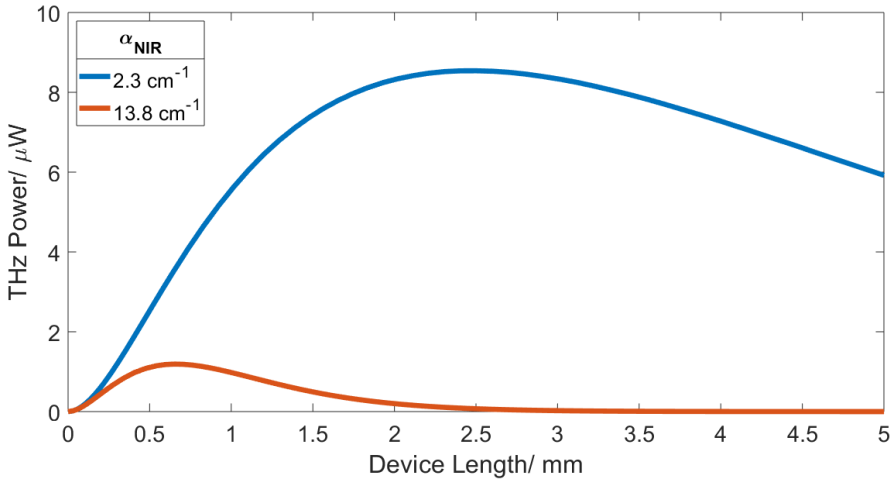

Figure 5.8: A plot displaying how much THz can be generated using the NIR loss coefficients measured using the test ribs.

but should not have a significant influence on coupling losses.

Comparing Figure 5.7 to Figure 5.6 shows that the coupling loss is much greater that the propagation loss from the waveguide itself. The propagation loss is around three to five dB/mm whilst the coupling is around 40 to 47 dB of loss. However, this value is for total coupling loss; there are two facets on each rib, which means there is roughly 22 dB of loss at each end when coupling both in and out, assuming an even distribution.

The coupling losses of between 35 and 55 dB leave room for improvement. High quality LN ribs have been stated to have coupling losses of 10 dB per facet [53]. Since these initial test ribs were characterised, promising work has started, focusing on reducing the coupling losses by improving the FIB operation. One method is by depositing a layer of SiO_2 before the FIB work in order to provide some protection to facet.

5.4 Fabry-Pérot Resonances

Fabry-Pérot resonance fringes provide an indication of the quality of the waveguide. They can be seen when sweeping the frequency through the ribs. It is a way to measure the quality of a cavity without requiring knowledge about the coupling losses [168].

In an optical cavity, light can circulate between the two end facets. When there is an integer number of half wavelengths through the length of the cavity, resonances form. This waveguide is a specific kind of optical cavity, called a Fabry-Pérot interferometer or Fabry-Pérot resonator. By looking at these resonances, the Free Spectral Range (FSR) can be determined, which is the

period in wavelength between the resonances. By taking the Full Width at Half Maximum (FWHM) of a resonance, the finesse of the rib can be calculated, using Equation (5.3) [169]. Finesse is a measure of how sharp the resonances are, where sharp resonances indicate a good quality resonator.

$$Finesse = \frac{FSR}{FWHM} = \frac{\pi}{\alpha l - \ln R} \tag{5.3}$$

where α is absorption coefficient in m^{-1}, l is the waveguide length in metres, and R is the reflectivity of the facets. The reflectivity is a fraction representing the proportion of light which is reflected back into the system when reaching a facet.

Rib B7 was used in the sample space. It was aligned using the method in Section 5.2. Once a signal was seen on the PD, the voltmeter it output to was replaced with an oscilloscope for data acquisition, which was also electronically connected to the source laser for a trigger signal. A wavelength range of 1545 to 1555 nm was scanned across for both rib B7 and when aligned directly to the PD with no rib, at a rate of 5 nanometres per second. 64 averages of the reading were taken, with each scan acquiring 5,000 samples per second.

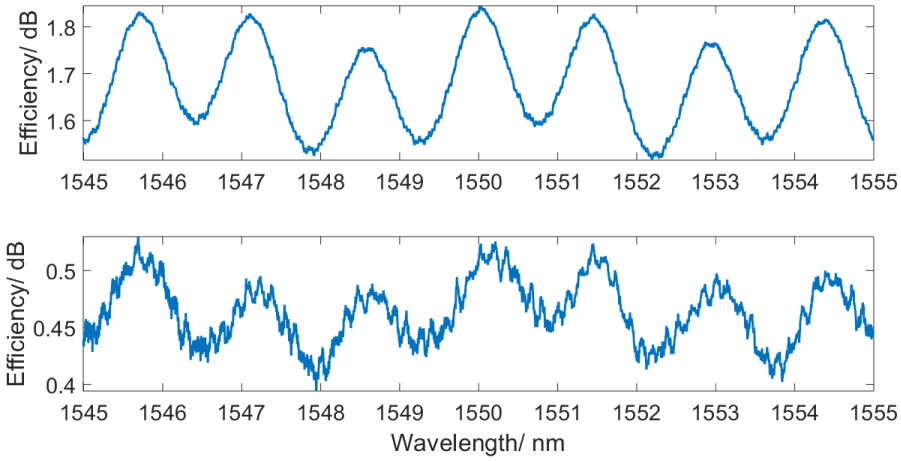

Figure 5.9: Plots analysing the finesse of a rib. They measure the ratio of output to input signal compared to the wavelength. The top plot is with no rib in the sample space, the bottom is with rib B7. It can be seen that between the two plots that the number of large oscillations does not decrease. However, there are many smaller oscillations within the large ones in the bottom plot with rib B7.

In Figure 5.9, two plots are shown. The top plot displays the results with no rib in the sample space. The bottom plot displays the results from having rib B7 in the sample space. Comparing the two plots shows they both have the same number of large oscillations. It is clear that these larger oscillations originate from some resonance in the measurement system. Using Equation (5.4) [170],

by taking the measured period 1.5 nm and assuming an index of 1 for air, a length of 0.8 mm is estimated, meaning these oscillations are most likely caused by reflections between the end of the optical fibre and the rib input facet.

$$l = \frac{\lambda_0^2}{2\ n\ \Delta\lambda\ \cos\theta} \tag{5.4}$$

$\Delta\lambda$ is the change in wavelength being measured, θ is the angle of incidence, λ_0 is the initial wavelength, and n is the waveguide index. For LN at 1550 nm, n is 2.1376 [123]. All components of the setup point directly at each other, so θ is 0, which makes cos θ equal to 1.

In Figure 5.9, there also appear to be a number of smaller oscillations within the larger ones in the plot for the rib.

The faster oscillations in rib B7 are around 0.2 nm. Using Equation (5.4), and the length of these smaller oscillations, a value of 2.81 mm for the length of the waveguide can be calculated. 2.81 mm is close to the actual rib length of 3 mm. It is worth considering also, that while the rib design was 3 mm, a small amount of that length will have been lost. This will have come from the wafer saw, where the samples were cut so that the ends of the ribs were exposed, and from the FIB, where the end of the rib was ablated to provide a good facet. Another possibility for the slight discrepancy in length is a variation in the index of the LN. Therefore, 2.81 mm is a realistic answer for the rib length.

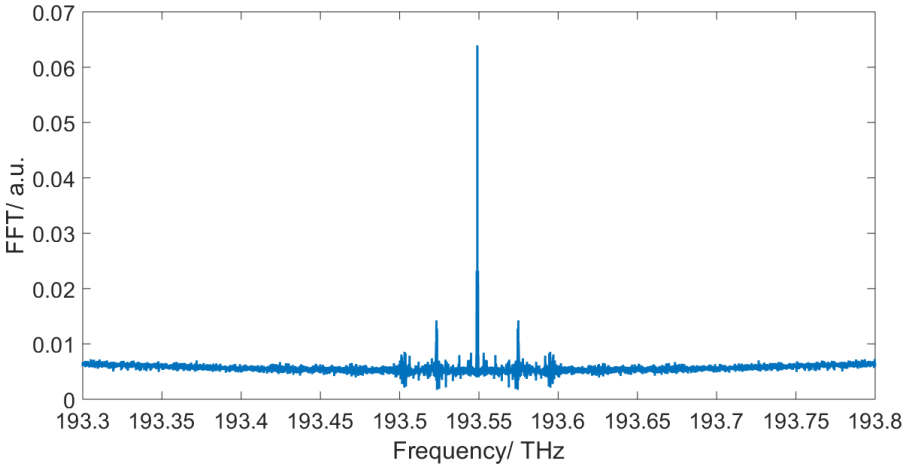

Figure 5.10: An Fast Fourier Transform (FFT) of the lower plot in Figure 5.9. The displayed frequency range has been cropped to exclude areas with high noise, likely caused by the free space oscillations seen in the original plot. A single frequency component is seen to contain most of the signal with two smaller sidebands, although other components may be hiding in the noisy data. The units a.u. stands for arbitrary units.

Figure 5.10 displays the FFT of the data shown in the lower plot of Figure 5.9. A cropped frequency range is shown, due to high levels of noise outside

of this range. The high noise levels are likely due to the large oscillations in Figure 5.9 that the rib oscillations were within. This FFT shows the majority of power within a single frequency component. There are two noticeable but small peaks either side of this larger peak. It is possible that further components are hidden within the frequencies with high noise.

It has been shown that the small oscillations in Figure 5.9 are the rib, rather than noise. The resonances are not very uniform, though can be seen generally to not be particularly sharp. The finesse is very low, as the ratio of resonance distance to width is poor. Taking one resonance at around 1550 nm, it has a width of approximately half the distance between resonances, which, using Equation (5.3), gives a finesse of around 2. Also using Equation (5.3), and taking the absorption coefficient values from Section 5.3, the facet reflectivity is calculated as around 0.40. This means that two fifths of the light which reaches a facet is put back into the rib, while three fifths of the light is lost.

The average number of round trips the light takes through the cavity can be calculated with the finesse by using Equation (5.5) [171].

$$RT_{avg} = \frac{Finesse}{2\pi} \tag{5.5}$$

The average number of round trips is calculated at around 0.32. As this is less than one half, it implies most light does not successfully reach one facet from the other. When also taking into consideration the low reflectivity value, a low efficiency is seen, where most of the light is lost during propagation and when reaching a facet.

This work has evidenced that while a signal is seen at the end of the rib, it is a small fraction of the input power. Over a third of the light successfully coupled to the highest performing 3 mm rib does not reach the end facet. As discussed before with the efficiency testing of Section 5.3, there is great scope for improvement of the fabrication of the test ribs, as this was a first trial batch. Refinement of the process should increase the quality of the ribs. It would also be worth using shorter ribs, to ensure that more of the coupled signal reached the end of the waveguide. The length could then be extended as the fabrication processing improved. A sensible next testing step would be to test the performance of different length LN ribs when using two NIR lasers with a splitter combiner as an input, as an experiment into the achievable walk-off length from the NIR waves. This could be done by testing ribs of different lengths, and recording their losses using a PD. By plotting the measured loss values, the length walk off starts can be determined by checking where on the plot the loss function changes, as the loss growth shall accelerate beyond this length.

5.5 Polarisation

The polarisation response of the ribs was assessed. This was important due to designing the waveguides to work in a vertical polarisation for compatibility

with the metal-metal THz waveguide and therefore also QCLs.

A polarisation analyser was used for these experiments; an optical element which only lets one plane of polarisation through. This means it can be used to analyse the polarisation of the incoming light. One was procured from Thor-Labs, part number LPNIRC050. It has an extinction ratio of greater than 1000:1 between 1100 and 1800 nm. The analyser was mounted in a continuous rotation mount, which allowed the analyser to be set at any angle. Rotating the polarisation analyser changed how much of the signal was blocked.

The input polarisation was adjusted using the polarisation paddles. The polarised signal was passed to the PM lensed fibre, which was also in a rotation mount, so could be rotated by 90° to change between horizontally or vertically aligned. Care was taken to not strain the fibre by over-twisting. With no rib in the sample space, and using the analyser, the paddles were adjusted to align the polarisation to the slow axis of the PM lensed fibre. The signal reaching the PD was next maximised when the analyser was set at either horizontal or vertical by rotating the fibre. This meant the polarisation through the lensed fibre was the same as the analyser. The paddles were left fixed and the input polarisation to the waveguides was changed only by rotating the PM lensed fibre.

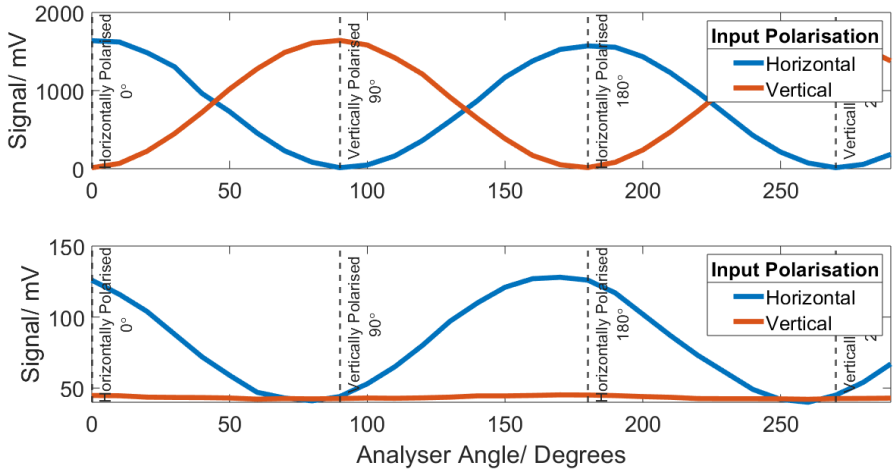

Figure 5.11: Two plots analysing the influence of polarised rays on the transmission through the test ribs. The top plot shows the transmission without a rib in the sample space, as the analyser is rotated when the polarisation plane of the PM fibre is set to horizontal or vertical. No PD gain was used. The bottom plot shows the transmission through rib C8 as the analyser is rotated when the polarisation plane of the PM fibre is set to horizontal or vertical. It is believed that some fibre slipping occurred, resulting in the slightly displaced peaks in comparison to the plot with no sample. The PD gain was set at 70 dB.

An initial sample data set was taken with no rib in the sample space. This data is presented in the top plot of Figure 5.11. An equal amount of signal gets

through between horizontal and vertical polarisation, as expected.

Ribs B7 and C8, which are 2.6 µm wide, and 3 mm and 4 mm long respectively, were used for the experiment due to being the most efficient ribs. The data presented in the lower plot of Figure 5.11 details the PD signal through rib C8 when the input polarisation is set to either horizontal or vertical, and the analyser is rotated through more than a single 180° cycle. Comparing the two plots of Figure 5.11, it can be seen with rib C8 that the maximum and minimum data points no longer align to the analyser positions of horizontal and vertical. This is likely to be due to a small slip of the fibre in its rotation mount, rather than an effect of the rib itself. Rib B7 showed the same plot shape as rib C8 in Figure 5.11.

The horizontal polarisation lets significantly more signal through than vertical polarisation when aligned with the analyser. This was expected, to an extent, due to the simulated polarisation analysis presented in Section 3.3.1.1. When also considering the ease of finding suitable mode solutions for horizontally polarised NIR modes in comparison to vertically polarised solutions, this data indicates that the LN ribs would be much more suited for horizontally polarised purposes. However, it was not indicated in Figure 3.10 that so little vertical polarisation would get through the device, which is an issue to the successful function of the device. It is not known why so few of the vertically polarised rays reach the end of the waveguide.

It should be noted that there is still a small amount of power reaching the detector at vertical polarisations, and this is likely to increase as the fabrication process is refined. This will then match the THz frequency polarisation design of the matched double metal waveguide.

From the data gathered in this section, it can be assumed that the data presented in Section 5.3 was dominated by horizontal polarisation. In theory it is possible to perform the experiments again with the signal restricted to vertical polarisation to assess the impact of the polarisation on the coupling and propagation losses, but the signals are likely too small to successfully measure in practice. Figure 5.8 in Section 5.3 demonstrated how the propagation losses of these ribs is low enough to generate THz generation. This is likely not the case if only taking vertically polarised input. Therefore, the results of this section indicate that a design change may be in order. A shift away from a double metal confinement technique is needed to move away from vertical polarisation. One option is to perform confinement using a wafer bonded structure.

Chapter 6

Terahertz Characterisation

An alternative waveguide was developed as an interim step to the device outlined in the work above. This waveguide requires less stringent matching conditions, while also being quicker and simpler to fabricate. A key aim of this device is to check the THz generation, as opposed to the NIR testing of the ribs in Chapter 5.

Building upon the information in Section 2.4.1, the premise of this new device was to take advantage of the cone shape emission of THz. The advantage of Cherenkov cones are the minimal wave copropagation, as the THz is extracted at an angle. Therefore these devices can be used to look at the THz generation performance with minimal destructive interference.

The chapter sections are outlined below:

- Cherenkov Lithium Niobate Waveguide
- Fabrication
- Experimental Arrangement
- Results

6.1 Cherenkov Lithium Niobate Waveguide

An alternative waveguide, also made out of a LN rib, was developed as an intermediate step to full phase matching. This proposed waveguide is without a bottom layer of gold, so the THz is not confined to the rib but able to escape into the substrate. This waveguide uses a silicon substrate. The waveguide then either has a radiation extracting silicon prism block mounted on it (pictured in Figure 6.1a), or the substrate is polished into a prism (pictured in Figure 6.1b), in order to gain a usable emission wavefront. The samples developed for this work used the externally mounted prism method in order to avoid mechanical polishing on small scale devices.

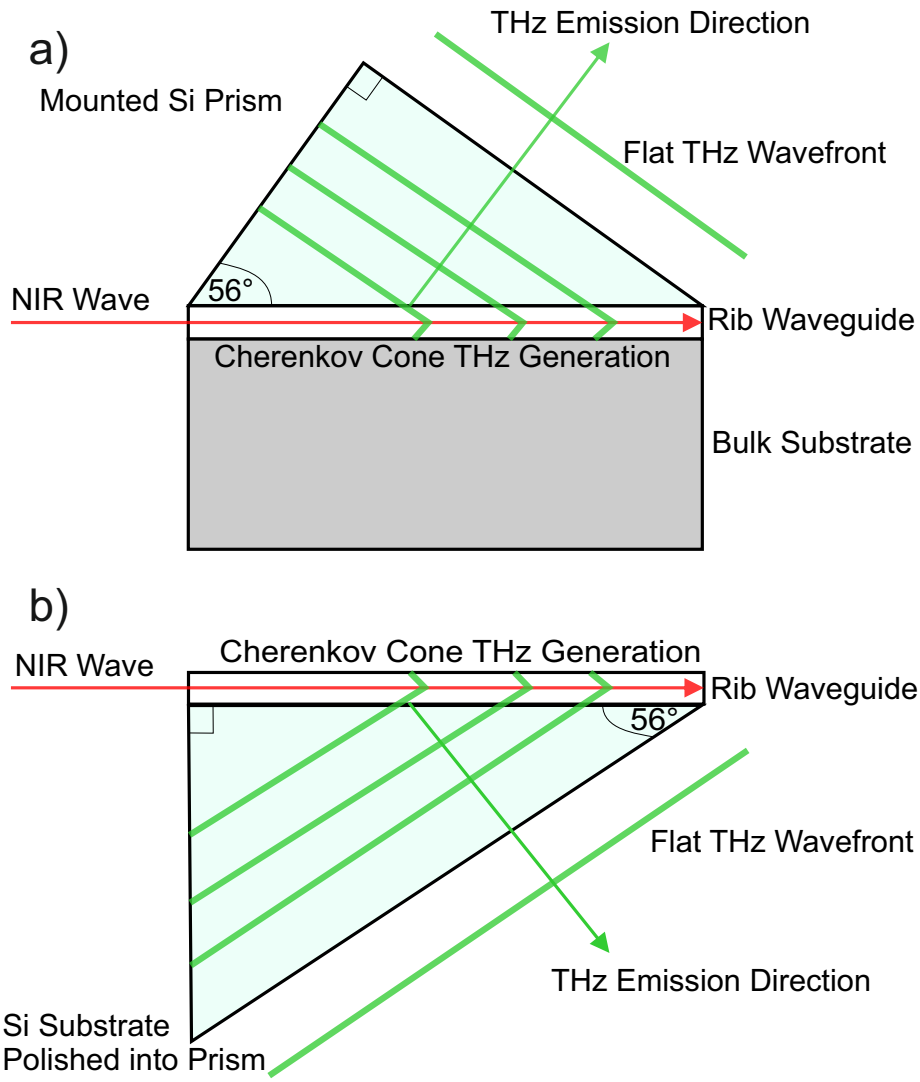

Figure 6.1: A sideview diagram of the design of the waveguide a) with a mounted prism, and b) with the substrate polished into a prism.

The premise of this waveguide is to utilise Cherenkov generated radiation, described in Section 2.4.1. The pump laser enters the thin film from the side of the sample, and as the THz is generated in a cone towards the top of the thin film, it is collected by the prism. The flat face of the prism then acts as an extraction mechanism, providing a flat face emission wavefront. The angle of the prism is calculated using Equation (2.27). By using the refractive indices

of LN and Si:

$$\arccos(\frac{n_{\mathrm{O}}}{n_{\mathrm{T}}}) \equiv \arccos(\frac{2.1376}{3.4175}) \approx 51.3^{\circ} \tag{6.1}$$

where n_{O} is the bulk material index the optical rays are travelling through (the LN), while n_{T} is the index the other side of the material boundary which the THz travels through (the silicon prism).

What makes this calculation more complex than is depicted from the simplicity of Equation (6.1) is the concept that the THz shall be generated at the material boundary interface. While this keeps the equation simple, in practice it is likely to more more complex. For example, the THz wave may pass through a small amount of LN before reaching the Si interface. This would result in a Cherenkov angle around 64°, which would then experience refraction at the Si prism surface according to Snell's law, creating an emission angle closer to 40°. This is a significant angle difference from the initial 51.3°, which can lead to system misalignment. The simplest action would be to simply generate the THz further from the material interface. However, this is not possible when trying to use a thin film sample for high confinement, as well as potentially leading to additional issues surrounding the amount of attenuation experienced by the THz waves as they propagate through the bulk LN. An additional factor to consider is whether the bulk index or mode index should be used for LN, as this could adjust the calculated value from Equation (6.1) further, to around 56°. A further factor to consider is that a 250 nm thick layer BCB is used within this device to act as a glue between the substrate and the prism.

Si prisms were obtained for this work with an angle of 56°. This uses the assumptions that the mode index is required, that the THz is generated at the boundary interface, and that the BCB does not influence the emission angle.

Using an extraction prism not only provides a flat wavefront, but additionally sees less loss due to the NIR and THz waves not propagating together for long distances through the LN. This waveguide is also simpler than the first proposed waveguide due to only having two different wavelengths to consider rather than three, as there is only a single input frequency. However, this extraction method also means that a poor beam shape is obtained out of the large emission area. The wavefront is very large and likely needs collecting and altering before being suitable for use.

6.2 Fabrication

Because of choosing to add an extraction prism to the top of the sample rather than polish the substrate, either Wafer 1 or Wafer 2 can be used for the fabrication of this waveguide. The substrate used was Wafer 1. The substrate is cut from the wafer using the fine grit blade on the surface, to gain good quality sample sides in order to reduce insertion losses. A coarser blade is then used to cut the rest of the sample through the back. After cleaning with solvents, the sample has a layer of BCB spun on to act as a glue for the prism. This BCB is diluted with mesitylene, allowing for a much thinner layer. The mixture is

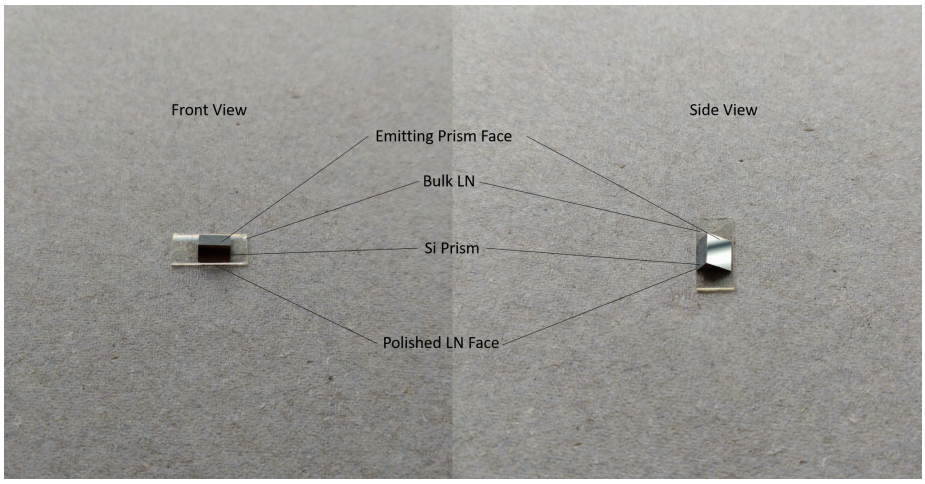

Figure 6.2: Two photos displaying a Si prism mounted on a piece of bulk LN, as used in Section 6.4.2. A thin film version of this device is used in Section 6.4. The change from thin film to bulk was to allow more light to be coupled into the device and provide more material to perform OR. The low confinements however result in low intensities through the samples, leading to poor THz generation efficiencies.

3:1 of mesitylene:BCB. A spin at 3000 rpm provides a layer thickness of around 250 nm. The Si prism is then placed on top of the BCB layer, and very gently held down using tweezers while the sample undergoes a soft bake on a hotplate following the BCB spin deposition. The soft bake is 100°C for 1 minute, using a glass slide under the sample in order to ramp the temperature to avoid damaging the LN. Once the bake is complete, the BCB has dried, fixing the prism in place. Placing the prism onto the BCB topped substrate was not found to be an issue, despite concerns that an edge bead formed during the spin process would create a gap between the prism and the substrate, caused by the prism sitting on top of the bead. This was checked by looking at the side of the sample using an optical microscope. Any BCB from the spin which spilled over the side of the substrate onto the surface which the pump laser would enter needed to be removed to reduce insertion losses. This was done by giving the sample surface a gentle wipe using a lint free cloth soaked in T1100 stripper. The samples were not cured, due to the limited number of Si prisms available, as curing the samples would permanently adhere the prism to the surface. Uncured, the prisms can be extracted and cleaned for use in further experiments. A finished sample can be seen in Figure 6.2. Rather than the thin film samples used in the initial tests, the sample in Figure 6.2 uses a piece of polished bulk LN which is discussed in Section 6.4.2. The sample seen in Figure 6.2 was mechanically polished to gain a good facet across the whole face, rather than using the wafer saw with a fine grit blade due to the quick wear that the blade would suffer

when cutting through a bulk substrate. Mechanical polishing is less suitable for the thin film sample because of the likelihood of severely damaging the sample edges, as discussed previously in Section 4.3.3.

6.3 Experimental Arrangement

A testing system was established to characterise the thin film samples, a diagram of which is given in Figure 6.3.

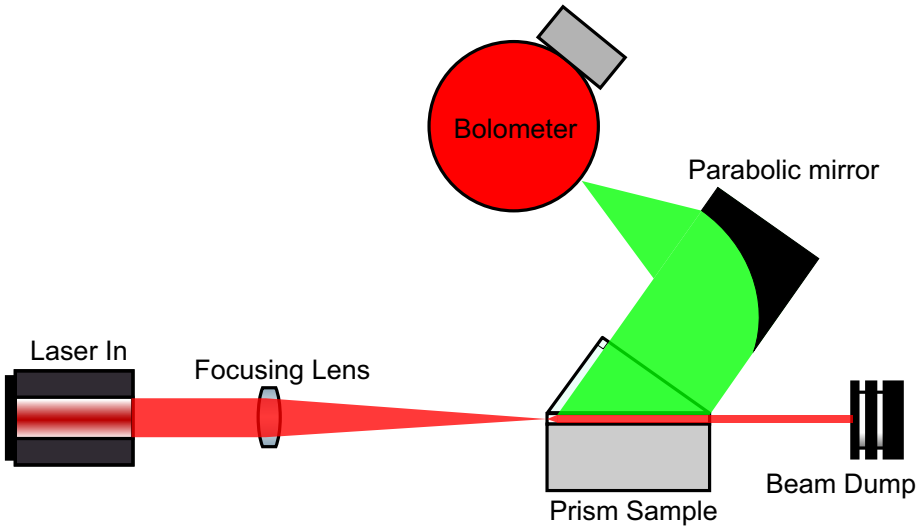

Figure 6.3: A diagram of the experimental setup. The laser beam is focused at the thin film, and collected in a beam dump as the generated THz is collected by a parabolic mirror and directed into a bolometer for detection.

A MaiTai laser from Spectra-Physics was used to provide a pump beam, operating at up to 4 W at 780 nm and pulsed at 100 fs pulse duration, 80 MHz pulse repetition rate, providing short pulses at high powers. The laser is horizontally polarised. It is important that the polarisation orientation is correct in the experiment in order to generate the THz within the crystal. The LN samples used had a Z-cut crystal orientation, meaning that the optically active crystal axis is perpendicular to the surface. The samples were mounted on their side so that the optic axis aligned with the horizontally polarised source beam.

The pump laser was focused by a lens into a spot size of 30 µm in order to have the pump power concentrated into a single spot for conversion from NIR. This provides a stronger THz generation focus, as research suggests that smaller spot sizes create greater efficiencies for Cherenkov cone based generation [100]. This spot size is still much larger than the 0.6 µm slab thin film to be focused into however, and much of the beam is lost due to the small thickness of the thin film surface.

The maximum pump power available was defined by the damage threshold of the LN, given as 4 GWcm^{-2} [172], as well as the pulse duration, frequency, and spot radius of the pump laser, as stated in Equation (6.2) below [173].

$$P_{\mathrm{In}} = D_{\mathrm{T}}(\pi r^2)(t_{\mathrm{pulse}} f_{\mathrm{pulse}}) \tag{6.2}$$

Where P_{In} is the maximum input power, D_{T} is the damage threshold, r is the spot size radius, t_{pulse} is the pulse duration from the pump laser, and f_{pulse} is the frequency of pulses from the pump laser. Using the previously stated values gives a maximum input power of 9.05 W. Therefore, all 4 W of laser power was available.

The large wavefront from the prism is focused using a parabolic mirror into a bolometer within a liquid helium bath cryostat. The model is TK1840 from QMC Instruments. A bolometer was used as the detection mechanism due to the high THz sensitivity it provides, as well as its utilisation of a Winston cone in order to gather misaligned THz emission. The pump beam is chopped at 200 Hz, and a lock-in amplifier is used in order to distinguish any signal from background radiation.

6.4 Results

6.4.1 Initial Tests

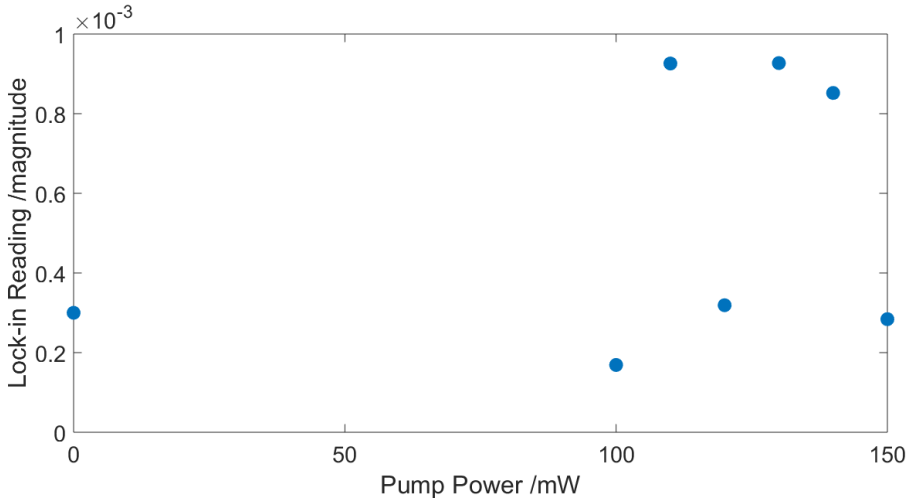

Figure 6.4: A plot conveying the average power seen at the bolometer when varying the pump power of one of the samples. The pump beam was chopped at 1000 Hz, and the lock in setting were a time constant of 1 second and a sensitivity of 10 µV. The results indicate intermittent interference within the system. Higher pump powers followed the same trend.

Two samples were initially trialled, prepared as detailed above, using Wafer 1. Neither produced any detectable signal. Figure 6.4 shows the results of one of the samples from varying the pump power. The bolometer reading changed, but seemingly not with the pump power, as it would sometimes collapse back to the noise floor when the pump power was changed again. When the detected power was above the noise floor, it was at a similar level each time, implying the cause was intermittent interference within the system. The source of the interference is unknown, however, it either appeared or disappeared upon adjustment of the pump power using a filter wheel, implying it was somehow influenced by the temporary presence of the experimenting personnel. It would be expected that a functioning sample would provide a non-linearly increasing response shape on the plot. The second sample did not differ from the noise floor.

6.4.2 Further Attempt

Following the results of the previous experiment, a new sample was fabricated, with adjustments from the previous two samples in order to improve the quality and increase the likelihood of seeing a signal. This sample used a bulk LN substrate rather than a thin film, providing a larger volume of LN to collect the pump beams and for the NIR signal to interact within, with the aim that this would provide additional signal compared to the thin film samples. The trade here is that not using thin films removes the confinement of the thin film height, reducing the intensity.

The sample can be seen in Figure 6.2. The side of the substrate was mechanically polished using diamond paper down to a 0.2 µm grit, prepared as detailed in Section 4.3.3, providing a high quality surface to improve coupling. The BCB layer was fully cured this time, as other UoL work has suggested that this increases THz transparency [151]. The cure was as stated by the BCB data sheet for a final layer, 250°C for 1 hour in a vacuum oven [164].

Due to availability of both the bolometer and the TDS system, the detection system used was changed from using the bolometer to EO detection utilising an adapted TDS system. Using EO detection addresses the issue of the bolometer being slow and struggling to differentiate between the sample and the background radiation. The EO detection system measures the the transient birefringence induced in a ZnTe EO crystal by a THz field. The change in polarisation of the probe beam is measured by a set of balanced photodiodes. The measured bias can be used to calculate the generated THz field. A disadvantage of EO detection is that it has a higher noise floor. The TDS setup is seen in Figure 6.5.

No signal was seen from this third sample either. The most likely issue is the alignment, due to the uncertainty on the direction of the THz generated. The output alignment of the emitted THz beam may have been off, and not being directed at the detector. This question about the angle needed for the prism and the system alignment is explained in Section 6.1.

Shifting to a bulk substrate was done in the hopes of using the large volume of crystal to collect more pump beam, and provide extra area to perform the

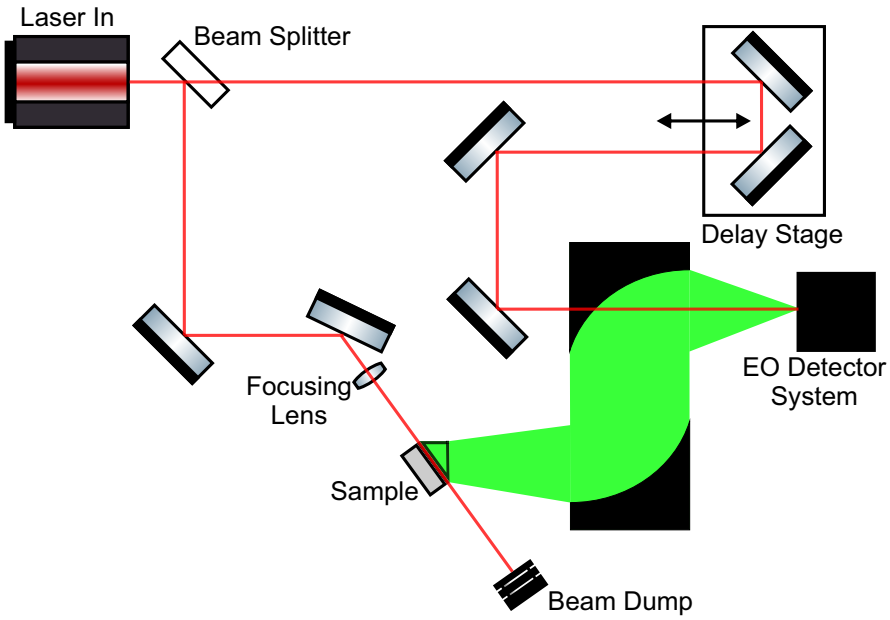

Figure 6.5: A diagram of the rearranged experimental setup, based on EO detection. The beam splitter separates the input into a pump and a probe beam. The pump beam goes to the sample, while the probe goes to the detector system via a delay stage. The EO detector system consists of a ZnTe and a pair of photodiodes to measure polarisation change of the probe line.

nonlinear process to generate a detectable signal. However, it may have introduced destructive interference due to the lack of waveguide confinement of the pump beam waist, as detailed in Section 2.4.1, as well as attenuation of any THz generated further from the prism interface. Additionally, moving away from thin film may have resulted in lower efficiency due to having a lower beam confinement [100]. The slab waveguide shape of the thin film may have suffered from the same problem due to the lack of horizontal confinement, allowing the beam to diverge along that axis from the focused spot. Simply having a lens with a smaller focus spot size may help with that if using bulk in the future.

An option for a future attempt is to use a cylindrical lens with a slab or bulk sample, which instead of focusing the pump beam to a spot, will change the beam shape to a flat line, which could be aligned to the rectangular LN substrate. If done with a higher input power to conserve intensity levels through the structure, then a large amount of THz should be generated.

Chapter 7

Conclusions and Future Work

The work shown throughout this thesis provides a good basis to progress from, with much of the initial study being produced to propel future work with. The results from the simulations and modelling together with the initial fabrication results suggests that the proposed device is feasible, albeit with some modifications and improved fabrication.

7.1 Conclusions

A device has been presented which fulfils the criteria established in Section 1.1.3 for a device needed within the THz research area. These aims are provided again below:

- Be tunable within a range of 1 to 5 THz
- Provide powers of at least a few microwatts within this frequency range
- Provide a low linewidth
- Operate at room temperature
- Provide a CW emission

The proposed device has been shown, using the simulation work in Chapter 3, to provide microwatt powers within the 1 to 5 THz range, within the conditions of room temperature and CW operation. The device also provides a low linewidth due to the dependence upon its pump beams, which can be from a highly technologically established area of telecommunications. One aim which perhaps has not been fulfilled as much as hoped is the tunability of the device. While adjusting the device is as simple as altering the frequency of the pump beams, the induced change in the effective refractive index of the device is larger

than anticipated, meaning that only a small change in operating frequency will result in a rapid drop off in emission power. It also means that two different pump beam frequencies with the same frequency difference cannot be used due to adjusting the index too much. However, this could be worked around for initial samples by fabricating several devices of a smaller operating range. It is also possible future work could experiment using periodically altering rib widths to engineer the index in an effort to create a larger tuning range by reducing the index difference.

A key positive about this device is shown in Figure 3.29. In this plot it shows that, due to energy conservation laws, higher generated THz frequencies create larger amounts of emission power. This is a large advantage compared to photomixers, which are perhaps the most comparable devices in terms of the aims set above, because the operation of photomixers does not extend into the higher frequencies specified.

The full conceived device has not been realised by the work of this project due to time constraints. However, the simulations, along with the test ribs, show promising signs that further work on the project can yield results. The simulations indicate that more than 2 µW of THz power can be generated from a waveguide of realistic length, which is significantly more than a photomixer at the same frequency. The length is limited by walk off between NIR frequencies.

The test ribs have demonstrated that LN ribs capable of guiding light can be produced in the UoL cleanroom. The ribs show that the majority of system loss comes from coupling, while the ribs themselves only make up a minority of the loss, around 4 dB/mm, despite needing improvement to reach the lower loss levels seen in other research. According to the the simulation results shown in Figure 3.26, this value is already acceptable for THz generation. However, both the propagation and coupling losses must be brought down for high generation levels.

The polarisation tests have shown that the ribs perform much more favourably when in a horizontal plane orientation. This agrees with the simulations. However, the THz frequency component of the waveguide will operate vertically polarised due to being confined using the SPP effect, so the NIR waveguide must be capable of vertical polarisation too. With refinement to the fabrication process, more signal will propagate through the NIR rib in a vertical polarisation orientation. However, if the amount of vertical polarisation reaching the end of the device does not drastically improve, a design change shall be needed. While it is not key to have the NIR frequency waves reach the end of the device, it is important to maintain a high intensity throughout in order for efficient conversion into THz. Adjusting the design to not use SPP confinement would satisfy the change to horizontal polarisation. This could possibly be implemented using a wafer bonded design.

With regards to the fabrication of the ribs, ion milling has been successfully deployed as a technique of creating low loss ribs after experimentation into patterning and masking methods and paying particular attention to sidewall quality. Different methods of creating high quality rib facets were explored, with the FIB proving a sensible choice.

The tests of the alternate waveguide design, utilising a Cherenkov cone, were unsuccessful. It is believed that this is due to misalignment. Further calculation or simulation of the correct Cherenkov angle could be done using software such as COMSOL.

7.2 Future Work

A main priority going forward is to produce some finished EO waveguides from the originally proposed design, which can be used for a THz generation test.

There are several areas of development left to complete in order to create a fully realised waveguide. They include performing further milling tests in order to create the optimum rib in terms of sidewall roughness, and experimental investigation of the deposition of the SiO_2, BCB, and gold layers. Challenges with the deposition may include quality of the deposited layers, adhesion to surrounding layers, and ensuring the processes used do not aggravate the thermal charging quality of LN.

When a functioning waveguide is established, different areas to explore exist; to enhance the waveguide design itself, and to test its applications.

A key area to explore in terms of improving the device is improving the tunability of the device, as specified in the original aims for the project. This could be done by reducing the index difference of the waveguides as the pump frequencies change. As mentioned in section 7.1, looking at the rib may provide the answer. It is possible that the index may be engineered by adjusting the rib shape, or introducing periodic width variations.

Another way to improve the device could be to experiment with incorporating gratings at the ridge facets, in an effort to reduce coupling losses. Additionally, anti-reflective coating could be applied to the facets.

The applications of a finished waveguide include THz TDS and injection locking. Of particular interest would be the injection locking of THz frequency QCLs; an underexplored area [16]. Fast TDS scans could be run at room temperature at frequencies above what is reachable by a photomixer.

As established in Section 5.5, it may be that the waveguide should undergo a design alteration due to its poor handling of vertical polarisation. If changing to a horizontally polarised design, a dielectric slab waveguide, more suited to horizontal polarisation than a plasmon waveguide, would be interesting to explore. This would require confining the THz in a way other than using an SPP waveguide, such as with a wafer bonded design.

Chapter 8

Appendix

8.1 Material Index Database

Table 8.1 and Table 8.2 provide the complex refractive index values used in the simulations shown in Chapter 3.

Refractive Indices - Real Part				
Frequency /THz	Material			
	LN	SiO_2	BCB	Gold
0.5	4.89 [47]	2.09 [121]	1.15	650 (E) [174]
1.0	4.91 [47]	2.091 [121]	1.10	447 [174]
1.5	4.95 [47]	2.094 [121]	1.36	356 [174]
1.75	4.98 [47]	2.095 [121]	1.37	322.32 [174]
1.9	5.01 [47]	2.096 [121]	1.45	306.45 [174]
1.95	5.01 [47]	2.097 [121]	1.46	301.65 [174]
1.99	5.01 [47]	2.097 [121]	1.44	297.49 [174]
2.0	5.01 [47]	2.098 [121]	1.42	296.49 [174]
2.01	5.32 [46]	2.098 [121]	1.42	295.48 [174]
2.02	5.32 [46]	2.098 [121]	1.42	294.49 [174]
2.03	5.32 [46]	2.099 [121]	1.42	293.50 [174]
2.04	5.40 [46]	2.099 [121]	1.43	292.53 [174]
2.05	5.24 [46]	2.1 [121]	1.44	291.56 [174]
2.07	5.41 [46]	2.1 [121]	1.44	294.49 [174]
2.1	5.43 [46]	2.1 [121]	1.44	286.88 [174]
2.15	5.39 [46]	2.1 [121]	1.45	282.42 [174]
2.25	5.523 [46]	2.1 [121]	1.42	274.08 [174]
2.5	5.385 [46]	2.102 [121]	1.58	255.4 [174]
3.0	5.570 [46]	2.109 [121]	1.57 [165]	225 [174]
3.5	5.711 [46]	2.118 [121]	1.57 (E) [165] [120]	199.1 [174]
4.0	5.935 [46]	2.108 [121]	1.57 (E) [165] [120]	177.47 [174]

4.5	6.259 [46]	2.14 [121]	1.57 (E) [165] [120]	160.63 [174]
5.0	6.514 [46]	2.15 [121]	1.57 (E) [165] [120]	143.95 [174]
193.0	2.1376 [123]	1.4657 [175]	1.55	0.52603 [174]
193.5	2.1376 [123]	1.4657 [175]	1.55 (E) [166]	0.52364 [174]
194.0	2.1377 [123]	1.4657 [175]	1.55 (E) [166]	0.52106 [174]
194.5	2.1378 [123]	1.4657 [175]	1.55 (E) [166]	0.51887 [174]
195.0	2.1379 [123]	1.4657 [175]	1.54 [166]	0.51627 [174]
195.5	2.1380 [123]	1.4657 [175]	1.54 (E) [166]	0.51415 [174]
196.0	2.1381 [123]	1.4657 [175]	1.54 (E) [166]	0.51207 [174]
196.5	2.1383 [123]	1.4657 [175]	1.54 (E) [166]	0.50947 [174]
197.0	2.1384 [123]	1.4657 [175]	1.54 (E) [166]	0.50728 [174]
197.5	2.1385 [123]	1.4657 [175]	1.54 (E) [166]	0.50485 [174]
198.0	2.1386 [123]	1.4657 [175]	1.54 (E) [166]	0.50249 [174]
198.5	2.1387 [123]	1.4657 [175]	1.54 (E) [166]	0.50027 [174]
199.0	2.1388 [123]	1.4657 [175]	1.54 (E) [166]	0.49770 [174]
199.5	2.1389 [123]	1.4657 [175]	1.54 (E) [166]	0.49573 [174]
200.0	2.1391 [123]	1.4658 [175]	1.54 (E) [166]	0.49350 [174]
200.5	2.1392 [123]	1.4658 [175]	1.54 (E) [166]	0.49124 [174]
201.0	2.1393 [123]	1.4658 [175]	1.54 (E) [166]	0.48931 [174]

Table 8.1: A table listing the real components of the refractive indices of materials used in the simulations in Chapter 3. Values with (E) after them are estimates based on available data. Unreferenced BCB values taken from experimental data, discussed in Section 4.4.2.

Refractive Indices - Imaginary Part				
Frequency /THz	Material			
	LN	SiO_2	BCB	Gold
0.5	0.00477i [47]	0.0035i [121]	0.015i [120]	650i (E) [174]
1.0	0.0119i [47]	0.0015i [121]	0.02i (E) [120]	534i [174]
1.5	0.0191i [47]	0.001i [121]	0.02i (E) [120]	444i [174]
1.75	0.0246i [47]	0.001i [121]	0.0225i (E) [120]	410.32i [174]
1.9	0.0298i [47]	0.001i [121]	0.0225i (E) [120]	394.45i [174]
1.95	0.0298i [47]	0.001i [121]	0.025i (E) [120]	389.67i [174]
1.99	0.0298i [47]	0.001i [121]	0.025i (E) [120]	385.73i [174]
2.0	0.0298i [47]	0.001i [121]	0.025i (E) [120]	384.77i [174]
2.01	0.0298i [47]	0.001i [121]	0.025i (E) [120]	383.81i [174]
2.02	0.0298i [47]	0.001i [121]	0.025i (E) [120]	382.87i [174]
2.03	0.0299i [47]	0.001i [121]	0.025i (E) [120]	381.94i [174]
2.04	0.0299i [47]	0.001i [121]	0.025i (E) [120]	381.01i [174]
2.05	0.03i [1]	0.0015i [121]	0.0275i (E) [120]	380.10i [174]
2.07	0.028i [1]	0.0015i [121]	0.0275i (E) [120]	382.87i [174]
2.1	0.0275i [1]	0.0015i [121]	0.0275i (E) [120]	363.51i [174]
2.15	0.025i [1]	0.001i [121]	0.0275i (E) [120]	371.42i [174]

2.25	0.025i [1]	0.0015i [121]	0.0275i (E) [120]	375.66i [174]
2.5	0.0191i [1]	0.0015i [121]	0.03i (E) [120]	346.2i [174]
3.0	0.159i [1]	0.002i [121]	0.03i (E) [120]	319i [174]
3.5	0.341i [1]	0.003i [121]	0.03i (E) [120]	297.3i [174]
4.0	0.477i [1]	0.0055i [121]	0.035i (E) [120]	278.6i [174]
4.5	0.424i [1]	0.002i [121]	0.04i (E) [120]	263.5i [174]
5.0	0.382i [1]	0.003i [121]	0.04i (E) [120]	249.04i [174]
193.0	Negligible [130]	0 [175]	Negligible	10.768i [174]
193.5	Negligible [130]	0 [175]	Negligible	10.737i [174]
194.0	Negligible [130]	0 [175]	Negligible (E)	10.703i [174]
194.5	Negligible [130]	0 [175]	Negligible	10.675i [174]
195.0	Negligible [130]	0 [175]	Negligible (E)	10.641i [174]
195.5	Negligible [130]	0 [175]	Negligible	10.614i [174]
196.0	Negligible [130]	0 [175]	Negligible (E)	10.587i [174]
196.5	Negligible [130]	0 [175]	Negligible	10.553i [174]
197.0	Negligible [130]	0 [175]	Negligible (E)	10.524i [174]
197.5	Negligible [130]	0 [175]	Negligible	10.493i [174]
198.0	Negligible [130]	0 [175]	Negligible (E)	10.462i [174]
198.5	Negligible [130]	0 [175]	Negligible	10.433i [174]
199.0	Negligible [130]	0 [175]	Negligible (E)	10.400i [174]
199.5	Negligible [130]	0 [175]	Negligible	10.374i [174]
200.0	Negligible [130]	0 [175]	Negligible (E)	10.345i [174]
200.5	Negligible [130]	0 [175]	Negligible	10.316i [174]
201.0	Negligible [130]	0 [175]	Negligible (E)	10.290i [174]

Table 8.2: A table listing the imaginary components of the refractive indices of materials used in the simulations in Chapter 3. Values with (E) after them are estimates based on available data. BCB NIR data taken experimentally.

Simulations using doped BCB used the values from Table 3.2 at all THz frequencies. Future work should include index testing of doped BCB across the THz frequency range for more reliable simulation data.

8.2 Simulation Values

Table 8.3 provides the values used to create the plot lines for different frequencies in Figure 3.29.

Simulation Variables			
THz Frequency /THz	NIR Frequency /THz	Refractive Index	THz Absorption Coefficient /cm^{-1}
1	193.5	1.8093	18.64
2	194	1.8835	36.35
3	194.5	1.9644	58.23
4	195	2.0285	83.35
5	195.5	2.0969	103.75

Table 8.3: A table providing the values of the variables used for the simulation with results displayed in Figure 3.29. Index and absorption coefficient values taken from COMSOL simulations.

Chapter 9

Bibliography

[1] Yun Shik Lee. *Principles of Terahertz Science and Technology*. Springer, Boston, MA, 2009.

[2] Carlo Sirtori. Applied Physics: Bridge for the Terahertz Gap. *Nature*, 417(6885):132–133, 2002.

[3] Benjamin S Williams. *Terahertz Quantum Cascade Lasers*. PhD thesis, Massachusetts Institute of Technology, 2003.

[4] John F. Federici, Brian Schulkin, Feng Huang, Dale Gary, Robert Barat, Filipe Oliveira, and David Zimdars. THz Imaging and Sensing for Security Applications—Explosives, Weapons and Drugs. *Semiconductor Science and Technology*, 20(7):S266–S280, 2005.

[5] Ashish Y. Pawar, Deepak D. Sonawane, Kiran B. Erande, and Deelip V. Derle. Terahertz Technology and its Applications. *Drug Invention Today*, 5(2):157–163, 2013.

[6] Peter De Maagt and Janet Charlton. Terahertz Space Applications and Technology. In *IEEE MTT-S International Microwave Symposium Digest*, pages 621–624, 2005.

[7] Joshua R. Freeman, Lalitha Ponnampalam, Haymen Shams, Reshma A. Mohandas, Cyril C. Renaud, Paul Dean, Lianhe Li, A. Giles Davies, Alwyn J. Seeds, and Edmund H. Linfield. Injection Locking of a Terahertz Quantum Cascade Laser to a Telecommunications Wavelength Frequency Comb. *Optica*, 4(9):1059, 2017.

[8] Milda Tamosiunaite, Stasys Tamosiunas, Mindaugas Zilinskas, and Gintaras Valusis. Atmospheric Attenuation of the Terahertz Wireless Networks. In *Broadband Communications Networks - Recent Advances and Lessons from Practice*. IntechOpen, 2018.

[9] Rüdeger Köhler, Alessandro Tredicucci, Fablo Beltram, Harvey E. Beere, Edmund H. Linfield, A. Giles Davies, David A. Ritchie, Rita C. Iotti, and Fausto Rossi. Terahertz Semiconductor-Heterostructure Laser. *Nature*, 417(6885):156, 2002.

[10] Mikhail A. Belkin, Federico Capasso, Alexey Belyanin, Deborah L. Sivco, Alfred Y. Cho, Douglas C. Oakley, Christopher J. Vineis, and George W. Turner. Terahertz Quantum-Cascade-Laser Source Based on Intracavity Difference-frequency Generation. *Nature Photonics*, 1(5):288–292, 2007.

[11] H. W. Hübers, R. Eichholz, S. G. Pavlov, and H. Richter. High Resolution Terahertz Spectroscopy with Quantum Cascade Lasers. *Journal of Infrared, Millimeter, and Terahertz Waves*, 125(15):151401, 2019.

[12] Lars Liebermeister, Simon Nellen, Robert Kohlhaas, Steffen Breuer, Martin Schell, and Björn Globisch. Ultra-Fast, High-Bandwidth Coherent CW THz Spectrometer for Non-Destructive Testing. *Journal of Infrared, Millimeter, and Terahertz Waves*, 40(3):288–296, 2019.

[13] C. P. Endres, F. Lewen, T. F. Giesen, S. Schlemmer, D. G. Paveliev, Y. I. Koschurinov, V. M. Ustinov, and A. E. Zhucov. Application of Superlattice Multipliers for High-Resolution Terahertz Spectroscopy. *Review of Scientific Instruments*, 78(4):043106, 2007.

[14] Takeshi Yasui, Yasuhiro Kabetani, Eisuke Saneyoshi, Shuko Yokoyama, and Tsutomu Araki. Terahertz Frequency Comb by Multifrequency-Heterodyning Photoconductive Detection for High-Accuracy, High-Resolution Terahertz Spectroscopy. *Applied Physics Letters*, 88(24):241104, 2006.

[15] N. Laman, S. Sree Harsha, D. Grischkowsky, and Joseph S. Melinger. High-Resolution Waveguide THz Spectroscopy of Biological Molecules. *Biophysical Journal*, 94(3):1010–1020, 2008.

[16] Reshma Anamari Mohandas. *Development of Terahertz Photomixer Technology at Telecommunications Wavelength.* PhD thesis, University of Leeds, 2016.

[17] L. H. Li, L. Chen, J. R. Freeman, M. Salih, P. Dean, A. G. Davies, and E. H. Linfield. Multi-Watt high-power THz frequency quantum cascade lasers. *Electronics Letters*, 53(12):799–800, 2017.

[18] B. S. Williams, S. Kumar, Q. Hu, and J. L. Reno. High-Power Terahertz Quantum-Cascade Lasers. *Electronics Letters*, 42(2):89–91, 2006.

[19] S. S. Dhillon, M. S. Vitiello, E. H. Linfield, A. G. Davies, Matthias C. Hoffmann, John Booske, Claudio Paoloni, M. Gensch, P. Weightman, G. P. Williams, E. Castro-Camus, D. R.S. Cumming, F. Simoens, I. Escorcia-Carranza, J. Grant, Stepan Lucyszyn, Makoto Kuwata-Gonokami, Kuniaki Konishi, Martin Koch, Charles A. Schmuttenmaer,

Tyler L. Cocker, Rupert Huber, A. G. Markelz, Z. D. Taylor, Vincent P. Wallace, J. Axel Zeitler, Juraj Sibik, Timothy M. Korter, B. Ellison, S. Rea, P. Goldsmith, Ken B. Cooper, Roger Appleby, D. Pardo, P. G. Huggard, V. Krozer, Haymen Shams, Martyn Fice, Cyril Renaud, Alwyn Seeds, Andreas Stöhr, Mira Naftaly, Nick Ridler, Roland Clarke, John E. Cunningham, and Michael B. Johnston. The 2017 Terahertz Science and Technology Roadmap. *Journal of Physics D: Applied Physics*, 50(4):3001, 2017.

[20] A. G. Stepanov, A. A. Mel'nikov, V. O. Kompanets, and S. V. Chekalin. Spectral Modification of Femtosecond Laser Pulses in the Process of Highly Efficient Generation of Terahertz Radiation via Optical Rectification. *JETP Letters*, 85(5):227–230, 2007.

[21] V. G. Bespalov, A. A. Gorodetskiĭ, I. Yu. Denisyuk, S. A. Kozlov, V. N. Krylov, G. V. Lukomskiĭ, N. V. Petrov, and S. É. Putilin. Methods of Generating Superbroadband Terahertz Pulses with Femtosecond Lasers. *Journal of Optical Technology*, 75(10):636–642, 2008.

[22] Joshua R. Freeman, Harvey E. Beere, and David A. Ritchie. Generation and Detection of Terahertz Radiation. In Kai-Erik Peiponen, J. Axel Zeitler, and Makoto Kuwata-Gonokami, editors, *Terahertz Spectroscopy and Imaging*, chapter 1, pages 1–28. Springer, 2012.

[23] T. H. Maiman. Stimulated Optical Radiation in Ruby. *Nature*, 187(4736):493–494, 1960.

[24] Jerome Faist, Federico Capasso, Deborah L. Sivco, Carlo Sirtori, Albert L. Hutchinson, and Alfred Y. Cho. Quantum Cascade Laser. *Science*, 264(5158):553–556, 1994.

[25] Mohammed Salih. *Development of Terahertz Frequency Quantum Cascade Lasers*. PhD thesis, University of Leeds, 2011.

[26] Sushil Kumar, Benjamin S. Williams, Stephen Kohen, Qing Hu, and John L. Reno. Continuous-Wave Operation of Terahertz Quantum-Cascade Lasers Above Liquid-Nitrogen Temperature. *Applied Physics Letters*, 84(14):2494–2496, 2004.

[27] Kazuue Fujita, Seungyong Jung, Yifan Jiang, Jae Hyun Kim, Atsushi Nakanishi, Akio Ito, Masahiro Hitaka, Tadataka Edamura, and Mikhail A. Belkin. Recent Progress in Terahertz Difference-Frequency Quantum Cascade Laser Sources. *Nanophotonics*, 7(11):1795–1817, 2018.

[28] Bérengère Argence, Bruno Chanteau, Olivier Lopez, Daniele Nicolodi, Michel Abgrall, Christian Chardonnet, Christophe Daussy, Benoît Darquié, Yann Le Coq, and Anne Amy-Klein. Quantum Cascade Laser Frequency Stabilization at the Sub-Hz Level. *Nature Photonics*, 9(7):456–460, 2015.

[29] A. Khudchenko, D. G. Pavelev, V. L. Vaks, and A. M. Baryshev. Overview of Techniques for THz QCL Phase-Locking. *European Physical Journal Web of Conferences*, 195:04003, 2018.

[30] D. A. Ackerman, J. E. Johnson, L. J. P. Ketelsen, L. E. Eng, P. A. Kiely, and T. G. B. Mason. Telecommunication Lasers. In Ivan Kaminow and Tingye Li, editors, *Optical Fiber Telecommunications*, chapter 12, pages 587–665. Academic Press, 4th edition, 2002.

[31] D. H. Auston, K. P. Cheung, and P. R. Smith. Picosecond Photoconducting Hertzian Dipoles. *Applied Physics Letters*, 45(3):284–286, 1984.

[32] Reshma A. Mohandas, Joshua R. Freeman, Mark C. Rosamond, Lalitha Ponnampalam, Alwyn J. Seeds, P. J. Canard, M. J. Robertson, D. G. Moodie, A. Giles Davies, Edmund H. Linfield, and Paul Dean. Terahertz Emission Mechanism and Laser Excitation Position Dependence of Nano-Grating Electrode Photomixers. In *41st International Conference on Infrared, Millimeter, and Terahertz Waves, IRMMW-THz*, pages 1–2. IEEE Computer Society, 2016.

[33] Hiroshi Ito, Fumito Nakajima, Tomofumi Furuta, and Tadao Ishibashi. Continuous THz-Wave Generation using Antenna-Integrated Uni-Travelling-Carrier Photodiodes. *Semiconductor Science and Technology*, 20(7):S191, 2005.

[34] Andrei G Stepanov, János Hebling, and Jürgen Kuhl. Efficient Generation of Subpicosecond Terahertz Radiation by Phase-Matched Optical Rectification using Ultrashort Laser Pulses with Tilted Pulse Fronts. *Applied Physics Letters*, 83(15):3000–3002, 2003.

[35] M. Ravaro, C. Manquest, C. Sirtori, S. Barbieri, G. Santarelli, K. Blary, J.-F. Lampin, S. P. Khanna, and E. H. Linfield. Phase-locking of a 25 THz Quantum Cascade Laser to a Frequency Comb using a GaAs Photomixer. *Optics Letters*, 36(20):3969, 2011.

[36] Masayoshi Tonouchi. Cutting-Edge Terahertz Technology. *Nature Photonics*, 1(2):97–105, 2007.

[37] Tadao Ishibashi and Hiroshi Ito. Uni-Traveling-Carrier Photodiodes. *Journal of Applied Physics*, 127(3):31101, 2020.

[38] R. M. Hochstrasser and D. J. Cook. Intense Terahertz Pulses by Four-Wave Rectification in Air. *Optics Letters*, 25(16):1210–1212, 2000.

[39] Seiji Kojima, Hideaki Kitahara, Seizi Nishizawa, and Mitsuo Wada Takeda. Dielectric properties of ferroelectric lithium tantalate crystals studied by terahertz time-domain spectroscopy. *Japanese Journal of Applied Physics*, 42(9S):6238–6241, 2003.

[40] Tadao Tanabe, Ken Suto, Jun Ichi Nishizawa, Kyosuke Saito, and Tomoyuki Kimura. Frequency-tunable terahertz wave generation via excitation of phonon-polaritons in GaP. *Journal of Physics D: Applied Physics*, 36(8):953, 2003.

[41] Yujie J. Ding and Ioulia B. Zotova. Second-Order Nonlinear Optical Materials for Efficient Generation and Amplification of Temporally-Coherent and Narrow-Linewidth Terahertz Waves. *Optical and Quantum Electronics*, 32(4-5):531–552, 2000.

[42] Geoffrey New. *Introduction to Nonlinear Optics*. Cambridge University Press, Cambridge, 2011.

[43] R. S. Weis and T. K. Gaylord. Lithium niobate: Summary of Physical Properties and Crystal Structure. *Applied Physics A Solids and Surfaces*, 37(4):191–203, 1985.

[44] D. S. Smith, H. D. Riccius, and R. P. Edwin. Refractive Indices of Lithium Niobate. *Optics Communications*, 17(3):332–335, 1976.

[45] Seiji Kojima, Naoki Tsumura, Hideaki Kitahara, Mitsuo Wada Takeda, and Seizi Nishizawa. Terahertz Time Domain Spectroscopy of Phonon-Polaritons in Ferroelectric Lithium Niobate Crystals. *Jpn. J. Appl. Phys*, 41(11B):7033–7037, 2002.

[46] K. A. Kuznetsov, S. P. Kovalev, G. K. Kitaeva, T. D. Wang, Y. Y. Lin, Y. C. Huang, I. I. Naumova, and A. N. Penin. Dispersion of the Dielectric Function Real Part for Mg:LiNbO 3 Crystals at Terahertz Frequencies. *Appl Phys B*, 101:811–815, 2010.

[47] Xiaojun Wu, Chun Zhou, Wenqian Ronny Huang, Frederike Ahr, and Franz X. Kärtner. Temperature Dependent Refractive Index and Absorption Coefficient of Congruent Lithium Niobate Crystals in the Terahertz Range. *Optics Express*, 23(23):29729, 2015.

[48] Yiwen Wang, Zhihua Chen, and Hui Hu. Analysis of Waveguides on Lithium Niobate Thin Films. *Crystals*, 8(5):191, 2018.

[49] Martin M. Fejer, Dieter H. Jundt, Robert L. Byer, and G. A. Magel. Quasi-Phase-Matched Second Harmonic Generation: Tuning and Tolerances. *IEEE Journal of Quantum Electronics*, 28(11):2631–2654, 1992.

[50] Séverine Diziain, Reinhard Geiss, Matthias Zilk, Frank Schrempel, Ernst-Bernhard Kley, Andreas Tünnermann, and Thomas Pertsch. Second Harmonic Generation in Free- Standing Lithium Niobate Photonic Crystal L3 Cavity. *Appl. Phys. Lett*, 103:051117, 2013.

[51] Rui Luo, Yang He, Hanxiao Liang, Mingxiao Li, and Qiang Lin. Highly Tunable Efficient Second-Harmonic Generation in a Lithium Niobate Nanophotonic Waveguide. *Optica*, 5(8):1006–1011, 2018.

[52] Akira Otomo, George I. Stegeman, Marinus C. Flipse, Mart B. J. Diemeer, Winfried H. G. Horsthuis, and Guus R. Möhlmann. Nonlinear Contrawave Mixing Devices in Poled-Polymer Waveguides. *Journal of the Optical Society of America B*, 15(2):759, 1998.

[53] Cheng Wang, Carsten Langrock, Alireza Marandi, Marc Jankowski, Mian Zhang, Boris Desiatov, Martin M. Fejer, and Marko Lončar. Ultrahigh-Efficiency Wavelength Conversion in Nanophotonic Periodically Poled Lithium Niobate Waveguides. *Optica*, 5(11):1438, 2018.

[54] Thorlabs. Periodically Poled Lithium Niobate (PPLN) - Tutorial. Technical report, Thorlabs, 2007.

[55] Y. S. Lee, T. Meade, V. Perlin, H. Winful, T. B. Norris, and A. Galvanauskas. Generation of Narrow-Band Terahertz Radiation via Optical Rectification of Femtosecond Pulses in Periodically Poled Lithium Niobate. *Applied Physics Letters*, 76(18):2505–2507, 2000.

[56] A N Bugai, S V Sazonov, and Andrei Yu Shashkov. A Self-Consistent Regime of Generation of Terahertz Radiation by an Optical Pulse with a Tilted Intensity Front. *Quantum Electronics*, 42(11):1027–1033, 2012.

[57] A. V. Smith, D. J. Armstrong, and W. J. Alford. Increased Acceptance Bandwidths in Optical Frequency Conversion by use of Multiple Walk-Off-Compensating Nonlinear Crystals. *Journal of the Optical Society of America B*, 15(1):122, 1998.

[58] Kwan Chi Kao. *Dielectric Phenomena in Solids: With Emphasis on Physical Concepts of Electronic Processes*. Elsevier Academic Press, San Diego, California, 2004.

[59] Robert G. Hunsperger. Losses in Optical Waveguides. In *Integrated Optics*, pages 93–111. Springer, Berlin, Germany, 2002.

[60] Eugene Hecht. *Optics*. Pearson, Essex, Great Britain, 5th edition, 2017.

[61] Kai-Erik Peiponen and Evgeny Gornov. Complex Refractive Index of Media in the THz Spectral Range. In William T Rhodes, editor, *Terahertz Spectroscopy and Imaging*, chapter 3, pages 57–79. Springer, Berlin, Germany, 2012.

[62] David J Segeistein. *The Complex Refractive Index of Water*. PhD thesis, University of Missouri-Kansas City, 1981.

[63] Dietrich Marcuse. *Theory of Dielectric Optical Waveguides*. Academic Press, Inc, Amsterdam, Netherlands, 1974.

[64] V. Ramaswamy. Strip-Loaded Film Waveguide. *Bell System Technical Journal*, 53(4):697–704, 1974.

[65] Shun Lien Chuang. *Physics of Optoelectronic Devices*. Wiley, New York, New York State, 1995.

[66] J. M. Enoch. Waveguide Modes: Are They Present, and What Is Their Possible Role in the Visual Mechanism? *JOSA, Vol. 50, Issue 10, pp. 1025-1026*, 50(10):1025–1026, 1960.

[67] Mihai Ibanescu, Steven G. Johnson, Marin Soljačić, J. D. Joannopoulos, Yoel Fink, Ori Weisberg, Torkel D. Engeness, Steven A. Jacobs, and M. Skorobogatiy. Analysis of Mode Structure in Hollow Dielectric Waveguide Fibers. *Physical Review E*, 67(4):046608, 2003.

[68] E. Snitzer. Cylindrical Dielectric Waveguide Modes. *JOSA*, 51(5):491–498, 1961.

[69] C. Yeh, S. B. Dong, W. P. Brown, and K. Ha. Single-Mode Optical Waveguides. *Applied Optics*, 18(10):1490–1504, 1979.

[70] Andrea Guarino, Gorazd Poberaj, Daniele Rezzonico, Riccardo Degl'Innocenti, and Peter Günter. Electro–Optically Tunable Microring Resonators in Lithium Niobate. *Nature Photonics 2007 1:7*, 1(7):407–410, 2007.

[71] M. A. Foster, K. D. Moll, A. L. Gaeta, T. A. Birks, Y .W. Li, W. J. Wadsworth, A. Ortigosa-Blanch, J. C. Knight, T. P. M Man, P. StJ Russell, Y. Lou, M. Y. Shen, I. Maxwell, E. Mazur, D. Akimov, M. Schmitt, R. Maksimenka, K. Dukel, Y. Kondrat, A. Khokhlov, V. Shevandin, W. Kiefer, A. M. Zheltikov, P. Dumais, F. Gonthier, S. Lacroix, A. Villeneuve, P. G. J Wigley, and G. I. Stegeman. Optimal Waveguide Dimensions for Nonlinear Interactions. *Optics Express*, 12(13):2880–2887, 2004.

[72] L. G. Carpenter, S. A. Berry, and C. B.E. Gawith. Ductile Dicing of LiNbO3 Ridge Waveguide Facets to Achieve 0.29 nm Surface Roughness in Single Process Step. *Electronics Letters*, 53(25):1672–1674, 2017.

[73] Romain Blanchard, Cécile Grezes, Stefan Menzel, Christian Pflügl, Laurent Diehl, Yong Huang, Jae Hyun Ryou, Russell D. Dupuis, and Federico Capasso. Double-Waveguide Quantum Cascade Laser. *Applied Physics Letters*, 100(3):33502, 2012.

[74] Shawn Yohanes Siew, Eric Jun Hao Cheung, Haidong Liang, Andrew Bettiol, Noriaki Toyoda, Bandar Alshehri, Elhadj Dogheche, and Aaron J. Danner. Ultra-Low Loss Ridge Waveguides on Lithium Niobate via Argon Ion Milling and Gas Clustered Ion Beam Smoothening. *Optics Express*, 26(4):4421, 2018.

[75] R. V. Schmidt and I. P. Kaminow. Metal-Diffused Optical Waveguides in LiNbO3. *Applied Physics Letters*, 25(8):458–460, 1974.

[76] J. L. Jackel, C. E. Rice, and J. J. Veselka. Proton Exchange for High-Index Waveguides in LiNbO3. *Applied Physics Letters*, 41(7):607–608, 1982.

[77] M. L. Bortz and M. M. Fejer. Annealed Proton-Exchanged LiNbO3 Waveguides. *Optics Letters*, 16(23):1844–1846, 1991.

[78] David H. Smithgall and Franklin W. Dabby. Graded-Index Planar Dielectric Waveguides. *IEEE Journal of Quantum Electronics*, 9(10):1023–1028, 1973.

[79] Masaharu Fukuma, Juichi Noda, and Hiroshi Iwasaki. Optical Properties in Titanium-Diffused LiNbO3 Strip Waveguides. *Journal of Applied Physics*, 49(7):3693–3698, 1978.

[80] Payam Rabiei, Jichi Ma, Saeed Khan, Jeff Chiles, Sasan Fathpour, A W Fang, H Park, O Cohen, R Jones, M J Paniccia, J E Bowers, R S Jacobsen, K N Andersen, P I Borel, J Fage-Pedersen, L H Frandsen, O Hansen, M Kristensen, A V Lavrinenko, G Moulin, H Ou, C Peucheret, B Zsigri, and A Bjarklev. Heterogeneous Lithium Niobate Photonics on Silicon Substrates. *Optics Express*, 21(21):25573–25581, 2013.

[81] Matthieu Roussey, Leila Ahmadi, Ségolène Pélisset, Markus Häyrinen, Arijit Bera, Ville Kontturi, Janne Laukkanen, Ismo Vartiainen, Seppo Honkanen, Yuri P. Svirko, and Markku Kuittinen. Strip-loaded Slot Waveguide: A Step Beyond Integrated Photonics Limits. In *SPIE*, volume 10106, page 101061F. SPIE, 2017.

[82] Balpreet Singh Ahluwalia, Øystein Ivar Helle, Olav Gaute Hellesø, O M Maragò, P H Jones, P G Gucciardi, G Volpe, A C Ferrari, D Yin, E J Lunt, M I Rudenko, D W Deamer, A R Hawkins, and H Schmidt. Rib Waveguides for Trapping and Transport of Particles. *Optics Express*, 24(5):4477–4487, 2016.

[83] L Vivien, F Grillot, E Cassan, D Pascal, S Lardenois, A Lupu, S Laval, M Heitzmann, and J.-M Fédéli. Comparison Between Strip and Rib SOI Microwaveguides for Intra-Chip Light Distribution. *Elsevier*, 2004.

[84] Neslihan Eti and Hamza Kurt. Model Analysis of Ridge and Rib Types of Silicon Waveguides with Void Compositions. *IEEE Journal of Quantum Electronics*, 52(10), 2016.

[85] Inna Krasnokutska, Jean-Luc J. Tambasco, Xijun Li, and Alberto Peruzzo. Ultra-Low Loss Photonic Circuits in Lithium Niobate on Insulator. *Optics Express*, 26(2):897, 2018.

[86] Pieter G Kik and Mark L Brongersma. *Surface Plasmon Nanophotonics*. Springer, Dordrecht, Netherlands, 1st edition, 2007.

[87] Shun Lien Chuang. *Physics of Photonics*. Wiley, New York, New York State, 2nd edition, 2009.

[88] Keunhan Park, Ceji Fu, Bong Jae Lee, and Zhuomin M. Zhang. Study of the Surface and Bulk Polaritons with a Negative Index Metamaterial. *JOSA B*, 22(5):1016–1023, 2005.

[89] Raman Kashyap and Galina Nemova. Surface Plasmon Resonance-Based Fiber and Planar Waveguide Sensors. *Journal of Sensors*, 2009:645162, 2009.

[90] Yuan Jin, Chongzhao Wu, John L. Reno, and Sushil Kumar. Terahertz Plasmonic Lasers with Narrow Beams and Large Tunability. *SPIE*, 10123:139–150, 2017.

[91] Benjamin S Williams, Sushil Kumar, Qing Hu, and John L. Reno. Operation of Terahertz Quantum-Cascade Lasers at 164 K in Pulsed Mode and at 117 K in Continuous-Wave Mode. *Optics express*, 13(9):3331, 2005.

[92] Benjamin S. Williams. Terahertz Quantum-Cascade Lasers, 2007.

[93] Riccardo Marchetti, Cosimo Lacava, Lee Carroll, Kamil Gradkowski, and Paolo Minzioni. Coupling Strategies for Silicon Photonics Integrated Chips. *Photonics Research*, 7(2):201, 2019.

[94] Ni Yao, Ni Yao, Junxia Zhou, Junxia Zhou, Junxia Zhou, Renhong Gao, Renhong Gao, Jintian Lin, Jintian Lin, Jintian Lin, Min Wang, Min Wang, Ya Cheng, Ya Cheng, Ya Cheng, Ya Cheng, Ya Cheng, Ya Cheng, Ya Cheng, Wei Fang, Wei Fang, and Limin Tong. Efficient light coupling between an ultra-low loss lithium niobate waveguide and an adiabatically tapered single mode optical fiber. *Optics Express*, 28(8):12416–12423, 2020.

[95] E. A. Ash, C. W. Pitt, M. G. F. Wilson, E. A. Ash, C. W. Pitt, and M. G. F. Wilson. Integrated Optical Circuits for Telecommunications. *Nature*, 261(5559):377–381, 1976.

[96] Andreas Boes, Bill Corcoran, Lin Chang, John Bowers, and Arnan Mitchell. Status and Potential of Lithium Niobate on Insulator (LNOI) for Photonic Integrated Circuits. *Laser and Photonics Reviews*, 12(4):1700256, 2018.

[97] K. H. Yang, P. L. Richards, and Y. R. Shen. Generation of Far-Infrared Radiation by Picosecond Light Pulses in LiNbO3. *Applied Physics Letters*, 19(9):320–323, 1971.

[98] Janos Hebling, Gabor Almasi, Ida Kozma, and Jurgen Kuhl. Velocity Matching by Pulse Front Tilting for Large Area THz-Pulse Generation. *Optics Express*, 10(21):1161, 2002.

[99] Zheng Gong, Jialin Chen, Ruoxi Chen, Xingjian Zhu, Chan Wang, Xinyan Zhang, Hao Hu, Yi Yang, Baile Zhang, Hongsheng Chen, Ido Kaminer,

and Xiao Lin. Interfacial Cherenkov radiation from ultralow-energy electrons. *Proceedings of the National Academy of Sciences of the United States of America*, 120(38), 2023.

[100] D. H. Auston, K. P. Cheung, J. A. Valdmanis, and D. A. Kleinman. Cherenkov Radiation from Femtosecond Optical Pulses in Electro-Optic Media. *Physical Review Letters*, 53(16):1555, 1984.

[101] Koji Suizu, Kaoru Koketsu, Takayuki Shibuya, Takuya Akiba, Kodo Kawase, and Toshihiro Tsutsui. Extremely frequency-widened terahertz wave generation using Cherenkov-type radiation. *Optics Express*, 17(8):6676–6681, 2009.

[102] Zhilin Ye, Yan Chen, Rui Ni, Yong Zhang, Yaodong Wu, Shining Zhu, Yunfei Niu, and Xiaopeng Hu. Nonlinear Cherenkov radiations modulated by mode dispersion in a Ti in-diffused LiNbO3 planar waveguide. *Optics Express*, 26(2):2006–2012, 2018.

[103] Takayuki Shibuya, Toshihiro Tsutsui, Koji Suizu, Takuya Akiba, and Kodo Kawase. Efficient cherenkov-type phase-matched widely tunable terahertz-wave generation via an optimized pump beam shape. *Applied Physics Express*, 2(3):032302, 2009.

[104] Jianhao Zhang, Rongbo Wu, Min Wang, Zhiwei Fang, Jintian Lin, Junxia Zhou, Renhong Gao, Wei Chu, and Ya Cheng. High-Index-Contrast Single-Mode Optical Waveguides Fabricated on Lithium Niobate by Photolithography Assisted Chemo-Mechanical Etching (PLACE). *Japanese Journal of Applied Physics*, 59(8):086503, 2020.

[105] Luis E. Zapata, Shu-Wei Huang, Wenqian Ronny Huang, Franz X. Kärtner, Eduardo Granados, and Kyung-Han Hong. High Conversion Efficiency, High Energy Terahertz Pulses by Optical Rectification in Cryogenically Cooled Lithium Niobate. *Optics Letters*, 38(5):796–798, 2013.

[106] Yuri Avestisyan, Caihong Zhang, Iwao Kawayama, Hironaru Murakami, Toshihiro Somekawa, Haik Chosrowjan, Masayuki Fujita, and Masayoshi Tonouchi. Terahertz Generation by Optical Rectification in Lithium Niobate Crystal Using a Shadow Mask. *Optics Express*, 20(23):25752, 2012.

[107] Y. S. Lee, T. Meade, T. B. Norris, and A. Galvanauskas. Tunable Narrow-Band Terahertz Generation from Periodically Poled Lithium Niobate. In *Technical Digest - Summaries of Papers Presented at the Quantum Electronics and Laser Science Conference, QELS 2001*, pages 45–46. Institute of Electrical and Electronics Engineers Inc., 2001.

[108] Caihong Zhang, Yuri Avetisyan, Andreas Glosser, Iwao Kawayama, Hironaru Murakami, and Masayoshi Tonouchi. Bandwidth Tunable THz Wave Generation in Large-Area Periodically Poled Lithium Niobate. *Optics Express*, 20(8):8784, 2012.

[109] Y. Sasaki, H. Yokoyama, and H. Ito. Surface-Emitted Continuous-Wave Terahertz Radiation using Periodically Poled Lithium Niobate. *Electronics Letters*, 41(12):712–713, 2005.

[110] Y. Avetisyan, Y. Sasaki, and H. Ito. Analysis of THz-Wave Surface-Emitted Difference-Frequency Generation in Periodically Poled Lithium Niobate Waveguide. *Applied Physics B: Lasers and Optics*, 73:511–514, 2001.

[111] Yuzo Sasaki, Avetisyan Yuri, Kodo Kawase, and Hiromasa Ito. Terahertz-Wave Surface-Emitted Difference Frequency Generation in Slant-Stripe-Type Periodically Poled LiNbO3 Crystal. *Applied Physics Letters*, 81(18):3323–3325, 2002.

[112] Yuri Avetisyan and Masayoshi Tonouchi. Nearly Single-Cycle Terahertz Pulse Generation in Aperiodically Poled Lithium Niobate. *Photonics*, 6(1):9, 2019.

[113] Michele De Regis, Luigi Consolino, Saverio Bartalini, and Paolo De Natale. Waveguided Approach for Difference Frequency Generation of Broadly-Tunable Continuous-Wave Terahertz Radiation. *Applied Sciences*, 8(12):2374, 2018.

[114] K. Takeya, T. Minami, H. Okano, S. R. Tripathi, and K. Kawase. Enhanced Cherenkov Phase Matching Terahertz Wave Generation via a Magnesium Oxide Doped Lithium Niobate Ridged Waveguide Crystal. *APL Photonics*, 2(1):016102, 2017.

[115] Mehrdad Mehdizadeh. Fundamentals of Field Applicators and Probes at Radiofrequencies and Microwave Frequencies. In *Microwave/RF Applicators and Probes for Material Heating, Sensing, and Plasma Generation*, pages 34–67. Elsevier, Amsterdam, Netherlands, 2015.

[116] D. Molter, M. Theuer, and R. Beigang. Nanosecond Terahertz Optical Parametric Oscillator with a Novel Quasi Phase Matching Scheme in Lithium Niobate. *Optics Express*, 17(8):6623–6628, 2009.

[117] M. Theuer, G. Torosyan, C. Rau, R. Beigang, K. Maki, C. Otani, and K. Kawase. Efficient Generation of Cherenkov-Type Terahertz Radiation from a Lithium Niobate Crystal with a Silicon Prism Output Coupler. *Applied Physics Letters*, 88(7):71122, 2006.

[118] G. P. Gallerano and S Biedron. Overview of Terahertz Radiation Sources. In *Proceedings of the 2004 FEL conference*, pages 216–221, 2004.

[119] Mian Zhang, Cheng Wang, Rebecca Cheng, Amirhassan Shams-Ansari, Marko Lončar, and John A Paulson. Monolithic Ultra-High-Q Lithium Niobate Microring Resonator. *Optica*, 4(12), 2017.

[120] Elena Mavrona, Felice Appugliese, Johan Andberger, Janine Keller, Martin Franckié, Giacomo Scalari, and Jèrôme Faist. Terahertz Refractive Index Matching Solution. *Optics Express*, 2019.

[121] Christopher L. Davies, Jay B. Patel, Chelsea Q. Xia, Laura M. Herz, and Michael B. Johnston. Temperature-Dependent Refractive Index of Quartz at Terahertz Frequencies. *Journal of Infrared, Millimeter, and Terahertz Waves*, 39(12):1236, 2018.

[122] Mark A. Ordal, Robert J. Bell, Ralph W. Alexander, Larry L. Long, and Marvin R. Querry. Optical Properties of Au, Ni, and Pb at Submillimeter Wavelengths. *Applied Optics*, 26(4):744, 1987.

[123] David L. Small, David E. Zelmon, and Dieter Jundt. Infrared corrected Sellmeier coefficients for congruently grown lithium niobate and 5 mol. Percent magnesium oxide–doped lithium niobate. *JOSA B, Vol. 14, Issue 12, pp. 3319-3322*, 14(12):3319–3322, 1997.

[124] G. Ulliac, V. Calero, A. Ndao, F. I. Baida, and M. P. Bernal. Argon Plasma Inductively Coupled Plasma Reactive Ion Etching Study for Smooth Sidewall Thin Film Lithium Niobate Waveguide Application. *Optical Materials*, 53:1–5, 2016.

[125] Etienne Perret, Nicolas Zerounian, Sylvain David, and Frédéric Aniel. Complex Permittivity Characterization of Benzocyclobutene for Terahertz Applications. *Microelectronic Engineering*, 85(11):2276–2281, 2008.

[126] Lei Cao, Anne Sophie Grimault-Jacquin, Nicolas Zerounian, and Frédéric Aniel. Design and VNA-Measurement of Coplanar Waveguide (CPW) on Benzocyclobutene (BCB) at THz Frequencies. *Infrared Physics and Technology*, 63:157–164, 2014.

[127] J. M. Pitarke, V. M. Silkin, E. V. Chulkov, and P. M. Echenique. Theory of Surface Plasmons and Surface-Plasmon Polaritons. *Reports on Progress in Physics*, 70(1):1, 2006.

[128] J. H. Schmid, P. Cheben, P. J. Bock, R. Halir, J. Lapointe, S. Janz, A. Delage, A. Densmore, J.-M Fedeli, T. J. Hall, B. Lamontagne, R. Ma, I. Molina-Fernandez, and D.-X Xu. Refractive Index Engineering With Subwavelength Gratings in Silicon Microphotonic Waveguides. *IEEE Photonics Journal*, 3(3):597–607, 2012.

[129] Greg Gbur and Emil Wolf. The Rayleigh Range of Gaussian Schell-Model Beams. *Journal of Modern Optics*, 48(11):1735–1741, 2001.

[130] Judith Renate Marie-Luise Schwesyg. *Interaction of Light with Impurities in Lithium Niobate Crystals*. PhD thesis, Universitat Bonn, 2011.

[131] Robert W. Boyd. *Nonlinear Optics*. Elsevier Inc., Amsterdam, Netherlands, 2008.

[132] A. A. Michelson, Michelson, and A. A. Measurement of the Velocity of Light Between Mount Wilson and Mount San Antonio. *ApJ*, 65(1):1, 1927.

[133] Bahaa E. A. Saleh and Malvin Carl Teich. *Fundamentals of Photonics*. Wiley, Hoboken, New Jersey, 1991.

[134] Lianhe Li, Li Chen, Jingxuan Zhu, J. Freeman, P. Dean, A. Valavanis, A. G. Davies, and E. H. Linfield. Terahertz Quantum Cascade Lasers with Greater Than 1 W Output Powers. *Electronics Letters*, 50(4):309–311, 2014.

[135] Karl F Renk. *Basics of Laser Physics*. Springer, New York, New York State, 2nd edition, 2017.

[136] H. Hu, R. Ricken, W. Sohler, and R. B. Wehrspohn. Lithium Niobate Ridge Waveguides Fabricated by Wet Etching. *IEEE Photonics Technology Letters*, 19(6):417–419, 2007.

[137] P. De Nicola, S. Sugliani, G. B. Montanari, A. Menin, P. Vergani, A. Meroni, M. Astolfi, M. Borsetto, G. Consonni, R. Longone, A. Nubile, M. Chiarini, M. Bianconi, and G. G. Bentini. Fabrication of Smooth Ridge Optical Waveguides in LiNbO3 by Ion Implantation-Assisted Wet Etching. *Journal of Lightwave Technology*, 31(9):1482–1487, 2013.

[138] Nadège Courjal, Blandine Guichardaz, Gwenn Ulliac, Jean Yves Rauch, Benattou Sadani, Hui Hui Lu, and Maria Pilar Bernal. High Aspect Ratio Lithium Niobate Ridge Waveguides Fabricated by Optical Grade Dicing. *Journal of Physics D: Applied Physics*, 44(30):305101, 2011.

[139] D. W. Ward, E. R. Statz, and K. A. Nelson. Fabrication of Polaritonic Structures in LiNbO3 and LiTaO3 using Femtosecond Laser Machining. *Applied Physics A: Materials Science and Processing*, 86(1):49–54, 2007.

[140] H Hu, ; A P Milenin, ; R B Wehrspohn, ; H Hermann, ; W Sohler, A P Milenin, R B Wehrspohn, H Hermann, and W Sohler. Plasma Etching of Proton-Exchanged Lithium Niobate. *Journal of Vacuum Science and Technology A*, 24(4):1012–1015, 2006.

[141] Shawn Y. Siew, Eric J. H. Cheung, Mankei Tsang, and Aaron J. Danner. Integrated Nonlinear Optics: Lithium Niobate-on-Insulator Waveguides and Resonators. In Sonia M. García-Blanco and Gualtiero Nunzi Conti, editors, *Integrated Optics: Devices, Materials, and Technologies XXI*, volume 10106, page 101060B. SPIE, 2017.

[142] Yunpeng Jiang, Shuang Li, Hui Hu, Lutong Cai, and Yiwen Wang. Waveguides Consisting of Single-Crystal Lithium Niobate Thin Film and Oxidized Titanium Stripe. *Optics Express*, 23(19):24212–24219, 2015.

[143] K. Tanaka and T. Suhara. Fabrication of 0.7μm2 Ridge Waveguide in Ion-Sliced LiNbO3 by Proton-Exchange Accelerated Etching. In *2015 Conference on Lasers and Electro-Optics Pacific Rim*, pages 1–2. Institute of Electrical and Electronics Engineers Inc., 2015.

[144] Martin F Volk, Sergiy Suntsov, Christian E Rüter, Detlef Kip, . M Levy, R M Osgood, R Liu, L E Cross, G S Cargill, A Kumar, and H Bakhru. Low loss Ridge Waveguides in Lithium Niobate Thin Films by Optical Grade Diamond Blade Dicing. *Optics Express*, 24(2):1386–1391, 2016.

[145] scia Systems GmbH. scia Mill 150. Technical report, scia Systems GmbH, Chemnitz, Germany, 2023.

[146] Stephen J. Fonash, S. Ashok, and Ranbir Singh. Effect of Ion-Beam Sputter Damage on Schottky Barrier Formation in Silicon. *Applied Physics Letters*, 39(5):423–425, 1981.

[147] Ming Jong Tsai, Alan L. Fahrenbruch, and Richard H. Bube. Sputtered Oxide/Indium Phosphide Junctions and Indium Phosphide Surfaces. *Journal of Applied Physics*, 51(5):2696–2705, 1980.

[148] Young Soo Lee, Dong won Choi, Bonggeun Shong, Saeroonter Oh, and Jin Seong Park. Low Temperature Atomic Layer Deposition of SiO2 Thin Films using Di-Isopropylaminosilane and Ozone. *Ceramics International*, 43(2):2095–2099, 2017.

[149] Paul Poodt, David C. Cameron, Eric Dickey, Steven M. George, Vladimir Kuznetsov, Gregory N. Parsons, Fred Roozeboom, Ganesh Sundaram, and Ad Vermeer. Spatial Atomic Layer Deposition: A Route Towards Further Industrialization of Atomic Layer Deposition. *Journal of Vacuum Science and Technology A: Vacuum, Surfaces, and Films*, 30(1):010802, 2012.

[150] DOW. CYCLOTENE Advanced Electronic Resins CYCLOTENE* 4000 Series Advanced Electronic Resins (Photo BCB) Processing Procedures for CYCLOTENE 4000 Series Photo BCB Resins DS2100 Puddle Develop Process. Technical report, DOW, 2005.

[151] Chris Wood. BCB Transparency, Private Communication, 2020.

[152] J. Cunningham, C. Wood, A. G. Davies, I. Hunter, E. H. Linfield, and H. E. Beere. Terahertz Frequency Range Band-Stop Filters. *Applied Physics Letters*, 86(21):1–3, 2005.

[153] Guozhong Zhao, Maarten ter Mors, Paul C. M. Planken, and Tom Wenckebach. Terahertz Dielectric Properties of Polystyrene Foam. *JOSA B*, 19(6):1476–1479, 2002.

[154] J. Perlich, V. Körstgens, E. Metwalli, L. Schulz, R. Georgii, and P. Müller-Buschbaum. Solvent Content in Thin Spin-Coated Polystyrene Homopolymer Films. *Macromolecules*, 42(1):337–344, 2009.

[155] Manish K. Mundra, Christopher J. Ellison, Ross E. Behling, and John M. Torkelson. Confinement, Composition, and Spin-Coating Effects on the Glass Transition and Stress Relaxation of Thin Films of Polystyrene and Styrene-Containing Random Copolymers: Sensing by Intrinsic Fluorescence. *Polymer*, 47(22):7747–7759, 2006.

[156] Peter Sigmund. Elements of Sputtering Theory. *Nanofabrication by Ion-Beam Sputtering*, pages 1–40, 2012.

[157] H. Y. Zhai, L. Zhang, W. K. Chu, T. Morishita, S. Tanaka, F. Z. Xu, and Q. S. Yang. Dynamic Study and Experimental "Two-Step Process" of Substrate Step Preparation for High-Tc Josephson Junctions. *Applied Physics Letters*, 76(10):1312–1314, 2000.

[158] F. Lacour, N. Courjal, M. P. Bernal, A. Sabac, C. Bainier, and M. Spajer. Nanostructuring Lithium Niobate Substrates by Focused Ion Beam Milling. *Optical Materials*, 27(8):1421–1425, 2005.

[159] Allresist. Negative E-Beam Resists AR-N 7520. Technical report, Allresist, 2018.

[160] Arnaud Gerthoffer, Clément Guyot, Wentao Qiu, Abdoulaye Ndao, Maria Pilar Bernal, and Nadège Courjal. Strong Reduction of Propagation Losses in LiNbO3 Ridge Waveguides. *Optical Materials*, 38:37–41, 2014.

[161] T G Bifano, T A Dow, and R 0 Scattergood. Ductile-Regime Grinding: A New Technology for Machining Brittle Materials. *Engineering for Industry*, 113(2):184–189, 1991.

[162] Lingyan He, Lingyan He, Mian Zhang, Mian Zhang, Amirhassan Shams-Ansari, Rongrong Zhu, Rongrong Zhu, Cheng Wang, Cheng Wang, and Lončar Marko. Low-loss fiber-to-chip interface for lithium niobate photonic integrated circuits. *Optics Letters*, 44(9):2314–2317, 2019.

[163] K. G. Subhadra, K. Kishan Rao, and D. B. Sirdeshmukh. Systematic Hardness Studies on Lithium Niobate Crystals. *Bulletin of Materials Science*, 23(2):147–150, 2000.

[164] DOW. CYCLOTENE * 3000 Series Advanced Electronic Resins. Technical report, DOW, 2005.

[165] Urban Senica, Andres Forrer, Tudor Olariu, Paolo Micheletti, Sara Cibella, Guido Torrioli, Mattias Beck, Jérôme Faist, and Giacomo Scalari. Planarized THz Quantum Cascade Lasers for Broadband Coherent Photonics. *Light: Science and Applications*, 11:347, 2022.

[166] Md. Faruque Hossain, Hau Ping Chan, and Mohammad Afsar Uddin. Simultaneous Measurement of Thermo-Optic and Stress-Optic Coefficients of Polymer Thin Films using Prism Coupler Technique. *Applied Optics*, 49(3):403, 2010.

[167] Thomas G. Mayerhöfer, Harald Mutschke, and Jürgen Popp. Employing Theories Far beyond Their Limits—The Case of the (Boguer-) Beer–Lambert Law. *ChemPhysChem*, 17(13):1948–1955, 2016.

[168] Sareh Taebi, Mohammadreza Khorasaninejad, and Simarjeet Singh Saini. Modified Fabry-Perot Interferometric Method for Waveguide Loss Measurement. *Applied Optics*, 47(35):6625–6630, 2008.

[169] Martin Suter and Peter Dietiker. Calculation of the Finesse of an Ideal Fabry-Perot Resonator. *Applied Optics*, 53(30):7004–7010, 2014.

[170] Rongqing Hui and Maurice S O'Sullivan. *Fiber Optic Measurement Techniques*. Academic Press, Cambridge, Massachusetts, 2009.

[171] Jingwei Yang and Cheng Wang. Hybrid Thin-Film Lithium Niobate/Silicon Waveguide Scheme for Efficient Terahertz Generation. *Proceedings of the 2021 Cross Strait Radio Science and Wireless Technology Conference, CSRSWTC 2021*, pages 382–383, 2021.

[172] Covesion. Material properties of Lithium Niobate. Technical report, Covesion, 2020.

[173] Newport Corporation. Technical Note: Laser Damage Threshold. Technical report, Newport Corporation, 2024.

[174] Larry L. Long, Marvin R. Querry, Ralph W. Alexander, Mark A. Ordal, and Robert J. Bell. Optical properties of Au, Ni, and Pb at submillimeter wavelengths. *Applied Optics*, 26(4):744–752, 1987.

[175] Lihong Gao, Fabien Lemarchand, and Michel Lequime. Exploitation of multiple incidences spectrometric measurements for thin film reverse engineering. *Opt. Express*, 20(14):15734–15751, 2012.